

Anisotropic Flow Measurements in STAR at the Relativistic Heavy Ion Collider

**Anisotrope stroming gemeten met de STAR detector
aan de relativistische zware ionen versneller**

(met een samenvatting in het Nederlands)

Proefschrift

ter verkrijging van de graad van doctor aan de Universiteit Utrecht op gezag van de
rector magnificus, prof. dr. J.C. Stoof, ingevolge het besluit van het college voor
promoties in het openbaar te verdedigen op maandag 29 oktober 2007 des ochtends te
10:30 uur

DOOR

Yuting Bai

geboren op 31 december 1975 te Yulin, China

Promotor: Prof. dr. Th. Peitzmann
Co-promotor: Dr. R.J.M. Snellings

Dit werk is een onderdeel van het onderzoeksprogramma van de “Stichting voor Fundamenteel Onderzoek der Materie” (FOM), financieel gesteund door de “Nederlandse Organisatie voor Wetenschappelijk Onderzoek” (NWO).

Contents

1	Introduction	5
1.1	Quark Gluon Plasma	5
1.2	Heavy Ion Collisions	7
1.3	Probes	8
1.3.1	Hard probes	8
1.3.2	Flow	9
1.3.3	Anisotropic flow	12
1.4	Model description	14
1.4.1	Hydrodynamics	14
1.4.2	RQMD and UrQMD	16
1.4.3	AMPT	16
2	Experimental Set-up	17
2.1	RHIC	17
2.2	The STAR Detector	22
2.2.1	STAR TPC	24
2.2.2	STAR FTPCs	27
2.2.3	Trigger	28
2.2.4	Centrality definition	29
2.2.5	Particle Identification: $\frac{dE}{dx}$	31
3	Flow analysis method	35
3.1	Two particle correlation	35
3.1.1	Event plane method	35
3.1.2	Scalar product method	37
3.2	Multiparticle correlation	38
3.2.1	Cumulant method	39
3.2.2	Lee-Yang zeroes	40
4	Results	43
4.1	Datasets	43
4.2	Elliptic flow	44
4.2.1	Transverse momentum dependence	44
4.2.2	Integrated flow and its centrality dependence	48

4.2.3	Particle type dependence	49
4.2.4	Energy dependence	57
4.2.5	Rapidity dependence	69
4.3	Higher harmonics	72
4.3.1	Transverse momentum dependence	72
4.3.2	Particle type dependence	78
4.3.3	Energy dependence	79
4.3.4	Rapidity dependence	79
5	Conclusions and Summary	87
	Bibliography	89
	Samenvatting	93
	Acknowledgements	95
	Curriculum Vitae	97

Chapter 1

Introduction

The goal of heavy ion physics is to study nuclear matter under conditions of extreme temperature and density, which should ultimately lead to the formation of a new state of matter, the Quark Gluon Plasma. This state of matter is thought to have existed in the first few microseconds after the Big Bang and possibly exists in the cores of heavy neutron stars.

It is expected that such a state of matter can be created in the laboratory by colliding heavy nuclei at high energies. At the Relativistic Heavy-Ion Collider (RHIC) at Brookhaven National Laboratory (BNL) nuclei collide with energies up to $\sqrt{s_{NN}} = 200$ GeV per nucleon. The measurements described in this thesis are performed by the Solenoidal Tracker at RHIC (STAR).

The main topic of this thesis, anisotropic flow, is an observable sensitive to the early evolution and to the degrees of freedom of the created system. It is usually characterized by Fourier coefficients of the particle momentum distribution. In this thesis, the second and fourth harmonic coefficients of anisotropic flow are studied in Au+Au collisions at $\sqrt{s_{NN}} = 200$ GeV and 62.4 GeV.

The thesis is organized as follows: In chapter 2 the experimental setup is described and chapter 3 describes the methods used for measuring anisotropic flow. The measured second and the fourth order harmonic coefficients of anisotropic flow are presented and discussed in chapter 4. Finally, chapter 5 contains the conclusions and summary.

1.1 Quark Gluon Plasma

The Standard Model provides a precise description of elementary particles, quarks and leptons, and their interactions, the strong, the weak, and the electromagnetic. The interactions between these particles are mediated by vector bosons: the 8 gluons mediate strong interactions, the W^\pm and Z mediate weak interactions, and the photon mediates the electromagnetic interactions.

The strong interaction between quarks and gluons that determines the structure of hadrons and nuclei is described by the fundamental theory known as Quantum Chromodynamics (QCD). This non-Abelian gauge theory exhibits two key features: asymptotic

freedom and confinement. At short distances or large momentum transfer Q^2 , the effective coupling constant $\alpha_s(Q^2)$ decreases logarithmically, i.e quarks and gluons appear to be weakly coupled, leading to so called asymptotic freedom. At large distances or small momenta, the effective coupling becomes strong, resulting in color confinement. Thus free quarks are never found but are instead bound inside hadrons.

As a result of asymptotic freedom, the processes involving strong interactions at short distance can be described by perturbative QCD (pQCD). The non-perturbative domain can be treated by lattice QCD calculations, where the field equations are solved numerically on a discrete space-time grid.

QCD predicts that at very high temperature and/or baryon density, a phase transition from a hadronic matter to a phase of deconfined quarks and gluons will take place. This deconfined dense state of matter is called the Quark Gluon Plasma (QGP).

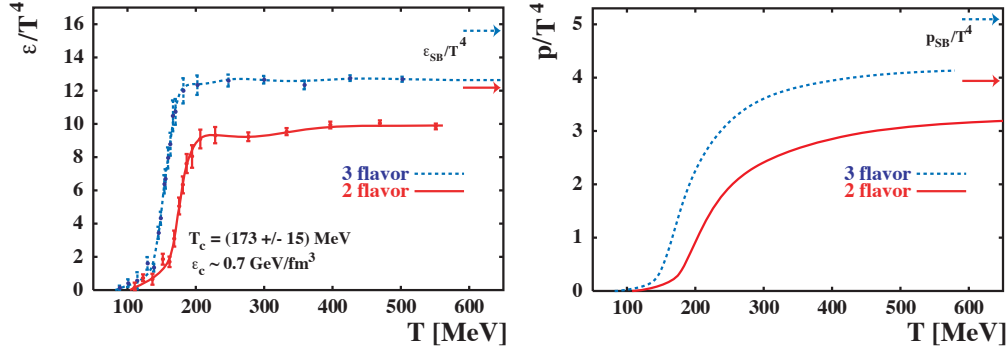


Figure 1.1: (a) Energy density ϵ as function of temperature from lattice calculations [1]. The arrows in the figure indicate the ideal Stefan-Boltzmann values. (b) The pressure versus the temperature from lattice calculations.

Lattice QCD provides quantitative information on the QCD phase transition between confined and deconfined matter and the equation of state (EoS). Properties like energy density and pressure provide direct information about the EoS and thus about the basic degrees of freedom. The estimated critical energy density and temperature are $\epsilon_c \sim 1$ GeV/fm³, $T_c \sim 170$ MeV respectively. Figure 1.1 (a) shows the calculated energy density as a function of temperature [1]. At the critical temperature $T_c \sim 170$ MeV, the energy density changes rapidly, indicating a rapid increase in the effective degrees of freedom. From these lattice calculations it follows in addition that at T_c not only deconfinement occurs but also chiral symmetry is restored. The pressure, shown in Fig. 1.1 (b), changes slowly at T_c compared to the rapid increase of the energy density. Therefore the pressure gradient in the system, $dP/d\epsilon$, is significantly reduced during the phase transition.

In the limit of an ideal Stefan-Boltzmann gas the EoS of a QGP is given by:

$$P_{SB} = \frac{1}{3}\epsilon_{SB}, \quad \epsilon_{SB} = g \frac{\pi^2}{30} T^4, \quad (1.1)$$

$$g = n_f \times 2_s \times 2_q \times 3_c \times \frac{7}{8} + 2_s \times 8_c, \quad (1.2)$$

where P_{SB} is the pressure, ϵ_{SB} the energy density and T the temperature. Each bosonic degree of freedom contributes $\frac{\pi^2}{30}T^4$ to the energy density; each fermionic degree of freedom contributes $\frac{7}{8}$ of this value. The value of g is obtained from the sum of the appropriate number of flavors \times spin \times quark/antiquark \times color factors for the quarks and spin \times color for the gluons. The energy density for a two (three) flavor QGP, where $g = 37$ ($g = 47.5$) is an order of magnitude larger than for a hadron gas where $g \sim 3$. The corresponding Stefan-Boltzmann values of the energy density and pressure are plotted in Fig. 1.1 as horizontal arrows, showing that the lattice results reach a significant fraction (0.8) of these values. The deviation from the Stefan-Boltzmann limit implies that the QCD system around T_c does not behave like a weakly interacting parton gas.

1.2 Heavy Ion Collisions

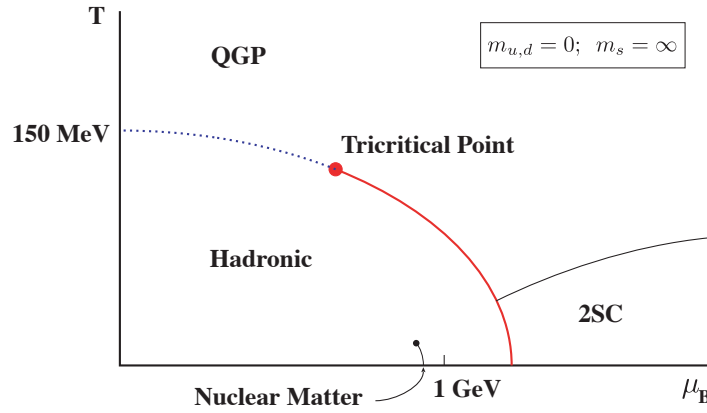


Figure 1.2: Theoretical phase diagram of nuclear matter.

The theoretical phase diagram of nuclear matter as function of temperature and baryon chemical potential is shown in Fig. 1.2. Relativistic heavy-ion collisions offer a unique tool to probe this phase diagram under controlled laboratory conditions.

The space-time evolution of a heavy-ion collision is illustrated in Fig. 1.3. The nuclei traveling at relativistic velocities appear Lorentz-contracted in the laboratory frame. After the collision, a large amount of the energy is deposited in the interaction region. If the energy density is large enough and the temperature of the created system exceeds the critical temperature T_c , a phase transition is expected to occur and a fireball of deconfined quarks and gluons is formed. Interactions among quarks and gluons may lead to thermalization and chemical equilibration. The subsequent expansion of the medium is then governed by the equation of state of the QGP. As the system expands and cools to the critical temperature T_c , hadronization takes place and the quarks and gluons become confined. Due to the finite formation time of the hadrons, the system is

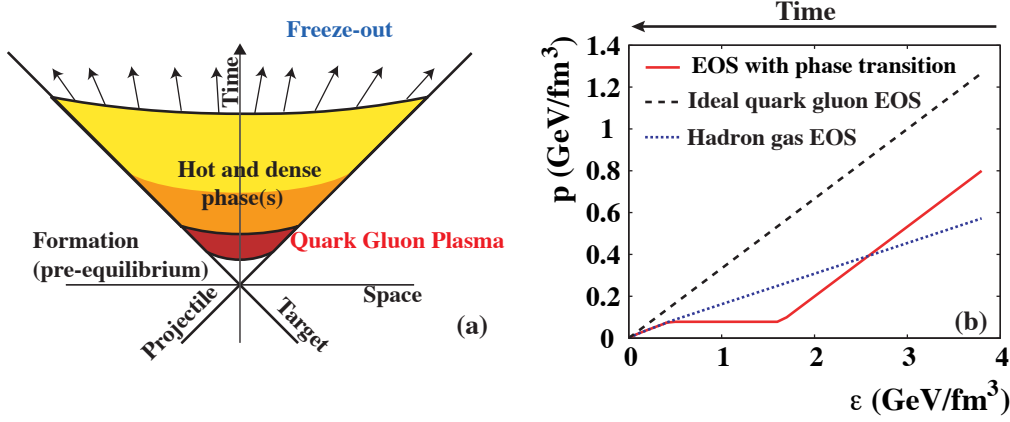


Figure 1.3: Illustration of the characteristic periods in time for a heavy-ion collision.

likely to evolve through a mixed phase where free quarks and gluons exist simultaneously with hadrons. Once all the quarks and gluons are confined inside hadrons, the system turns into a hadron gas. As the hadron gas continues to expand and the temperature cools down to the chemical freeze-out temperature T_{ch} , the inelastic scatterings between hadrons cease and the relative abundance for hadron species will not change any more. When the system becomes so dilute that the hadrons even no longer interact with each other elastically, and the system becomes free-streaming, kinetic freeze-out occurs indicated by T_{fo} .

Ultra-relativistic heavy-ion experiments have been performed at the Brookhaven Alternating Gradient Synchrotron (AGS), the CERN Super Proton Synchrotron (SPS) and the Brookhaven Relativistic Heavy Ion Collider (RHIC) with maximum center of mass energies of $\sqrt{s_{NN}} = 4.75, 17.2$ and 200 GeV respectively. The future Large Hadron Collider (LHC) at CERN will be commissioned for Pb+Pb collisions at an energy of $\sqrt{s_{NN}} = 5.5$ TeV.

1.3 Probes

In heavy ion collisions a rich set of observables is available to study the QGP and the phase transition [2]. In the following we will describe the two observables discussed in this thesis, namely parton energy loss and collective motion.

1.3.1 Hard probes

Particles with high transverse momentum are produced through the initial hard scattering processes. The hard scattering and subsequent fragmentation of partons generates jets of correlated hadrons. It is argued that energetic partons traversing a dense system lose energy by induced gluon radiation, giving rise to the so-called jet-quenching phenomenon [3]. The magnitude of this energy loss is related to the color charge density

of the medium. Therefore high p_t particles can be used as penetrating probes of the created system.

Modifications of high p_t particle production in nuclear collisions, A+B, with respect to p+p interactions are given by the nuclear modification factor defined by

$$R_{AB}(p_t) = \frac{d^2\sigma_{AB}/dp_t d\eta}{\langle N_{\text{bin}} \rangle d^2\sigma_{pp}/dp_t d\eta}. \quad (1.3)$$

Where $d^2\sigma_{pp}/dp_t d\eta$ is the inclusive cross section measured in p+p collisions and $\langle N_{\text{bin}} \rangle$ accounts for the geometrical scaling from p+p to nuclear collisions as described by the Glauber model in Sec. 2.2.4. If an Au+Au collision is an incoherent superposition of p+p collisions, the ratio would be unity. Nuclear effects such as energy loss and shadowing will reduce the ratio below unity while anti-shadowing and the Cronin effect [4] lead to a value above unity. The Cronin effect, shadowing, and gluon saturation belong to initial-state effects. The Cronin effect, an enhancement of the particle yield at intermediate p_t , is usually attributed to multiple soft parton scatterings before a hard interaction of the parton (p_t broadening). The shadowing of the structure function [5] modifies the particle yield depending on the parton momentum fraction, x_{Bj} , probed in the partonic scattering. An alternative model of the initial state of a nucleus is the gluon saturation or color glass condensate (CGC) in which the gluon population at low x_{Bj} is limited by non-linear gluon-gluon dynamics [6–8]. Initial- and final-state nuclear effects in Au+Au collisions can be isolated through studies of d+Au collisions. Figure 1.4 shows R_{AB} for charged particles in d+Au and central Au+Au collisions. A strong suppression relative to binary scaling is observed in central Au+Au collisions. In d+Au interactions no suppression but instead an enhancement is seen. Therefore the suppression in Au+Au is due to final state effects and indicates that a dense medium is created in central Au+Au collisions.

In addition to the nuclear modification factor, R_{AB} , dihadron azimuthal correlations can be used to study the effect of jet quenching. The azimuthal correlations of two high- p_t particles from jets are expected to show a narrow near-side correlation and a broader away-side correlation. However, in the case of strong jet quenching the away-side jet would be suppressed by energy loss in the traversed medium. Figure 1.5 shows the azimuthal correlations of high- p_t particles with $2 \text{ GeV}/c < p_t < p_t^{\text{trig}}$ relative to the trigger particle with $4 < p_t < 6 \text{ GeV}/c$ in p+p, d+Au and Au+Au collisions. The near-side and away-side peaks are clearly visible in p+p, minimum bias and central d+Au collisions. In central Au+Au collisions, a similar near-side peak appears while the away-side peak has disappeared. The suppression only occurs in Au+Au collisions and shows that this is a final state effect as expected from partonic energy loss mechanisms.

1.3.2 Flow

Flow refers to a collective expansion of bulk matter, arising from the density gradient from the center to the boundary of the created fireball in nuclear collisions. Interactions among constituents push matter outwards; frequent interactions lead to a common constituent velocity distribution. This so-called collective flow is therefore sensitive to the strength of the interactions. Collective flow is additive and thus accumulated over the

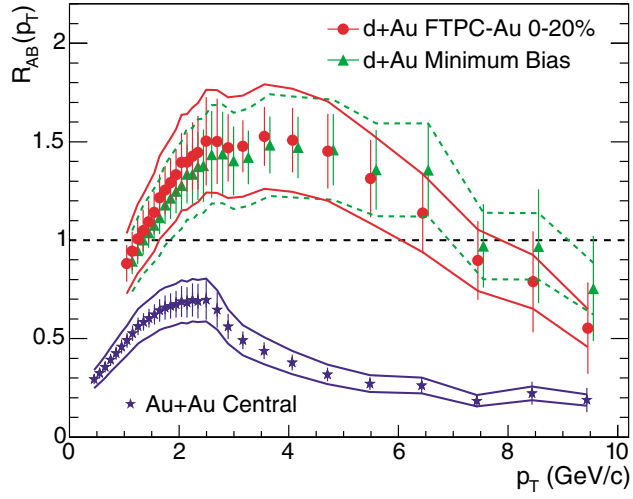


Figure 1.4: $R_{AB}(p_t)$ for d+Au and Au+Au collisions [9].

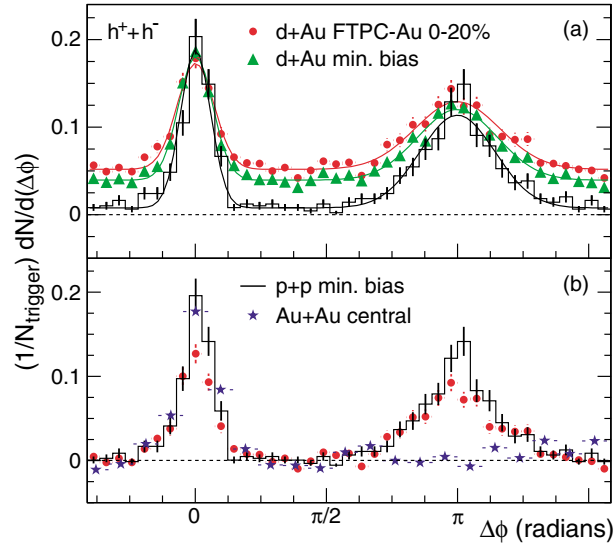


Figure 1.5: Dihadron azimuthal distributions for d+Au, Au+Au and p+p collisions [9].

whole system evolution, making it potentially sensitive to the equation of state of the expanding matter. At lower energies the collective flow reflects the properties of dense hadronic matter, while at RHIC energies a large contribution from the pre-hadronic phase is anticipated.

The particle yields as a function of transverse momentum reveal the dynamics of the collision and reflect the properties of bulk matter at kinetic freeze-out. As already mentioned above, kinetic freeze-out corresponds to the final stage of the collision when the system becomes so dilute that all interactions between the particles cease so that the momentum distributions do not change anymore. For a given particle type, the random thermal motion is superimposed onto the collective flow. The transverse momentum distribution of a specific particle type depends on the temperature at freeze-out (T_{fo}), the particle mass (m) and the transverse flow velocity ($\langle v_T \rangle$):

$$\frac{d^2N}{m_T dm_T dy} \propto \exp(-m_T/T) \quad (1.4)$$

where transverse mass is defined as $m_T = \sqrt{m^2 + p_T^2}$ and the slope of the distribution is described qualitatively by $T = T_{fo} + m\langle v_T \rangle^2$ [10]. For a more detailed and precise analysis, a hydrodynamically inspired blast wave model is used to describe the spectra [11].

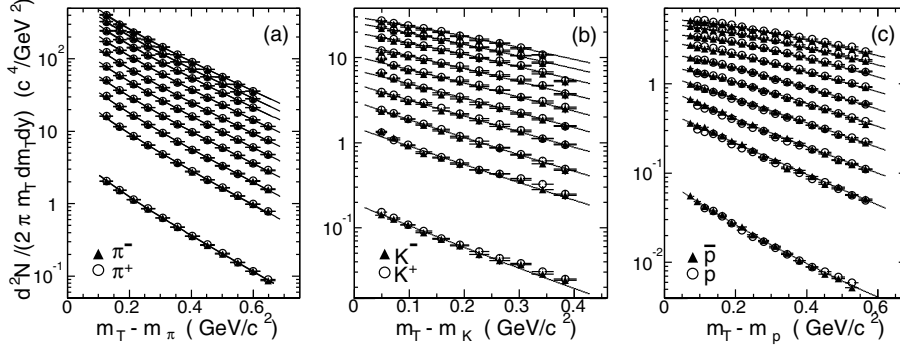


Figure 1.6: Invariant yield as function of transverse mass for π^\pm , K^\pm and p and \bar{p} for p+p (bottom set of data points in the figures) and Au+Au events from 70–80% to 0–5% centrality (from bottom to top) [12]. The curves are Bose-Einstein fits for π^- and blast-wave model fits for K^- and \bar{p} .

Figure 1.6 shows transverse mass spectra for π^\pm , K^\pm and p and \bar{p} for p+p and Au+Au collisions [12]. The lines are a fit to the particle spectra with a blast wave model. The fit describes all the particle spectra rather well, which shows that these spectra can be characterized by the two parameters of the model: a single kinetic freeze-out temperature and a common transverse flow velocity.

1.3.3 Anisotropic flow

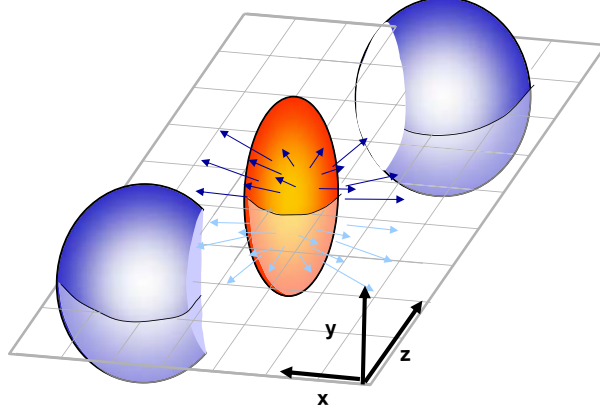


Figure 1.7: Sketch of an almond shaped fireball, where z direction is the collision axis (see text for details).

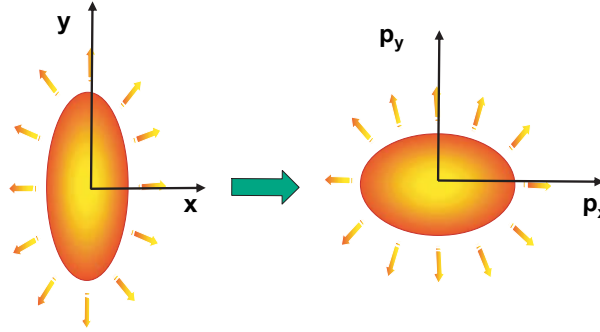


Figure 1.8: Sketch of the formation of anisotropic flow.

In heavy-ions collisions, the size and shape of the collision region depend on the distance between the centers of the nuclei in the transverse plane (impact parameter \mathbf{b}). The plane defined by the beam direction and the impact parameter is called the reaction plane (x - z plane in Fig. 1.7).

In non-central collisions ($\mathbf{b} \neq 0$), the overlapping reaction zone of two colliding nuclei is not spherical (shown in Fig. 1.7). Rescatterings among the system's constituents convert the initial coordinate-space anisotropy into a momentum-space anisotropy since the pressure gradient is not azimuthally symmetric, see Fig. 1.8. The spatial anisotropy is largest early in the evolution of the collision. As the system expands it becomes more spherical, thus this driving force quenches itself. Therefore the momentum anisotropy is particularly sensitive to the early stages of the system evolution [13]. In addition,

because anisotropic flow depends on rescattering, it is sensitive to the degree of thermalization [14, 15] of the system at early time.

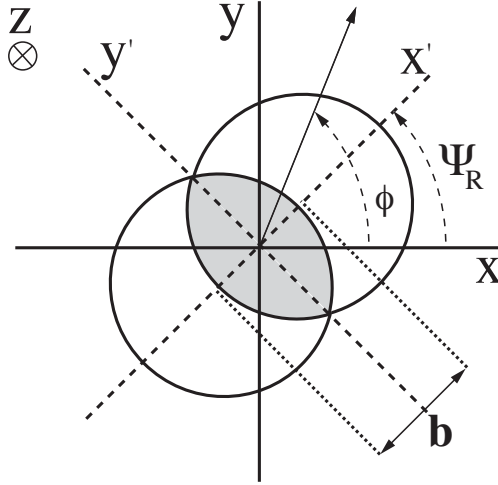


Figure 1.9: Definition of the coordinate system.

Anisotropic flow is usually quantified by the Fourier expansion of the triple differential invariant distribution [16]:

$$E \frac{d^3 N}{d^3 p} = \frac{1}{2\pi} \frac{d^2 N}{p_t dp_t dy} \left(1 + \sum_{n=1}^{\infty} 2v_n \cos(n(\phi - \Psi_r)) \right) \quad (1.5)$$

where the rapidity is defined by the energy E and the longitudinal momentum p_z : $y = \frac{1}{2} \ln\left(\frac{E+p_z}{E-p_z}\right)$, which is an additive variable under Lorentz boosts along the z direction. The azimuthal angle of an outgoing particle is given by ϕ , Ψ_r denotes the reaction plane angle in the laboratory frame (see Fig. 1.9 for the definition of the coordinate system) and n is a positive integer which corresponds to the n^{th} order harmonics. The sine terms vanish due to reflection symmetry with respect to the reaction plane.

The Fourier coefficients are given by

$$v_n = \langle \cos(n(\phi - \Psi_r)) \rangle \quad (1.6)$$

where $\langle \dots \rangle$ indicates an average over the particles in all events under study. The first order harmonics v_1 and the second order harmonics v_2 are usually called directed flow and elliptic flow, respectively.

The initial spatial anisotropy of the created system is quantified by the eccentricity

$$\epsilon_{std} = \frac{\langle y^2 - x^2 \rangle}{\langle y^2 + x^2 \rangle} \quad (1.7)$$

where the x direction is taken along the impact parameter vector and the average is taken over all the interaction points of the system (see Fig. 1.10).

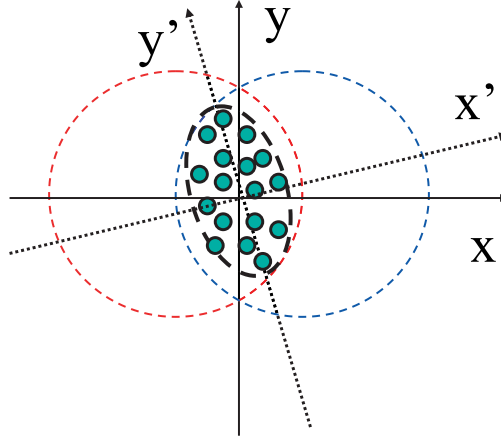


Figure 1.10: An illustration showing the standard eccentricity and the participant eccentricity (see text for details).

However even at fixed impact parameter, the number of individual nucleons participating in the collision as well as their positions in the transverse plane could fluctuate from event to event. As a consequence, the center of the overlap zone can be shifted and the orientation of the principal axes of the interaction zone can be rotated with respect to the conventional coordinate system. To correct for this the participant eccentricity is defined by

$$\epsilon_{part} = \frac{\langle y'^2 - x'^2 \rangle}{\langle y'^2 + x'^2 \rangle} \quad (1.8)$$

where the eccentricity is calculated relative to the new coordinate system defined by the major axis of the initial system (see Fig. 1.10). The eccentricity determined like this is called ϵ_{part} .

The average values of ϵ_{std} and ϵ_{part} are rather similar for all but the most peripheral collisions for interactions of heavy nuclei like Au+Au. For smaller systems, however, fluctuations in the nucleon positions become quite important for all centralities and the average eccentricity can vary significantly depending on how it is calculated [17].

1.4 Model description

In this section a brief description will be given of the theory and phenomenological models used in comparison with the measurements.

1.4.1 Hydrodynamics

Hydrodynamics is a macroscopic approach to describe the dynamical evolution of the expansion stage of a heavy-ion collision. In the model, it is assumed that shortly after the

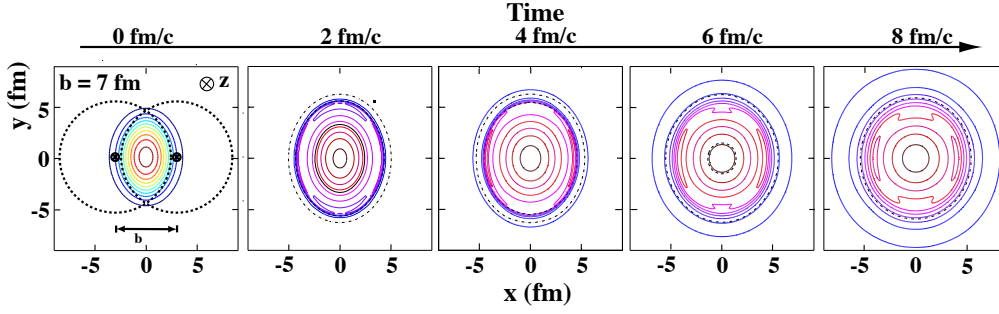


Figure 1.11: The created initial transverse energy density profile and its time dependence in coordinate space for a non-central heavy-ion collision [18]. The z -axis is along the beam direction, the x -axis is defined by the impact parameter \mathbf{b} .

collision the produced strongly interacting matter reaches a state of local thermal equilibrium and subsequently expands adiabatically. The evolution of system is determined by its initial conditions and equation of state (EoS).

The equation of state $p(\epsilon, n)$ which relates energy and baryon density to the pressure is subject to the constraints of local conservation of energy, momentum, and conserved currents (e.g. baryon number),

$$\partial_\mu T^{\mu\nu}(x) = 0 \quad \text{and} \quad \partial_\mu j^\mu(x) = 0, \quad (1.9)$$

The energy-momentum tensor $T^{\mu\nu}$ in the ideal fluid (non-dissipative) is given by

$$T^{\mu\nu}(x) = (\epsilon(x) + p(x))u^\mu(x)u^\nu(x) - g^{\mu\nu}p(x), \quad (1.10)$$

$$j^\mu(x) = n(x)u^\mu(x) \quad (1.11)$$

where $\epsilon(x)$ is the energy density, $p(x)$ the pressure, and $n(x)$ the conserved number density at point x . $u^\mu(x)$ is the local four velocity of the fluid. The equation of state describes how macroscopic pressure gradients generate collective flow. A phase transition from the QGP phase to a hadron gas causes a softening of the EoS: as the temperature crosses the critical temperature, the energy and entropy densities increase rapidly while the pressure rises slowly. The derivative of pressure to energy density, p/ϵ , has a minimum at the end of the mixed phase, known as the softest point. The diminishing driving force slows down the build-up of flow.

The initial conditions which are input parameters, describe the starting time of the hydrodynamic evolution and the relevant macroscopic density distributions at that time. The hydrodynamic evolution is terminated by implementing the freeze-out condition which describes the breakdown of local equilibrium due to decreasing local thermalization rates.

In non-central collisions, driven by its internal asymmetric pressure gradients, the system will expand more strongly in the direction of the reaction plane than perpendicular to the reaction plane. Figure. 1.11 shows the created initial energy density in the transverse plane at different times after thermalization. As time evolves, the system becomes less and less deformed.

1.4.2 RQMD and UrQMD

Relativistic Quantum Molecular Dynamics (RQMD) is a microscopic transport model which combines classical propagation of particle trajectories with stochastic interactions [19, 20]. The created strings and resonances can be excited in elementary collisions and overlapping color strings may fuse into so-called ropes. Subsequently, the fragmentation products from rope, string and resonance decays interact with each other and with the original nucleons, mostly via binary collisions. These interactions drive the system towards equilibration and are the underlying mechanism which makes collective flow develop, even in the preequilibrium stage. In this model, the equilibrium pressure is simply an ideal gas of hadrons and resonances. The resulting equation of state in the cascade mode of RQMD is similar to the one in Ref. [21].

Another widely used model, the Ultra-relativistic Quantum Molecular Dynamics (UrQMD) model is based on analogous principles as RQMD but with a vastly extended collision term [22, 23]. The range of applicability includes the SIS energy region ($\sqrt{s} \approx 2$ GeV) up to the RHIC energy ($\sqrt{s} = 200$ GeV).

1.4.3 AMPT

The AMPT model (A Multi-Phase Transport model) is a hybrid model that uses minijet partons from hard processes and strings from soft processes from the Heavy Ion Jet Interaction Generator (HIJING) model [24] as the initial conditions for modeling heavy ion collisions at ultra-relativistic energies. Time evolution of resulting minijet partons is then described by Zhang's parton cascade (ZPC) [25] model. After minijet partons stop interacting, they are combined with their parent strings. The string fragments into hadrons using the Lund string fragmentation model as implemented in the PYTHIA program [26]. The final state hadronic scatterings are then modeled by a relativistic transport model (ART) [27].

In the AMPT model, there exists a string melting scenario in which hadrons, that would have been produced from string fragmentation, are converted instead to valence quarks and antiquarks with their current quark masses [28]. Interactions among these partons are again described by the ZPC parton cascade model. Since there are no inelastic scatterings, only quarks and antiquarks from the melted strings are present in the partonic matter. The transition from partonic matter to hadronic matter is achieved using a simple coalescence model, which combines two nearest quark and antiquark into mesons and three nearest quarks or antiquarks into baryons or anti-baryons. The particle type is determined by the invariant mass of these partons.

Chapter 2

Experimental Set-up

The anisotropic flow analysis described in this thesis is performed on data taken with the STAR experiment at RHIC. In this chapter, we will introduce the experimental setup, the track reconstruction, the trigger configuration, the centrality definition and the particle identification.

2.1 RHIC

The Relativistic Heavy-Ion Collider (RHIC) at Brookhaven National Laboratory (BNL) is designed to create and investigate strongly interacting matter at high energy densities [29]. It is the first facility capable of colliding heavy ions. The center-of-mass energy in a collision can be up to 200 GeV per nucleon pair which is about a factor of ten larger than the highest energies reached at previous fixed target experiments. RHIC can also perform proton-proton and proton-nucleus collisions in order to understand the initial parton distribution functions of the incident nuclei and for reference data for the heavy ion studies. In addition, there is a program of polarized proton-proton collisions with the top center-of-mass energy of 500 GeV to study the gluon contribution to the spin of the nucleon.

The RHIC complex shown in Fig. 2.1 consists of a Tandem van de Graaff, a Linear Accelerator (Linac), the Booster Synchrotron, the Alternating Gradient Synchrotron (AGS) and ultimately the RHIC synchrotron ring. For gold beam operations, the gold ions with charge $Q = -1e$ are generated in the Pulsed Sputter Ion source and initially accelerated in the Tandem van de Graaff. Passing through a series of stripping foils the ions exit the Van de Graaff with a kinetic energy of 1 MeV per nucleon and a net charge of $Q = +32e$. They are then injected to the Booster Synchrotron and accelerated to 95 MeV per nucleon. After leaving the Booster, the ions are further stripped to $Q = +77e$ and are transferred to the AGS, where they are accelerated to 8.86 GeV per nucleon and sorted into four final bunches. The ions are fully stripped ($Q = +79e$) at the exit of the AGS and transported to RHIC via the AtR beamline. Once injected into RHIC storage ring, the ions are accelerated to collision energy and stored for the data taking. For $p + p$ collisions, protons are injected from the 200 MeV Linac directly into

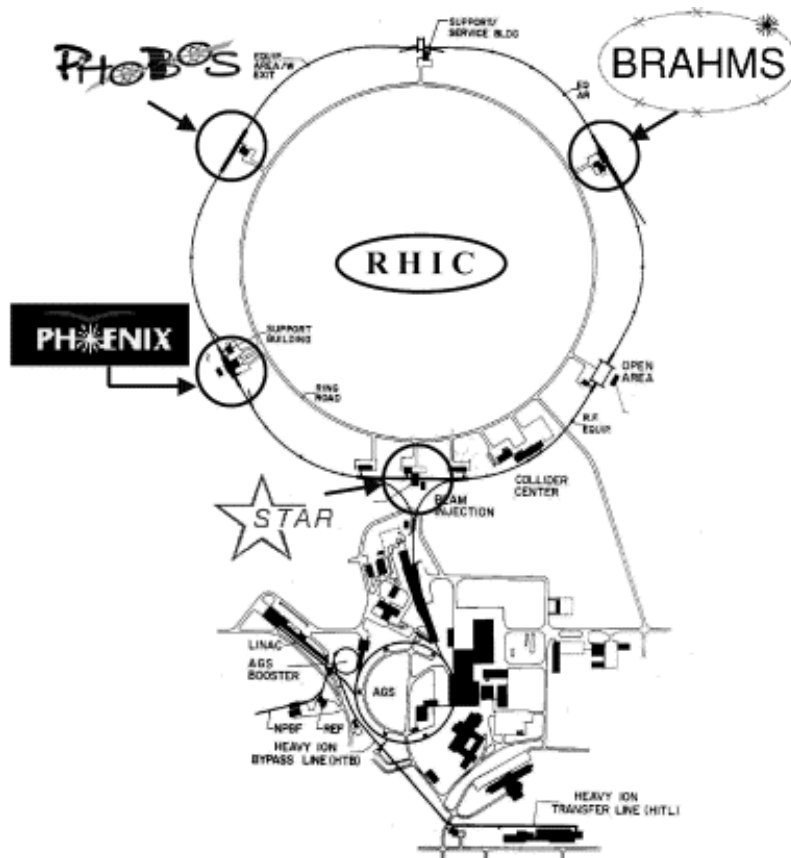


Figure 2.1: RHIC complex

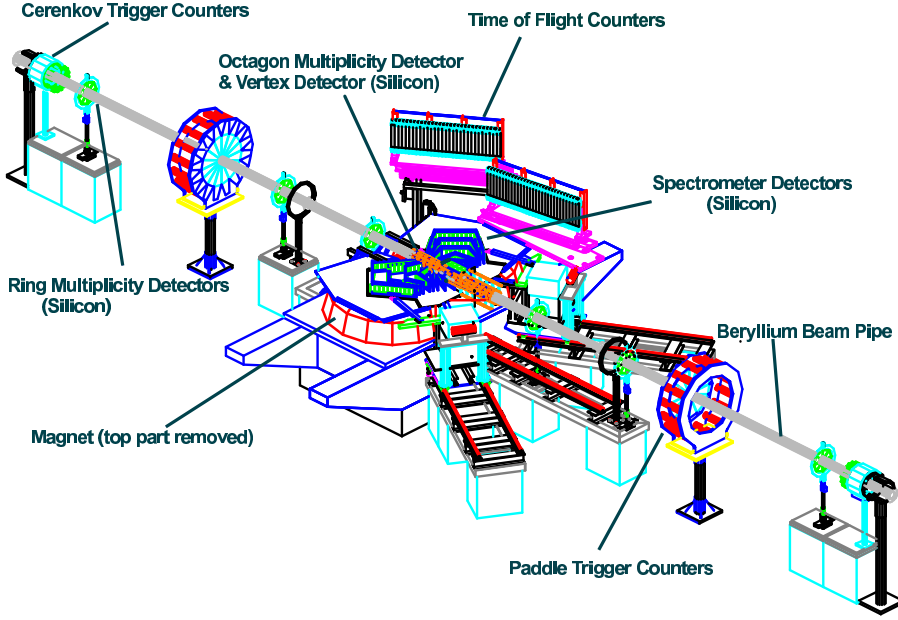


Figure 2.3: Schematic layout of the PHOBOS detector.

as a time-of-flight wall allow for particle identification. Additional detectors include a Vertex detector, sets of scintillator paddles and a Cherenkov detector arrays for vertex determination, event triggering and centrality selection.

PHENIX [32], shown in Fig. 2.4, is designed specifically to measure direct probes such as electrons, muons and photons. Aside from the global detectors for the event characterization, the detectors are grouped into two central arms and two forward muon arms. The central arms, covering the pseudo-rapidity region $|\eta| < 0.35$, consist of tracking subsystems for charged particles and electromagnetic calorimetry. Three sets of Pad Chambers (PC) and the Drift Chambers (DC) are used for the tracking. A Time Expansion Chamber (TEC), a ToF and RICH detectors provide particle identification. A lead-scintillator (PbSc) calorimeter and a lead-glass (PbGl) calorimeter measure the photons and electrons. Two muon spectrometers cover the pseudo-rapidity region $1.1 < |\eta| < 2.4$ and azimuth angle $0 < \phi < 2\pi$.

STAR [33] is a large acceptance solenoidal tracking detector which covers the full azimuth ($0 \leq \phi \leq 2\pi$) for $|\eta| < 1.8$ and $2.5 < |\eta| < 4.0$. The emphasis is on global event characterization, resonance identification, fluctuations and event-by-event observables. The layout of the STAR experiment with the different subsystem is shown in Fig. 2.5 and will be discussed in detail in the next section.

To date, RHIC has run in p+p, d+Au, Au+Au and Cu+Cu configurations.

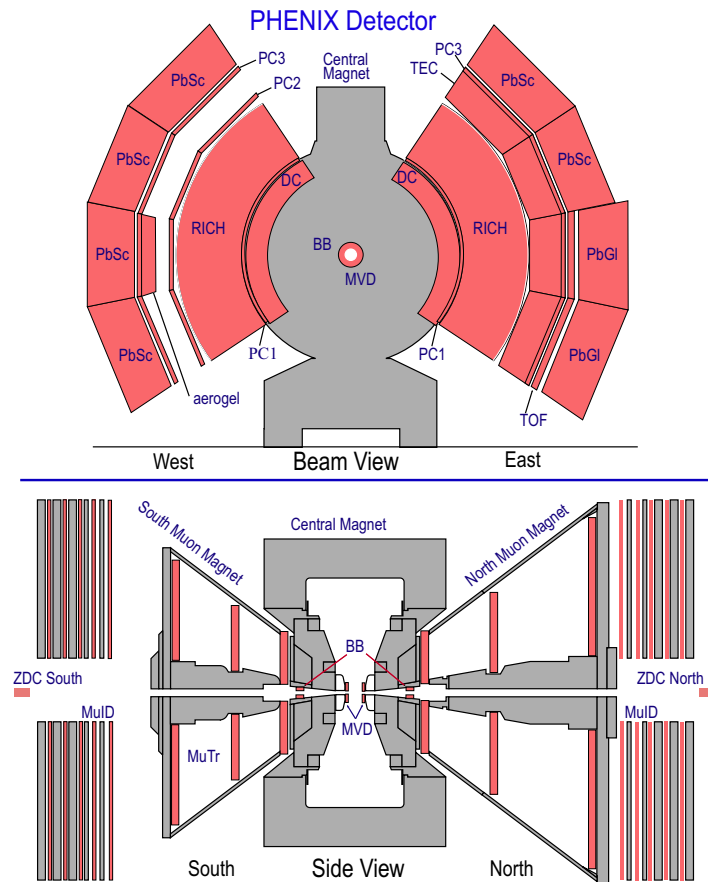


Figure 2.4: Layout of the PHENIX detector.

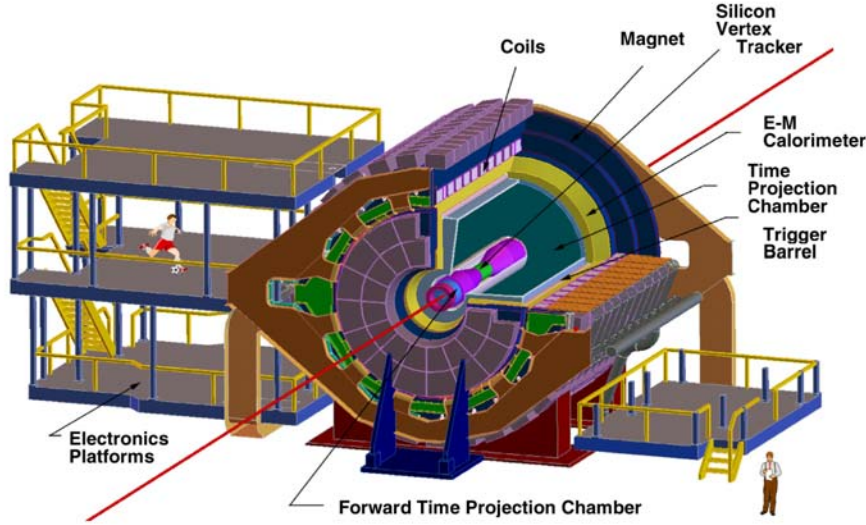


Figure 2.5: Perspective view of the STAR detector

2.2 The STAR Detector

The Solenoidal Tracker at RHIC (STAR) was designed primarily to measure hadron production over a large solid angle, featuring detector systems for high precision tracking, momentum analysis, and particle identification at mid-rapidity [33]. The large acceptance of STAR makes it particularly well suited for event-by-event characterizations of heavy-ion collisions and for the detection of hadron jets.

A cutaway side-view of the STAR detector in the configuration for the RHIC 2001 run is displayed in Fig. 2.6. A room temperature solenoidal magnet with a maximum magnetic field of 0.5 T provides a uniform magnetic field for charged particle momentum analysis. Charged particle tracking close to the interaction region is accomplished by a Silicon Vertex Tracker (SVT) consisting of 216 silicon drift detectors arranged in three cylindrical layers. The Silicon Strip Detectors (SSD) completes the inner tracking layers with a pseudo-rapidity coverage $|\eta| \leq 1$ and complete azimuthal symmetry $0 < \phi \leq 2\pi$. Silicon tracking close to the interaction is used to localize the primary interaction vertex and to identify secondary vertexes from weak decays. A large volume Time Projection Chamber (TPC) for charged particle tracking and particle identification is located at a radial distance from 50 to 200 cm from the beam axis. The TPC covers a pseudo-rapidity range $|\eta| < 1.8$ for tracking with complete azimuthal symmetry. Both the SVT and TPC contribute to particle identification using ionization energy loss. To extend the tracking to the forward region, a radial-drift TPC (FTPC) is installed covering $2.5 < |\eta| < 4$, also with complete azimuthal coverage and symmetry. Two time-of-flight (TOF) module prototypes based on scintillator materials (TOFp) and multi-gap resistive plate chamber technology (TOFr) respectively are placed outside of TPC to test the

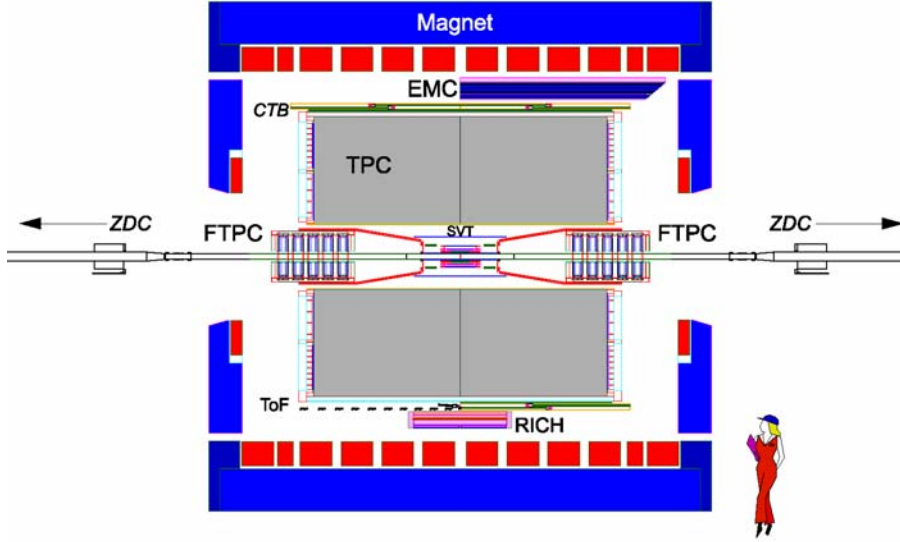


Figure 2.6: Cutaway side view of the STAR detector as configured in 2001

performance of the upcoming full barrel TOF upgrade which will extend the capability of particle identification of STAR. A barrel electromagnetic calorimeter (EMC) and an endcap electromagnetic calorimeter (EMC) are designed to measure the transverse energy of events, and trigger on and measure high transverse momentum photons, electrons, and electromagnetically decaying hadrons. The EMC's include shower-maximum detectors to distinguish high momentum single photons from photon pairs resulting from π and η meson decays. The EMC and the EMC provide coverage of $-1 < \eta < 1$ and $-1 < \eta < 2$ respectively, with the full azimuthal coverage.

In addition, fast detectors operate as the main trigger detectors: a central trigger barrel (CTB), two zero-degree calorimeters (ZDC) and two beam-beam counters (BBC).

The CTB consists of 240 scintillator slats arranged around the outer cylinder of the TPC. With full azimuthal coverage over $|\eta| < 1$, it triggers on the central collisions and measures the charged multiplicity in the mid-rapidity region.

The ZDCs are located on the beam axis at ± 18 m away from the TPC center, covering polar angle $\theta < 2.5$ mrad. They measure neutrons at beam rapidity originating from the break up of the colliding nuclei, while charged fragments get swept away by the the same beam steering magnets that bend the incoming nuclei towards the interaction point. The number of the neutrons detected in the ZDCs can be identified with the amount of energy deposited in the collision. The ZDCs are used for triggering as well as monitoring the beam luminosity. In addition the comparison of timing signal from the two ZDCs can give a measure of the interaction location.

The BBC subsystem consists of two disk shaped scintillating detectors situated ± 3.5 m from the interaction point, covering pseudorapidity $3.3 < |\eta| < 5.0$. Each BBC disk is composed of scintillating tiles that are arranged in a hexagonal closest packing. The BBCs are sensitive to the high-energy hadrons that are focused in the high (near beam)

rapidity region. The z position of the main interaction vertex can also be selected with the timing signal difference of the two BBCs.

2.2.1 STAR TPC

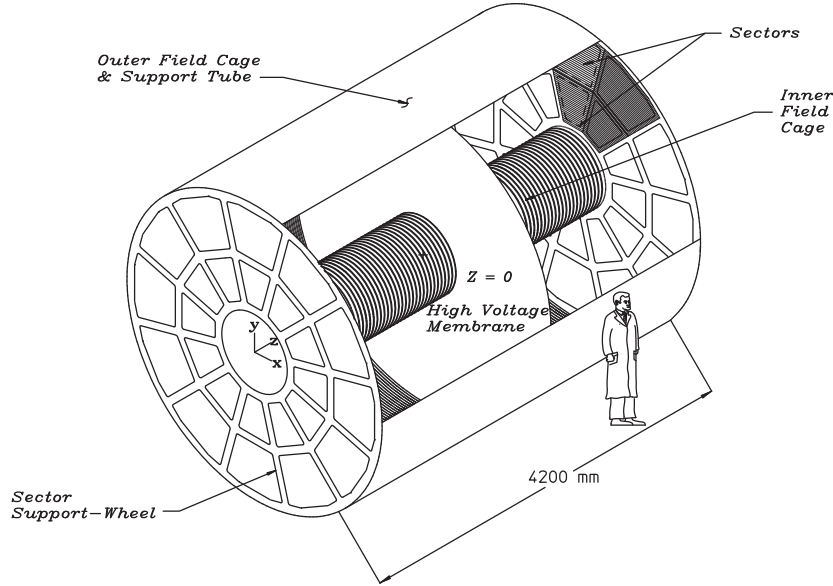


Figure 2.7: Sectioned view of the STAR TPC.

As the primary tracking device [34], the STAR TPC records the tracks of particles, measures their momenta, and identifies the particles by measuring their ionization energy loss (dE/dx). It covers a pseudorapidity range ($|\eta| < 1.8$) with a full azimuth ($0 < \pi < 2\pi$).

The TPC is a cylinder 4.2 m long and 4.0 m in diameter, as shown schematically in Fig. 2.7. Located in a large solenoidal magnet that operates up to 0.5 T, the TPC is divided into two drift regions by the central membrane which is typically held at 28 KeV. The central membrane, the concentric field cage cylinders and the readout end caps provide an uniform electric field of approximately 135 V/cm. Electric field uniformity is critical since any distortions will result in a distortion of the recorded tracks. The TPC is filled with a mixture of 10% methane and 90% argon gas in which the electron drift velocity is around 5.45 cm/ μ s.

The end-cap readout planes at each side of the TPC are organized into 12 sectors. The geometry of one sector is shown in Fig. 2.8. Each sector is further divided into an inner and outer sector. The inner sector has 1750 pads, each with 11.5 mm in the radial

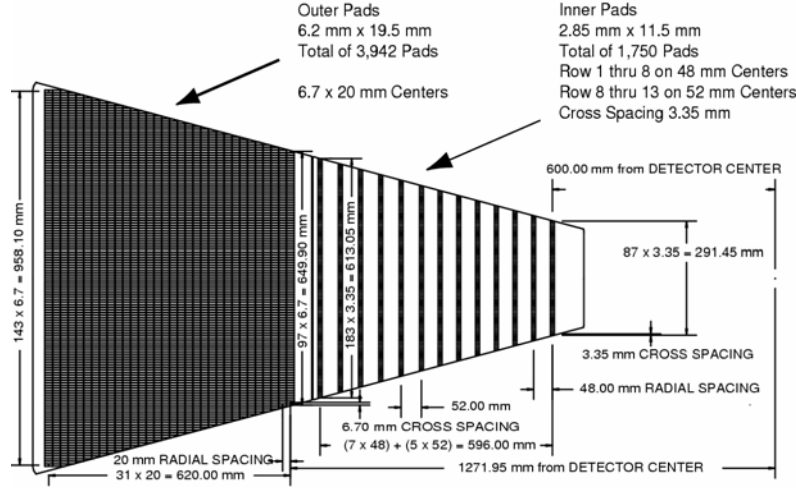


Figure 2.8: The anode pad plane of one full sector shown. The inner sub-sector has small pads arranged in widely spaced rows. The outer sub-sector is densely packed with larger pads.

direction and 2.85 mm in the tangential direction. They are grouped into 13 pad rows. The outer sector has 3940 pads, and the corresponding dimensions are 19.5 mm (radial) and 6.2 mm (tangential). The outer sector pads are combined into 32 rows. The inner sector pads are smaller in order to improve two-track resolution. Its size is limited by the diffusion limit of the TPC. Combining the inner and outer sector, there are a total of 5,690 pads per sector which corresponds to a total of 136,560 channels for all 24 TPC sectors.

The readout system is based on Multi-Wire Proportional Chambers (MWPC) with readout pads. Figure 2.9 shows a cutaway view of the readout pad planes of an outer sector. The MWPC consists of the gating grid, the ground grid and the anode grid. The gating grid separates the drift region from the amplification region. This grid controls the entry of electrons from the TPC drift volume into the MWPC and allows the drift electrons to pass through while the event is being recorded. The ground grid is used to terminate the field in the avalanche region as well as calibrate the pad electronics. The anode wires are held at a high voltage and provide the necessary electric field to avalanche the electrons from the track ionization. The avalanche leaves a cloud of positive ions, and the readout pads image their charge. The signal measured on the pads is then amplified, integrated and digitalized by the front-end electronics. These circuits can sample the arrival of electrons into at most 512 time buckets as well. The position of the ionizing particle along the drift direction (z coordinate) is reconstructed by the time bucket and the drift velocity. The x and y coordinates are determined by the location of the readout pad.

When a charged particle transverses the TPC gas volume, it ionizes gas atoms and molecules every few tenths of a millimeter along its path and leaves behind a clusters

of electrons. Under the influence of an externally applied electric field, the electron clusters are then drifted at a constant average velocity to the end caps, where their time of arrival and location are recorded.

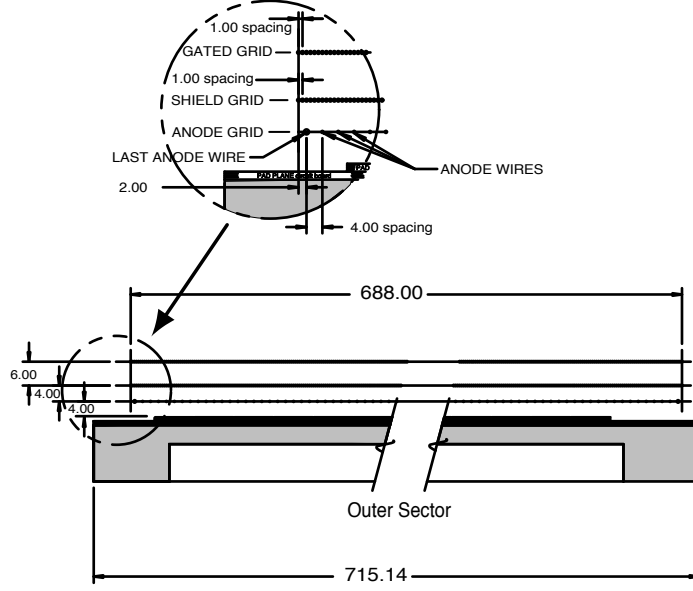


Figure 2.9: A cutaway view of an outer sub-sector pad plane.

The reconstruction of events in the TPC consists of the following steps: cluster finding, global track-finding and fitting, primary vertex fitting, and primary track re-fitting. A cluster finder gathers the TPC data into clusters in 2D space and time direction. They are subsequently converted into 3D space points in the global STAR coordinate system, where drift velocity and trigger-time offset are taken into account. Their integrated and gain calibrated charge is used for particle identification via the dE/dx measurement. Operating on these space points, the Time Projection Chamber Tracker (TPT) finder works its way from the outer padrows inwards, gathering space points into tracks and determine their 3D momentum using a helix fit. These tracks are then passed through a Kalman filter, calculating the track parameters while taking energy loss and multiple scattering in the beam pipe and detector materials into account. These global tracks are then extrapolated towards the beam axis in the center of the TPC and a common origin is sought, which is identified as the primary vertex. Once the primary vertex is found, all global tracks which point back to the newly found primary vertex by distance of closest approach (DCA) less than 3 cm are selected and refitted using a constrained Kalman fit that forces the tracks to originate from the primary vertex. These tracks are labeled as primary tracks.

From simulations, it is known that the tracking efficiency depends on the multiplicity, p_t and particle type etc. In general, it is larger than 80% in the region $p_t > 200$ GeV/ c . The primary vertex resolution is $350 \mu\text{m}$ in events with more than 1000 tracks.

The global event reconstruction offline software integrates all the tracking, timing, and energy deposition information from the different detector subsystems and produces the overall event characteristics of the triggered events into a Data Summary Tape (DST) format for the physics analysis.

2.2.2 STAR FTPCs

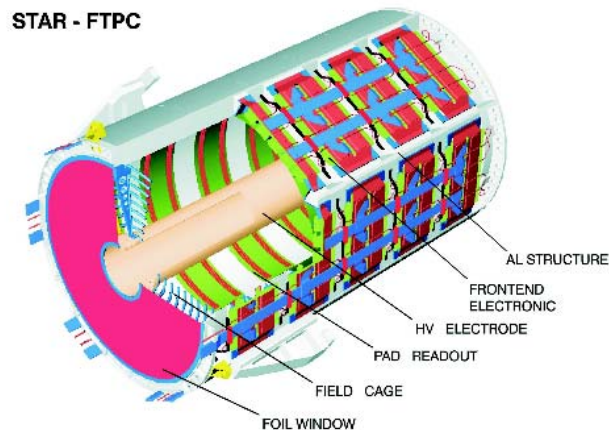


Figure 2.10: Schematic diagram of an FTPC for the STAR experiment

The Forward Time Projection Chambers (FTPC) were constructed to extend the acceptance of the main TPC [35]. They cover the pseudorapidity range of $2.5 < |\eta| < 4.0$ on both sides of STAR and measure momenta and production rates of charged particles as well as neutral strange particles.

The FTPC illustrated in Fig. 2.10 is a cylindrical structure, 75 cm in diameter and 120 cm long, with a radial drift, and readout chambers located in 5 rings on the outer cylinder surface. Each ring has two padrows and is subdivided azimuthally into 6 readout chambers. The radial drift field, perpendicular to the magnetic field, was chosen to improve the two-track separation in the region close to the beam pipe where the particle density is highest. The field cage is formed by the inner HV-electrode, a thin metalized plastic tube, and the outer cylinder wall at ground potential. The field region at both ends is closed by concentric rings. The front-end electronics, which amplifies, shapes, and digitizes the signals, is mounted on the back of the readout chambers. Each particle trajectory is sampled up to 10 times. The ionization electrons are drifted to the anode sense wires and the induced signal on the adjacent cathode surface is read out by 9600 pads. The filled gas is a mixture of 50% Ar and 50% CO₂.

The reconstruction of tracks in FTPC proceeds in two steps. The first step is to calculate the track points (cluster finding) from the charge distribution measured by the pads. In the second step (track finding), these track points of different padrows are grouped to tracks. Using the magnetic field map, the up to ten position measurements per track are then used to fit the momentum.

The FTPCs obtain a position resolution of $100\ \mu\text{m}$, a two-track separation of $1 - 2\ \text{mm}$, a momentum resolution between 12% and 15%, and overall reconstruction efficiency between 70% and 80%.

2.2.3 Trigger

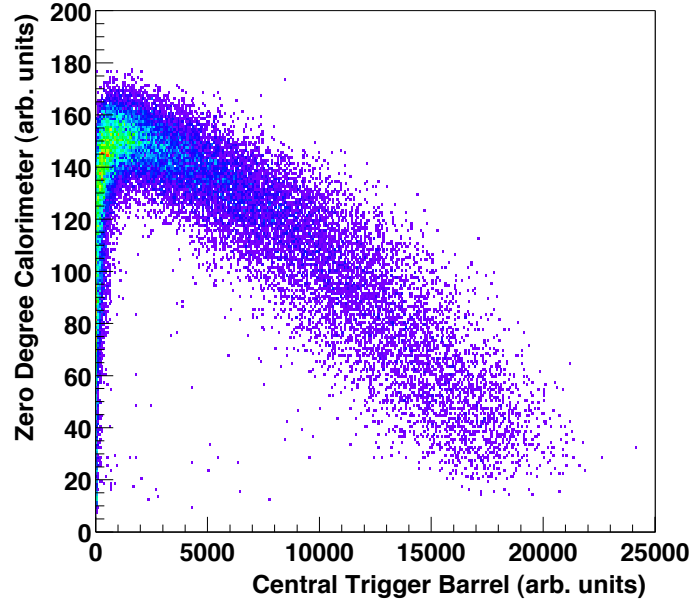


Figure 2.11: Correlation between the summed pulse heights from the ZDC and the CTB for events with a primary collision vertex reconstructed from tracks in the TPC.

The STAR trigger system is a 10 MHz pipelined system which is based on input from fast detectors to control the event selection for the much slower tracking detectors [36]. Interactions are selected according to the distributions of particles and energy obtained from the fast trigger detectors. As an example, Fig. 2.11 shows the correlation between the summed ZDC pulse height and that of the CTB for events with a primary collision vertex reconstructed from tracks in the TPC. The largest number of events occurs for large ZDC values and small CTB values, which corresponds to collisions at large impact

parameters. Collisions at progressively smaller impact parameters result in less energy in the forward direction (smaller pulse heights in ZDC) and more energy in the side-ward direction (larger pulse heights in CTB). This correlation between the ZDC and CTB is used in the experiment to provide a centrality selection trigger for the collision. The ZDC is double-valued since collisions at either small or large impact parameter can result in a small amount of energy in the forward ZDC direction.

The typical trigger configurations are a minimum bias trigger and a central trigger. The minimum bias trigger intends to maximize acceptance of inelastic Au+Au collisions at all impact parameters. The central trigger is defined to accept most central collisions.

Of interest to the anisotropic flow analysis is the minimum bias trigger configuration. Table 2.1 lists cuts for the minimum bias trigger selection in Au+Au collisions at $\sqrt{s_{NN}} = 200$ GeV and $\sqrt{s_{NN}} = 62.4$ GeV. It was required that the pulse heights in both ZDCs or BBCs are above a threshold. The CTB portion of the trigger condition was imposed to reject non-hadronic events. Offline vertex cuts along the beam axis (z axis) were applied to remove the ZDC or BBC bias.

Table 2.1: Minimum bias trigger selection in Au+Au collisions at $\sqrt{s_{NN}} = 200$ GeV and $\sqrt{s_{NN}} = 62.4$ GeV.

Collisions	Online Cuts	Offline vertex cut
AuAu 200 GeV	ZDCs>threshold and CTBsum > 75	$ z < 30$ cm
AuAu 62.4 GeV	ZDCs>threshold or CTBsum > 15	$ z < 30$ cm

2.2.4 Centrality definition

In heavy ion collisions, the system created in a head-on collisions is different from that in a peripheral collisions. Therefore, collisions are categorized by their centrality. Theoretically, the centrality is characterized by the impact parameter \mathbf{b} which is the distance between the centers of two colliding heavy ions. Instead of by impact parameter, the centrality is often characterized by the number of participating nucleons N_{part} or by the number of binary collisions N_{bin} . A participating nucleon N_{part} or wounded nucleon N_{wounded} is defined as a nucleon which undergoes at least one inelastic nucleon-nucleon collision. The binary collision N_{bin} is defined as the total number of inelastic nucleon-nucleon collisions. The soft particle production scales with the number of participating nucleons whereas hard processes scale with the number of binary collisions. These measures can be related to the impact parameter \mathbf{b} using a Glauber calculation, see Fig. 2.12 as an example for Au+Au collisions at top RHIC energy.

The Glauber model is a multiple collision model which treats a nucleus-nucleus collision as an independent sequence of nucleon-nucleon collisions, see [37] and references therein. In the Glauber calculation, the nucleons in a nucleus are distributed according to the Woods-Saxon distribution:

$$\rho(r) = \frac{\rho_0(1 + wr^2/R^2)}{1 + e^{(r-R)/a}} \quad (2.1)$$

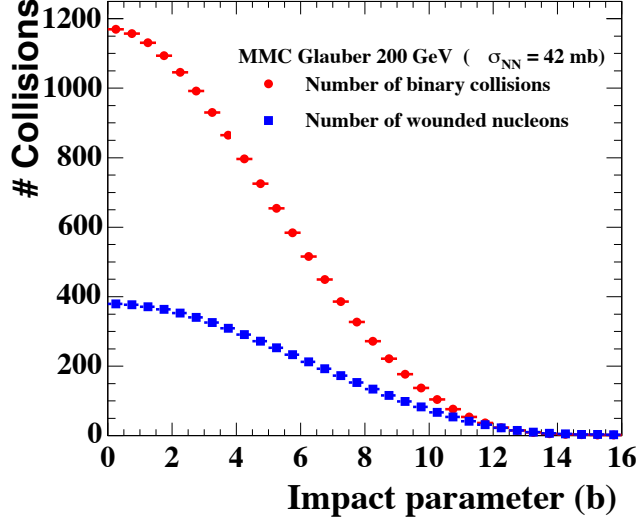


Figure 2.12: Number of participating nucleons and binary collisions versus impact parameter.

where ρ_0 corresponds to the nucleon density in the center of the nucleus, R corresponds to the nuclear radius, a to the skin depth and w characterizes deviations from a spherical shape. For the case of ^{197}Au , the parameters are $R = 6.38$ fm, $a = 0.535$ fm and $w = 0$. For the case of ^{63}Cu , the parameters are $R = 4.20641$ fm, $a = 0.5977$ fm and $w = 0$.

The model assumes that nucleons in each nucleus travel on straight-line trajectories through the colliding system and interact according to the inelastic cross section, σ_{inel}^{NN} , as measured in p+p collisions. At RHIC energies, the values used for σ_{inel}^{NN} are 32.3, 35.6, 40, and 42 mb at $\sqrt{s_{NN}} = 19.6, 62.4, 130$ and 200 GeV respectively.

The Glauber calculation can be implemented either by the optical model or in a Monte Carlo generator. The optical model is based on an analytic method of classically overlapping nuclei. The Monte Carlo approach is based on a computer simulation of billiard ball like colliding nucleons.

Experimentally, the collision centrality can be inferred from the measured particle multiplicities if one assumes that this multiplicity is a monotonic function of \mathbf{b} . When the total integral of the multiplicity distribution is known, centrality classes are defined by binning the distribution based upon the fraction of the total integral. Alternative centrality classification can be made by studying the correlation of beam rapidity spectator multiplicity with mid-rapidity particle production [38–41].

However, neither N_{part} nor N_{bin} can be measured directly in the experiment. Their values can be extracted by mapping the measured data, *i.e.*, the per-event charged particle multiplicity (dN/dN_{ch}) distribution to the corresponding distribution obtained from Glauber calculations. This is done by defining centrality classes in both the measured and calculated distributions and then connecting the mean values from the same cen-

trality class in the two distribution.

For the Au+Au collisions in STAR, the centrality selection is based on the uncorrected primary charged particle multiplicity in the pseudorapidity region $|\eta| < 0.5$ as measured by the TPC. The centrality classes are calculated as fraction of this multiplicity distribution. Glauber calculations are performed using a Monte Carlo calculation. The centrality bin defined as 0–5% corresponds to the most central collisions amounting to 5% of the total cross section, while 70–80% is the most peripheral collisions. Minimum bias refers to 0 to 80% of the most central hadronic cross section. The calculated $d\sigma/dN_{\text{part}}$ or $d\sigma/dN_{\text{bin}}$ distribution is divided into bins corresponding to common fraction of the total geometric cross section to extract the average N_{part} or N_{bin} for each centrality bin.

Table 2.2 and Table 2.3 list the fraction of the cross section, the reference multiplicity, the number of participating nucleons and the number of binary collisions for each selected centrality bin in Au+Au collisions at 200 and 62.4 GeV, respectively.

Table 2.2: Centrality selection, the reference multiplicity, the number of participating nucleons and the number of binary collisions in 200 GeV Au +Au collisions.

Centrality	RefMult	$\langle N_{\text{part}} \rangle$	$\langle N_{\text{bin}} \rangle$
70% – 80%	14 – 31	$14.1 + 3.6 - 5.0$	$12.3 + 4.4 - 5.2$
60% – 70%	31 – 57	$27.4 + 5.5 - 7.5$	$29.5 + 8.2 - 11.3$
50% – 60%	57 – 96	$47.8 + 7.6 - 9.5$	$63.9 + 14.1 - 18.9$
40% – 50%	96 – 150	$76.6 + 8.5 - 10.4$	$123.4 + 22.7 - 27.3$
30% – 40%	150 – 222	$115.5 + 8.7 - 11.2$	$220.2 + 30.0 - 38.3$
20% – 30%	222 – 319	$166.7 + 9.0 - 10.6$	$368.6 + 41.1 - 50.6$
10% – 20%	319 – 441	$234.6 + 8.3 - 9.3$	$591.3 + 51.9 - 59.9$
5% – 10%	441 – 520	$299.3 + 6.6 - 6.7$	$827.9 + 63.9 - 66.7$
0 – 5%	≥ 520	$352.4 + 3.4 - 4.0$	$1051.3 + 71.5 - 71.1$

2.2.5 Particle Identification: $\frac{dE}{dx}$

Charged particles passing through the TPC will lose energy via ionization. The charge collected for each hit on a track is proportional to the energy loss of the particle. For a particle with charge Z (in units of e) and speed $\beta = v/c$ transversing a medium with density ρ , the mean energy loss is described by the Bethe-Bloch formula

$$\left\langle \frac{dE}{dx} \right\rangle = 2\pi N_0 r_e^2 m_e c^2 \rho \frac{Zz^2}{A\beta^2} \left[\ln \frac{2m_e \gamma^2 v^2 E_M}{I^2} - 2\beta^2 \right] \quad (2.2)$$

where N_0 is Avogadro's number, m_e is the electron mass, $r_e (= e^2/m_e)$ is the classical electron radius, c is the speed of light, z is the atomic number of the absorbing material, A is the atomic weight of the absorbing material, $\gamma = 1/\sqrt{1 - \beta^2}$, I is the mean excitation energy, and $E_M (= 2m_e c^2 \beta^2 / (1 - \beta^2))$ is the maximum transferable energy in a single collision [42].

Table 2.3: Centrality selection, the reference multiplicity, the number of participating nucleons and the number of binary collisions in 62.4 GeV Au +Au collisions.

Centrality	RefMult	$\langle N_{\text{part}} \rangle$	$\langle N_{\text{bin}} \rangle$
70% – 80%	9 – 20	13.01 + 3.36 – 4.58	11.23 + 3.69 – 4.78
60% – 70%	20 – 38	25.91 + 5.59 – 5.58	26.85 + 8.76 – 9.00
50% – 60%	38 – 65	45.79 + 7.03 – 6.99	56.61 + 15.06 – 14.35
40% – 50%	65 – 102	74.15 + 9.01 – 8.51	109.30 + 22.36 – 22.33
30% – 40%	102 – 154	112.03 + 9.62 – 9.06	193.45 + 31.85 – 30.94
20% – 30%	154 – 222	162.15 + 10.02 – 9.47	320.87 + 42.87 – 39.14
10% – 20%	222 – 313	228.99 + 9.20 – 7.75	511.74 + 54.91 – 47.53
5% – 10%	313 – 373	293.26 + 7.13 – 5.60	713.72 + 63.47 – 54.78
0 – 5%	≥ 373	347.26 + 4.26 – 3.75	904.27 + 67.68 – 61.99

It is seen from the equation that the different particle species with the same momentum p have different amounts of mean energy loss. The charged particles therefore can be identified by their specific energy loss.

A track crossing the entire TPC has 45 dE/dx samples, which are distributed according to the Landau probability distribution. One of the properties of this distribution is that its tail dies off very slowly, and the dispersion of values around the mean is very large. A typical procedure to reduce fluctuations from the Landau tails is to truncate the distribution. In STAR, the highest 30% ionization values are removed and the truncated mean $\langle dE/dx \rangle$ is then determined from 70% of the samples. Fig. 2.13 shows the energy loss for particles in the TPC as a function of momentum.

In order to quantitatively describe the particle identification, a variable is defined (in the case of charged pion identification) as

$$n\sigma_\pi = \ln\left[\frac{dE}{dx}_{\text{meas.}} - \langle \frac{dE}{dx} \rangle_\pi\right] / \sigma_{dE/dx} \quad (2.3)$$

in which $\frac{dE}{dx}_{\text{meas.}}$ is the measured energy loss of a track and $\langle \frac{dE}{dx} \rangle_\pi$ is the expected mean energy loss for charged pions. $\sigma_{dE/dx}$ denotes the resolution of specific ionization in the TPC. For the identification of charged kaons, protons and anti-protons, a similar definition can be given by $n\sigma_K$, $n\sigma_p$, $n\sigma_{\bar{p}}$. The different particle species can be selected by applying the cuts on the variables.

The typical resolution of dE/dx in Au+Au collisions is $\sim 8\%$, which allows for the π/K separation up to $p \sim 0.7$ GeV/ c and proton/meson separation up to $p \sim 1.1$ GeV/ c .

Recently, a new technique was developed to extend the pions and (anti)protons identification to high momentum ($p > 2.5$ GeV/ c) [43,44]. This method is based on the clear separation of the mean dE/dx for different particles in the relativistic rise region of dE/dx . The pions are separated from kaons and protons on the level $1.5 - 3.0\sigma$. The dE/dx separation between kaon and proton is 1σ or less, which is insufficient for proton-kaon identification. The method is confirmed by the STAR TOF measurements.

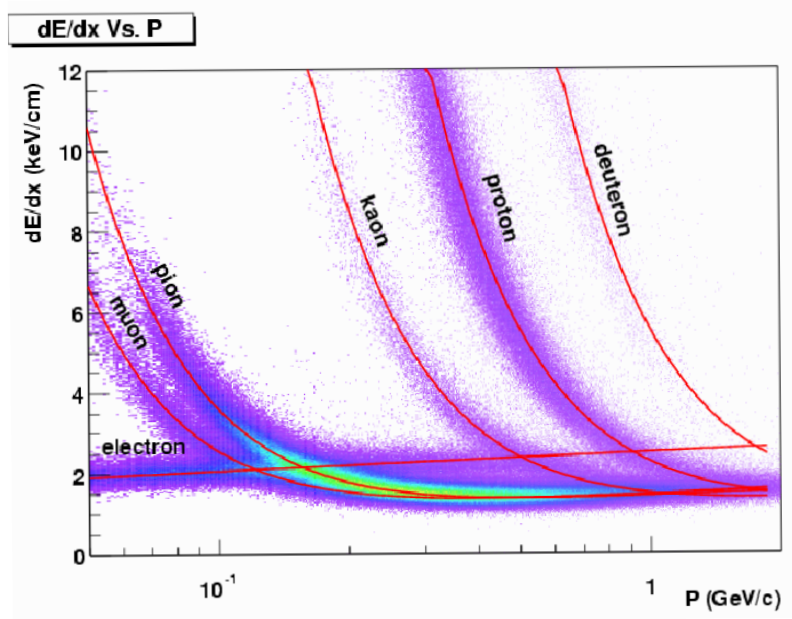


Figure 2.13: The energy loss distribution as a function of p_t in the TPC.

The neutral particles, such as K_S^0 and Λ , can be reconstructed from the topology of their decay daughters detected in the TPC and thus can be measured at larger p_t .

Chapter 3

Flow analysis method

In order to obtain accurate measurements of anisotropic flow in the experiment and estimate the systematic uncertainties, several analysis methods have been developed. The event plane method and the cumulant method are applied to the data for this analysis. In this chapter, in addition to these two approaches, we also briefly review two related methods, the scalar product method and Lee-Yang zeros method.

3.1 Two particle correlation

3.1.1 Event plane method

Anisotropic flow is defined as a correlation between the emitted particles and the direction of the impact parameter in a collision. The standard event plane method is proposed to study flow by reconstructing the reaction plane Ψ_r [45]. The estimated reaction plane is called the event plane. Starting from the n^{th} harmonic event flow vector Q_n whose x and y components are given by

$$Q_n \cos(n\Psi_n) = \sum_i w_i \cos(n\phi_i) \quad (3.1)$$

$$Q_n \sin(n\Psi_n) = \sum_i w_i \sin(n\phi_i) \quad (3.2)$$

The n^{th} harmonic event plane can be obtained:

$$\Psi_n = \left(\tan^{-1} \frac{\sum_i w_i \sin(n\phi_i)}{\sum_i w_i \cos(n\phi_i)} \right) / n, \quad (3.3)$$

where ϕ is the azimuthal angle of a particle. The sum runs over the particles used in the event plane determination. w_i are the weights to optimize the event plane resolution. For example transverse momentum of the particles can be taken as weights. As long as the colliding nuclei are not polarized, any ensemble of events should have randomly distributed azimuthal angles of the reaction planes. A straightforward detector-induced

bias is non-uniform azimuthal coverage which can be corrected for as long as the non-uniformities are small. Several procedures aiming at flattening the event plane azimuthal distribution have been developed [45, 46]. One of most commonly used methods is to use the distribution of the particles themselves as a measure of the acceptance. One accumulates the laboratory azimuthal distribution of the particles for all events and uses the inverse of this as other weights in the calculation of the event planes. Figure 3.1 shows the ϕ weight distribution calculated from different part of the TPC in STAR. The 2nd order event plane distribution for minimum bias data in Au+Au collisions at 62.4 GeV is shown in Fig. 3.2. A particle is then correlated with the event plane estimated above to evaluate the flow coefficients. This particle has to be subtracted from the event plane calculation to avoid the trivial autocorrelation.

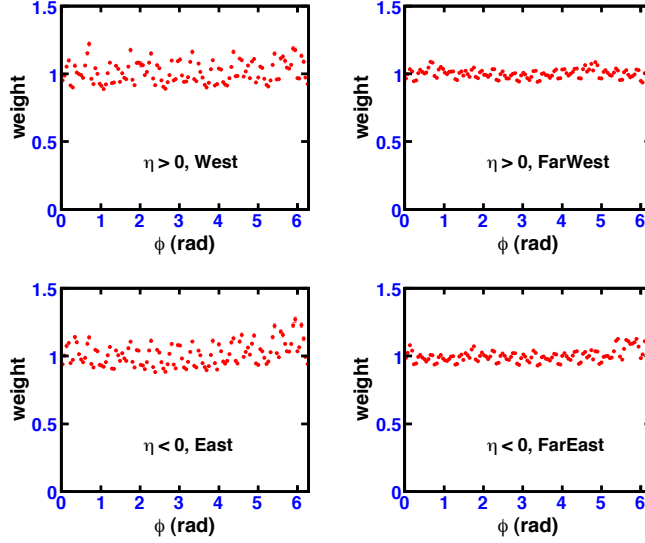


Figure 3.1: The ϕ weight distributions for the top 5% centrality in Au+Au collisions at $\sqrt{s_{NN}} = 62.4$ GeV.

Since the event plane is only an approximation to the true reaction plane, the observed n^{th} order flow coefficients $v_p^{obs} = \langle \cos(mn(\phi - \Psi_n)) \rangle$ has to be corrected up by the even plane resolution,

$$v_p = \frac{v_p^{obs}}{\langle \cos(mn(\Psi_n - \Psi_r)) \rangle}, \quad (3.4)$$

where p is a multiple of n ($p = mn$). This indicates that the higher order harmonics v_p can be measured relative to the lower order event plane Ψ_n . If the first order event plane is determined, it becomes possible to obtain all v_p . However, the event plane resolution becomes worse as the relative harmonic order m increases [45]. At ultra-relativistic energies, the second order event plane Ψ_2 has the highest resolution. Elliptic

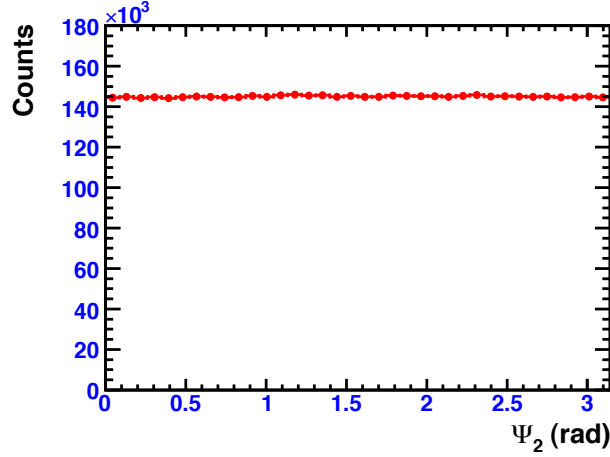


Figure 3.2: The 2th order event plane distribution in Au+Au collisions at 62.4 GeV.

flow and the higher order even harmonics estimated with respect to the Ψ_2 are denoted as $v_2\{EP_2\}$, $v_4\{EP_2\}$ etc.

The event plane resolution for a full event is estimated from the correlation of the planes of independent sub-events Ψ^a , Ψ^b . In the most common case, each event is randomly divided into two statistically equivalent sub-events. Assuming the resolution for each sub-event is the same, then the sub-event resolution is expressed as

$$\langle \cos(mn(\Psi_n^a - \Psi_r)) \rangle = \sqrt{\langle \cos(mn(\Psi_n^a - \Psi_n^b)) \rangle} \quad (3.5)$$

In fact, the event plane resolution can be evaluated analytically [16, 47, 48],

$$\langle \cos(mn(\Psi_n - \Psi_r)) \rangle = \frac{\sqrt{\pi}}{2\sqrt{2}} \chi_n \exp(-\chi_n^2/4) [I_{\frac{m-1}{2}}(\chi_n^2/4) + I_{\frac{m+1}{2}}(\chi_n^2/4)] \quad (3.6)$$

where $\chi_n = v_n \sqrt{2N}$ is a variable proportional to flow signal and to the number of particles N used to determine the event plane. I_ν is the modified Bessel function of order ν . Since the sub-event resolution is known, the root χ_n can be solved using an iterative routine. The full event plane resolution is then obtained by replacing the χ by $\sqrt{2}\chi$. Figure 3.3 shows the 2nd order event plane resolution determined in Au+Au collisions at 62.4 GeV for 9 different centrality classes.

3.1.2 Scalar product method

Anisotropic flow can also be measured without estimating the reaction plane. It is calculated directly by projecting the unit vector $u(\eta, p_t)$ of the analyzed particles on the

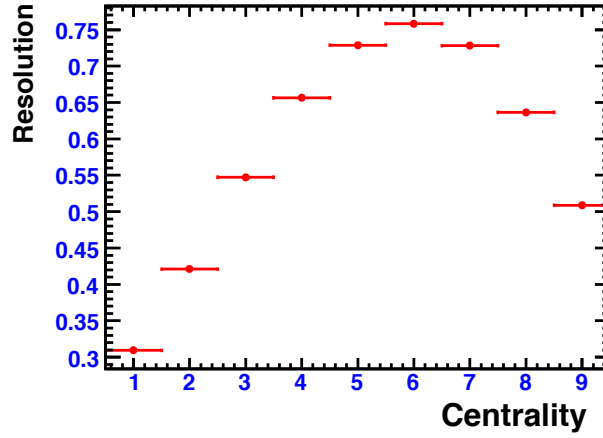


Figure 3.3: The 2nd order event plane resolution in 62.4 GeV Au+Au collisions for 9 different centrality intervals.

event flow vector Q [49].

$$v_n(\eta, p_t) = \frac{\langle Q_n \cdot u(\eta, p_t) \rangle}{2\sqrt{\langle Q_n^a \cdot Q_n^b \rangle}} \quad (3.7)$$

where $u = e^{in\phi}$ is the unit vector of a particle. The vectors Q_n^a and Q_n^b are constructed from the subevents a and b . The correlation between these two subevents is

$$\langle Q_n^a \cdot Q_n^b \rangle = \langle v_n^2 M^a M^b \rangle \quad (3.8)$$

where M^a and M^b are the multiplicities for subevents a and b .

Both of these methods described above are based on two-particle azimuthal correlations. In these methods, anisotropic flow is usually assumed to be the only or dominant source of correlation in azimuth between particles. However, there are other sources of two particle correlations, for instance, the correlations from resonance decay, jets, and quantum effects. These correlations, which are not related to the reaction plane, are called non-flow correlations. In the experiment it is important either to estimate or to minimize these non-flow contributions. This can be done by using appropriate cuts in phase space or using multi-particle correlations.

3.2 Multiparticle correlation

As mentioned above, the methods of flow analysis are sensitive to the non-flow effects. To remedy the limitations new methods have been developed, which are based on the fact that anisotropic flow is a correlation among all particles in an event whereas non-flow effects originate from a few particle correlations. The cumulant method is proposed

to measure flow by a cumulant expansion of multiparticle azimuthal correlations [50,51]. With the increase of order in cumulant expansion, the non-flow effects will decrease. The limit of the infinite order cumulant results in the Lee-Yang zero method [52–54]. These two methods are described below.

3.2.1 Cumulant method

The principle of the cumulant method is that when cumulants of higher order are considered, the contribution of non-flow effects from lower order correlations will be eliminated [50,51]. In the following we take a four-particle correlations as an example to illustrate how this approach works.

Assuming a perfect detector, the measured two-particle correlations can be expressed as flow and non-flow components,

$$\langle e^{in(\phi_1-\phi_2)} \rangle = \langle e^{in(\phi_1-\Psi_r)} \rangle \langle e^{in(\Psi_r-\phi_2)} \rangle + \delta_n = v_n^2 + \delta_n \quad (3.9)$$

where n is the harmonic. The average is taken for all pairs of particles in a certain rapidity and transverse momentum region (typically corresponding to the acceptance of a detector) and for all events in a event sample. The δ_n denotes the non-flow contributions to two-particle correlation. The measured four-particle correlations can be decomposed as follows:

$$\langle e^{in(\phi_1+\phi_2-\phi_3-\phi_4)} \rangle = v_n^4 + 2 \cdot 2 \cdot v_n^2 \delta_n + 2\delta_n^2 \quad (3.10)$$

In this expression, two factors of “2” in front of the term $v_n^2 \delta_n$ correspond to the two ways of pairing (1,3)(2,4) and (1,4)(2,3) and account for the possibility to have non-flow effects in the first pair and flow in the second pair or vice versa. The factor “2” in front of δ_n^2 is from two ways of pairing. The pure four-particle non-flow correlation is omitted in the expression.

From this it follows that the flow contribution can be obtained by subtracting the two-particle correlation from the four-particle correlation:

$$\langle \langle e^{in(\phi_1+\phi_2-\phi_3-\phi_4)} \rangle \rangle = \langle e^{in(\phi_1+\phi_2-\phi_3-\phi_4)} \rangle - 2\langle e^{in(\phi_1-\phi_3)} \rangle^2 = -v_n^4, \quad (3.11)$$

where the notation $\langle \langle \dots \rangle \rangle$ is used for the cumulant. The cumulant of order two is just $\langle \langle e^{in(\phi_1-\phi_2)} \rangle \rangle = \langle e^{in(\phi_1-\phi_2)} \rangle$.

In practice, the cumulants can be calculated by first constructing the generating function of the multiparticle correlations:

$$G_n(z) = \prod_{j=1}^M \left[1 + \frac{w_j}{M} (z^* e^{in\phi_j} + z e^{-in\phi_j}) \right] \quad (3.12)$$

where z is an arbitrary complex number and z^* is its complex conjugate. M denotes the multiplicity in an event. w_j are weights like transverse momentum or rapidity to minimize the statistical error and maximize the flow signal. When the generating function is averaged over events and then expanded in powers of z , z^* , the coefficients of expansion yield the multiparticle correlations. Using these correlations, one can construct the

generating function of the cumulants,

$$M(\langle G_n(z) \rangle^{1/M} - 1) = \sum_k \frac{|z|^{2k}}{(k!)^2} \langle \langle e^{in(\phi_1 + \dots + \phi_k - \phi_{k+1} - \dots - \phi_{2k})} \rangle \rangle \quad (3.13)$$

To study $2k$ particle correlation ($k \geq 1$), the $(2k)^{th}$ order cumulants denoted by $c_n\{2k\}$ can be derived by solving k equations with k different values $|z|$ in the complex plane. From the measured $c_n\{2k\}$, one obtains an estimate of the integrated flow, which is denoted by $V_n\{2k\}$.

$$V_n\{2\}^2 = c_n\{2\}, \quad V_n\{4\}^4 = -c_n\{4\}, \quad V_n\{6\}^6 = c_n\{6\}/4, \quad \dots \quad (3.14)$$

Given an estimate of the n^{th} order integrated flow V_n , one can obtain an estimate of differential flow v'_p (flow in a restricted phase-space window) in any harmonic $p = mn$, where m is an integer. For instance, the 4^{th} order differential flow v'_4 can be analyzed using the integrated V_1 , V_2 , V_3 and V_4 as reference. The generating function of the cumulants for studying differential flow is given by

$$D_{p/n}(z) = \frac{\langle e^{ip\psi} G_n(z) \rangle}{\langle G_n(z) \rangle}, \quad (3.15)$$

where ψ refers to the azimuth of the particle of interest. In the numerator, the average is performed over all particles of interest. On the other hand, the denominator is averaged over all events. Following the same procedure as in the case of the integrated flow, the cumulant $d_p\{2k + m + 1\}$ involving $2k + m + 1$ particles is computed. After this the differential flow $v'_p\{2k + m + 1\}$ is estimated.

For instance, the differential flow estimated from the lowest order cumulant is shown for two cases ($m = 1$ or $m = 2$):

$$\begin{aligned} v'_{n/n}\{2\} &= d_{n/n}\{2\}/V_n, & v'_{n/n}\{4\} &= -d_{n/n}\{4\}/V_n^3, \\ v'_{2n/n}\{3\} &= d_{2n/n}\{3\}/V_n^2, & v'_{2n/n}\{5\} &= -d_{2n/n}\{5\}/(2V_n^4) \end{aligned} \quad (3.16)$$

The advantage of the generating functions is that they automatically involve all possible k -particle correlations when building the k -particle cumulants. Moreover, the formalism removes the non-flow correlations arising from detector inefficiencies. However, in practice, the use of higher order cumulants is often limited by statistics.

3.2.2 Lee-Yang zeroes

More recently, a new method that extracts flow directly from the genuine correlation among a large number of particles has been proposed [52–54]. The method is based on an analogy with the Lee-Yang theory of phase transitions [55] and is called Lee-Yang zeroes. It is expected that this method provides the cleanest separation between flow and non-flow effects. In the following, a product generating function and the related calculations are shown as an example.

Consider a generating function of azimuthal correlations,

$$G^\theta(r) = \langle \prod_{j=1}^M [1 + irw_j \cos(n(\phi_j - \theta))] \rangle \quad (3.17)$$

where r is a real positive variable, $0 \leq \theta < \pi/n$ an angle and the w_j is the weight attributed to the j^{th} particle to maximize the signal. The product runs over all particles in an event and the average denoted by the angular brackets is over events. If there is no collective flow the system consists of independent subsystems, and the product can be factorized to a product over the subsystems. Then the zeroes of G^θ are the same as those of the subsystem function and their positions are independent of the system size (multiplicity). On the contrary, when there is collective flow, the generating function can no longer be factorized and the positions of its zeroes approach the origin as the multiplicity increases. Therefore, the behavior of the zeroes reflects the presence or absence of collective flow in the system.

Now that the position of the first zero of G^θ is directly related to the presence and magnitude of anisotropic flow in the system, the first step to implement the Lee-Yang zeroes is to locate the first zero: calculate the modulus $|G^\theta(r)|$ as a function of r for several values of θ , so as to find for each θ the first minimum r_0^θ . This first minimum then yields an estimate of the integrated flow

$$V_n^\theta\{\infty\} = \frac{j_{01}}{r_0^\theta} \quad (3.18)$$

where $j_{01} = 2.40483$ is the first zero of Bessel function J_0 . The integrated flow is then used as a reference to derive the estimates $v_{mn}^\theta\{\infty\}$ of differential flow $v_{mn}(p_t, y)$ by computing a function at r_0^θ . Averaging the various estimates $v_{mn}^\theta\{\infty\}$ over θ results in $v_{mn}\{\infty\}$ with reduced statistical errors. For further details. see the detailed explanation in [53].

Lee-Yang zeroes provide a natural probe of collective behavior and are expected to give results similar to higher order cumulants. Its main limitation is the statistical errors, which can be significantly larger than with the standard method of flow analysis if the flow or the multiplicities are too small.

Chapter 4

Results

In this chapter, we present measurements of elliptic flow v_2 and the higher harmonic v_4 in Au+Au collisions at $\sqrt{s_{NN}} = 200$ GeV and at $\sqrt{s_{NN}} = 62.4$ GeV. The flow coefficients are studied as function of transverse momentum, centrality, pseudorapidity and particle species.

4.1 Datasets

The analysis was done with the data taken from Au+Au collisions at $\sqrt{s_{NN}} = 200$ GeV and $\sqrt{s_{NN}} = 62.4$ GeV during RHIC Run IV. Particles used in this analysis were reconstructed in the main TPC and two FTPCs. Events were selected with a primary vertex position within 30 cm longitudinally of the TPC center and within 1 cm radially from the beam line. There were 13×10^6 events analyzed at $\sqrt{s_{NN}} = 200$ GeV and 6×10^6 events analyzed at $\sqrt{s_{NN}} = 62.4$ GeV.

Table 4.1: Cuts used in the TPC analysis. Vertex refers to the event vertex, fit points are the space points on a track in the TPC. The ratio, pts/max. pts, is defined by the number of space points to the expected maximum number of space points and dca is the distance of closest approach of the track to the event vertex.

cut	value
p_t	$> 0.15 \text{ GeV}/c$
η	-1.3 to 1.3
multiplicity	> 10
vertex z	-30. to 30. cm
vertex x, y	-1.0 to 1.0 cm
fit points	> 15
fit pts / max. pts	> 0.52
dca	$< 1.0 \text{ cm}$

For the tracks used in the analysis reconstructed in the TPC, the cuts are described in Table 4.1, except for the upper p_t cutoff which is 12 GeV/ c . The ratio of the number of space points to the expected maximum number of space points for the tracks was required to be greater than 0.52 to suppress split tracks from being counted twice. A dca cut of 1 cm is used to select primary particles.

For the analysis involving tracks from the FTPCs, which cover the pseudorapidity $2.5 < |\eta| < 4.0$, at least 5 hits are required. For the FTPC tracks the distance of closest approach of the track to the vertex (dca) is also restricted to less than 1 cm.

For the determination of the event plane, particles with pseudorapidity $|\eta| < 1$ and $p_t < 2$ GeV/ c were used.

At low p_t ($p_t < 1.0$ GeV/ c) and in the relativistic-rise ($p_t > 2.5$ GeV/ c), the pions, kaons and (anti)protons were selected based on the difference between the measured dE/dx of each track and its expected value. This difference is expressed in units of the Gaussian standard deviation ($n\sigma_\pi$, $n\sigma_K$, $n\sigma_p$). For $p_t < 1.0$ GeV/ c , the particles within the region $|n\sigma_\pi| < 3.0$, $|n\sigma_K| < 3.0$ and $|n\sigma_p| < 3.0$ are taken as pions, kaons and (anti)protons, respectively. The purity is estimated to be 98% [56]. For $p_t > 2.5$ GeV/ c , pions are selected with $n\sigma_\pi > 0$ (the top half of the distribution). In this case, the purity is also 98% [57]. (Anti)protons are selected with $-3.0 < n\sigma_p < 0$ (the negative half of the distribution) or $-5.0 < n\sigma_\pi < -2.5$. The difference in the proton v_2 for these two cuts is below 3%. (In the case of $-5.0 < n\sigma_\pi < -2.5$, the sample contains 75% protons, 19% kaons and 6% pions [57].)

The systematic uncertainties from detector artifacts are estimated by comparing data taken with a different magnetic field setting: 0.5 T (full-field) and 0.25 T (half-field). Below 0.5 GeV/ c the half-field v_2 values are lower. A possible reason for the difference is that the half-field data have poorer two-track resolution and are more sensitive to track merging. This uncertainty to v_2 for all particles is around ± 0.0035 (absolute).

The systematic uncertainties in anisotropic flow measurements include detector artifacts, non-flow effects and flow fluctuations. From all these uncertainties the non-flow effects and flow fluctuations are the dominant contributions and are studied in detail in this thesis.

4.2 Elliptic flow

4.2.1 Transverse momentum dependence

Elliptic flow as function of transverse momentum is sensitive to the evolution and freeze-out conditions of the created system. For charged particles, shown in Fig. 4.1, the elliptic flow increases almost linearly as function of p_t reaching values of about 0.15 at large p_t . At low transverse momenta, the elliptic flow is well described by hydrodynamics as shown by the full line in Fig. 4.1. However, above 1 GeV/ c the observed elliptic flow starts to deviate from ideal hydrodynamics. The position of the onset of the deviation from ideal hydrodynamics and its magnitude are thought to constrain the shear viscosity of the fluid [61].

At sufficiently high transverse momentum in Au+Au collisions, hadron yields are believed to contain a significant fraction originating from the fragmentation of high en-

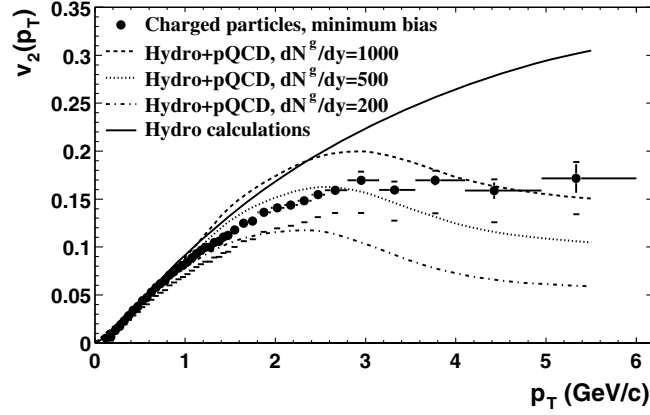


Figure 4.1: Elliptic flow versus transverse momentum for charged particles [58]. The solid line is a hydrodynamic model calculations [59] and the dashed lines show hydro + pQCD calculations for various gluon densities [60].

ergy partons, resulting from initial hard scatterings. Calculations based on perturbative QCD (pQCD) predict that high energy partons traversing nuclear matter lose energy through induced gluon radiation [62]. The energy loss (jet quenching) is expected to depend strongly on the color charge density of the created system and the traversed path length of the propagating parton. In non-central heavy-ion collisions, the geometrical overlap region has an almond shape in the transverse plane, with its short axis in the reaction plane. Depending on the azimuthal emission angle, partons traversing such a system, on average, experience different path lengths and therefore different energy loss. This leads to an azimuthal anisotropy in particle production at high transverse momenta [63–65]. Therefore at high p_t the observed elliptic flow does provide a constraint on the initial gluon density. The dashed lines in Fig. 4.1 show the theory predictions based on energy-loss calculations in a static medium [60].

With the large data sample obtained in Au+Au collisions at $\sqrt{s_{NN}} = 200$ GeV during RHIC Run IV, anisotropic flow coefficients can be measured up to 10 GeV/ c for different collision centralities using higher order cumulants.

Figure 4.2 (a) shows the charged particle v_2 as a function of transverse momentum for mid-central (20–60%) Au+Au collisions at 200 GeV. These v_2 values are obtained with the event plane method (denoted by $v_2\{EP\}$), and with the two- and four-particle cumulant method (denoted by $v_2\{2\}$ and $v_2\{4\}$, respectively). A systematic difference is observed for the values obtained with these three methods, especially between the methods based on two- and four-particle correlations (see Fig. 4.2 (b)). Figure 4.2 (b) clearly shows that the difference increases with transverse momentum. Above 5 GeV/ c the $v_2\{4\}$ is up to 50% lower than the $v_2\{2\}$ and the $v_2\{EP\}$. On the other hand, the difference between $v_2\{2\}$ and $v_2\{EP\}$ is below 5% and is approximately independent of transverse momentum. The difference between $v_2\{2\}$ and $v_2\{4\}$ can be explained by a combination of non-flow effects and fluctuations, where the transverse momentum

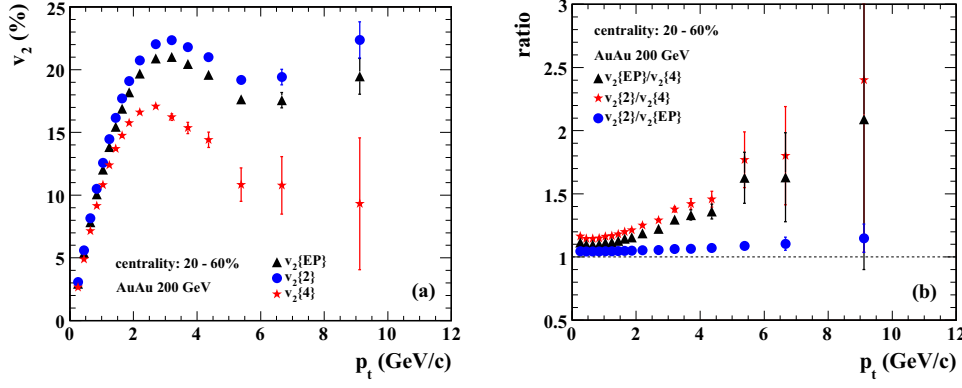


Figure 4.2: (a) Charged particle v_2 versus p_t for 20–60% centrality in Au+Au collisions at 200 GeV from the event plane method (triangles), from the two-particle cumulant method (circles) and from the four-particle cumulant method (stars). (b) The ratios of $v_2\{EP\}/v_2\{4\}$ (triangles), $v_2\{2\}/v_2\{4\}$ (stars) and $v_2\{2\}/v_2\{EP\}$ (circles).

dependence of the difference is likely driven by non-flow. In general, if the fluctuations are small enough, the true v_2 lies between $(v_2\{2\} + v_2\{4\})/2$ and $v_2\{4\}$ [66].

The observed trend, independent of the method used, is that v_2 increases with p_t , reaches its maximum around 3 GeV/c and then decreases again. Elliptic flow obtained using two particle correlations starts to increase again above 6 GeV/c, which is attributed to the non-flow. However, the estimated elliptic flow from the four particle cumulant method is not affected by non-flow and is still sizable above 8 GeV/c. The sizable $v_2\{4\}$ at high p_t is consistent with the scenario of parton energy loss.

The charged particle v_2 as function of p_t for individual centralities in Au+Au collisions at 200 GeV is shown in Fig. 4.3 (a). As before, v_2 is obtained with the event plane method and the cumulant method. $v_2\{4\}$ fails for centrality 0–5% which is attributed to flow fluctuations. Comparing $v_2\{2\}$ as well as $v_2\{EP\}$ to $v_2\{4\}$ for each centrality class, see Fig. 4.3 (b), shows that the mid-central collisions are least effected by non-flow. In the centrality intervals 10–20%, 20–30% and 30–40% the ratio increases with p_t from 1.1 to 1.3 at 5 GeV/c. For more central collisions, 5–10%, the non-flow contribution is larger with the ratio always above 1.2. Peripheral collisions, for instance 60–70%, show the largest non-flow contribution with the ratio reaching 2 at 3 GeV/c, indicating that these v_2 values are dominated by non-flow effects. The centrality dependence of non-flow is as expected because the two particle correlation is a combination of flow and non-flow and the correlation induced by flow, $\propto Mv_2^2$, is small for central and peripheral collisions. Figure 4.3 (b) shows in addition that there is almost no p_t and centrality dependence for the ratio $v_2\{2\}$ to $v_2\{EP\}$.

Figure 4.4 compares the centrality dependence of $v_2\{4\}$. It shows that the centrality dependence changes from low p_t to intermediate p_t . At low p_t , $v_2\{4\}$ continues to increase from central to peripheral collisions, while at intermediate p_t $v_2\{4\}$ peaks for mid-central collisions (30–40%).

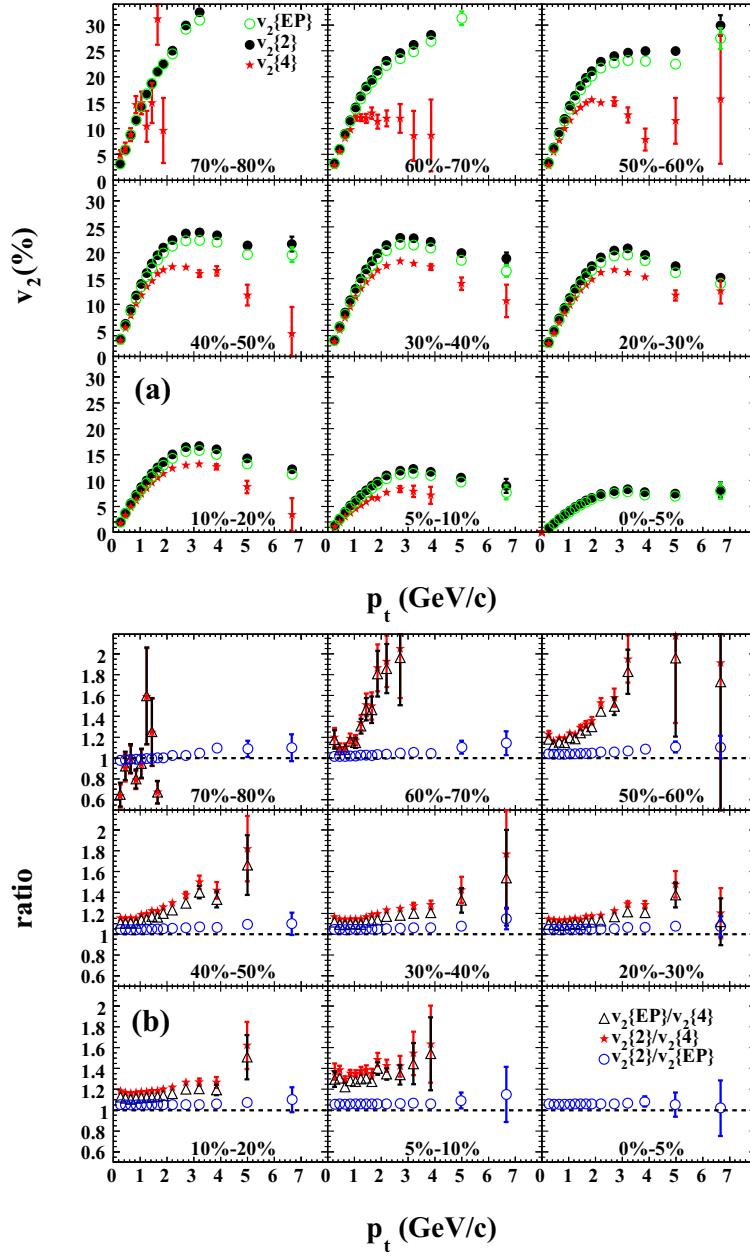


Figure 4.3: (a) Charged particle v_2 versus p_t from the event plane method (open circles), from the two-particle cumulant method (full circles) and from the four-particle cumulant method (stars) for 9 different centrality bins in Au+Au collisions at 200 GeV. (b) The ratios of $v_2\{EP\}/v_2\{4\}$ (triangles), $v_2\{2\}/v_2\{4\}$ (stars) and $v_2\{2\}/v_2\{EP\}$ (circles).

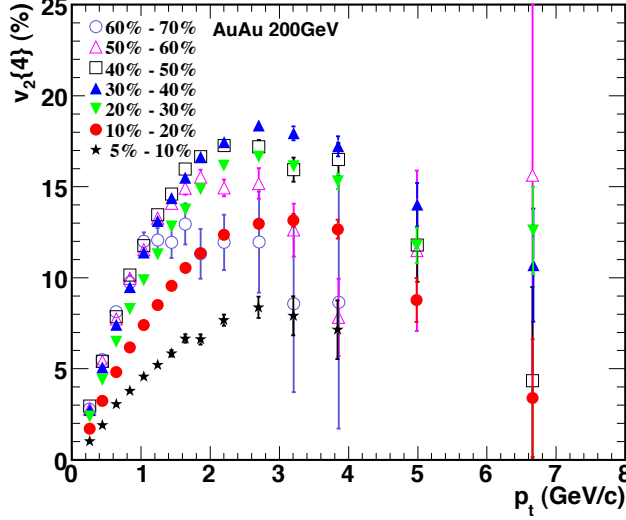


Figure 4.4: Charged particle v_2 versus p_t obtained from the four-particle cumulant method for 7 centrality classes in Au+Au collisions at 200 GeV.

4.2.2 Integrated flow and its centrality dependence

It is argued that the centrality dependence of elliptic flow indicates the degree of equilibration [14] and might provide a indication of the phase transition [13].

In the low density limit (LDL), the mean free path is comparable to or larger than the system size. In this limit, the integrated elliptic flow is proportional to the spatial anisotropy and the number of rescatterings in the transverse plane [67],

$$v_2 \propto \epsilon \frac{1}{S} \frac{dN}{dy} \quad (4.1)$$

where ϵ stands for the spatial eccentricity, dN/dy is the multiplicity density and $S = \pi \sqrt{\langle x^2 \rangle \langle y^2 \rangle}$ is a measure of the initial transverse size of the collision region, where x and y are the spatial coordinates in the plane perpendicular to the collision axis. The brackets $\langle \rangle$ denotes an average weighted with the initial density. The centrality dependence of elliptic flow in LDL reflects the convolution of the eccentricity and the multiplicity which with increasing impact parameter increases and decreases respectively. Therefore the integrated elliptic flow has its maximum at an intermediate impact parameter.

With the increase of particle density, the elliptic flow increases. Eventually, it saturates at the hydrodynamical limit, where the mean free path is much less than the geometrical size of the system and complete thermalization is reached. Elliptic flow in this limit is mainly determined by the eccentricity. Therefore v_2/ϵ is approximately constant though the magnitude does depend on the velocity of sound in the fluid (and thus on the different contributions from the different phases and the phase transition) [47].

The velocity of sound is governed by the equation of state of nuclear matter through $c_s^2 = dp/d\varepsilon$, where p is the pressure and ε is the energy density. A softer equation of state, with smaller c_s , produces smaller elliptic flow. The centrality dependence of elliptic flow in this limit follows the eccentricity, therefore has its maximum at larger impact parameter.

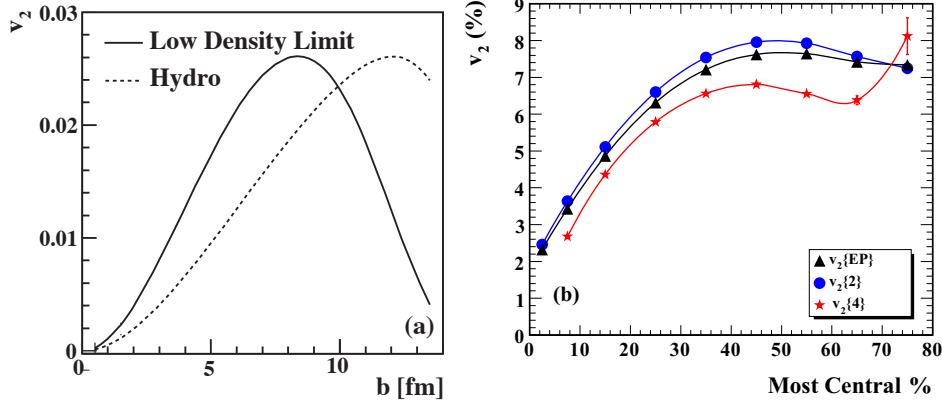


Figure 4.5: (a) v_2 versus centrality from the low density limit (full curve) and hydrodynamics (dashed curve) [14]. (b) Charged particle v_2 integrated over p_t and η versus centrality from the standard event plane method (triangles), from the two-particle cumulant method (circles) and from the four-particle cumulant method (stars) in Au+Au collisions at 200 GeV.

The characteristic dependence of elliptic flow versus centrality for both low density and hydrodynamical limit is shown in Fig. 4.5 (a). Figure 4.5 (b) shows the measured charged particle v_2 integrated over $0.15 < p_t < 2$ GeV/ c and $-1.3 < \eta < 1.3$ as a function of centrality in Au+Au collisions at 200 GeV obtained with the event plane and cumulant methods. As discussed for differential flow, the estimated integrated flow depends on the method due to non-flow or flow fluctuations. The maximum of integrated v_2 is found to be in the 40–60% centrality interval, depending on the method used. This corresponds to the impact parameter range $b = 10 - 11$ fm, which is in between the low density and hydrodynamic limit.

4.2.3 Particle type dependence

Measurements of v_2 for identified particles, as shown in Fig. 4.6, have established that at low p_t the elliptic flow exhibits a characteristic mass ordering with v_2 values at fixed p_t decreasing with increasing mass. Above $p_t = 2$ GeV/ c , the data shows a reversed trend where the v_2 of heavier baryons is larger than that of the lighter mesons [68]. While v_2 for different particle species at low p_t is well described by hydrodynamic calculations as shown by curves in Fig. 4.6, they start to deviate significantly from hydrodynamics at higher p_t .

In hydrodynamics, the collective radial motion boosts particles to higher average

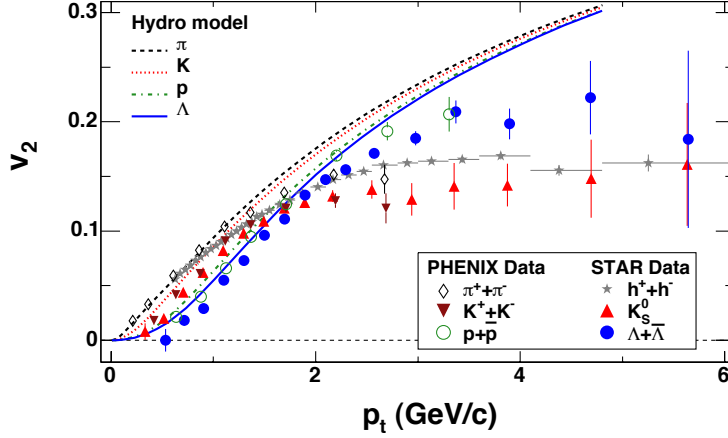


Figure 4.6: v_2 versus p_t for various particle species. The lines are hydrodynamic calculations [68].

momenta, heavier particles gain more momentum than lighter ones. This leads to a flattening of the spectra at low transverse momenta. This flattening reduces v_2 at low p_t , and therefore the heavier the particle the more the rise of $v_2(p_t)$ is shifted towards larger p_t [59].

Ideal hydrodynamics assumes complete local thermalization at the formation time of the system, followed by an evolution governed by an Equation of State (EoS). The details of the dependence of elliptic flow on particle mass and transverse momentum are sensitive to the EoS. Figure 4.7 shows the hydrodynamical model predictions of $v_2(p_t)$ for pions and (anti-)protons for two equations of state: the full curves are for an EoS incorporating the effect of a phase transition from a QGP to a hadron gas, the dashed curves are for a hadronic EoS without phase transition. It is clear that the hydro calculations using the EoS which incorporates the phase transition provides a better description of the measurements. The effect of a phase transition is less pronounced for the pions compared to the protons. This can be understood because the lighter particles are more affected by the temperature thus less sensitive to the collective velocity, and it is the collective velocity which is sensitive to the EoS.

Models of hadron formation by coalescence or recombination of constituent quarks predict that at intermediate p_t ($2 < p_t < 5$ GeV/c), hadron v_2 (v_2^h) is related to the v_2 of quarks (v_2^q) in the quark-gluon phase by the relationship: $v_2^h(p_t) \approx n_q v_2^q(p_t/n_q)$ [70–74]. The elliptic flow therefore approximately scales with the number of constituent quarks (n_q) with v_2/n_q vs. p_t/n_q for all hadrons falling on a universal curve. This scaling has been considered indicative of the partonic origin of flow [70, 71]. Figure 4.8 shows the n_q scaled elliptic flow versus the n_q scaled transverse momentum for various mesons and baryons. The data except pions fall on a universal curve.

The studies presented so far with the STAR TPC are for pions, kaons and (anti)protons limited to low transverse momentum ($p_t < 1.0$ GeV/c). The particle identification can

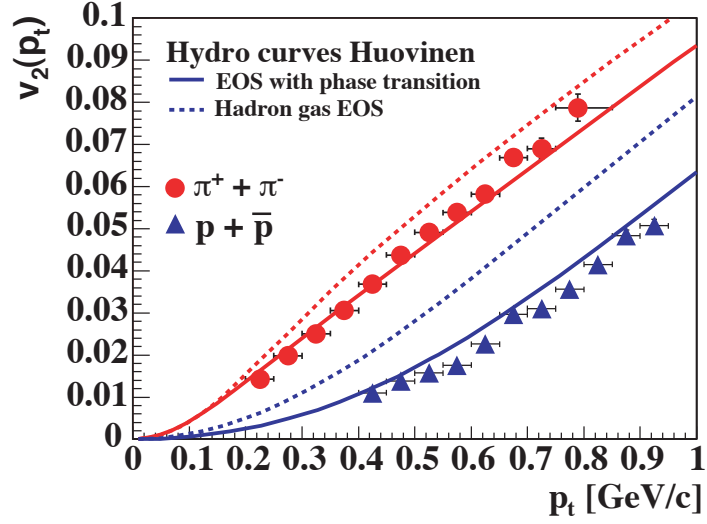


Figure 4.7: v_2 for pions and protons+antiprotons versus p_t [68]. The lines are hydro model calculations. The full line is a calculation with an equation of state incorporating a phase transition, the dashed line is without phase transition.

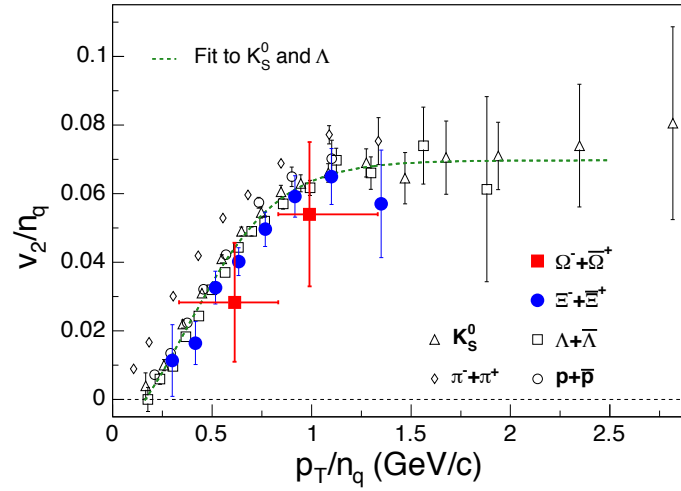


Figure 4.8: Number of constituent quark (n_q) scaled v_2 as function of scaled p_t for various particle species. Pions and (anti)proton results are from PHENIX. The line is the scaled result of the fit to K_s^0 and Λ [69].

be extended to higher transverse momentum ($p_t > 2.5$ GeV/ c) using the relativistic rise of the specific ionization energy loss in the TPC, which allows for measuring v_2 of pions and protons at intermediate to high p_t .

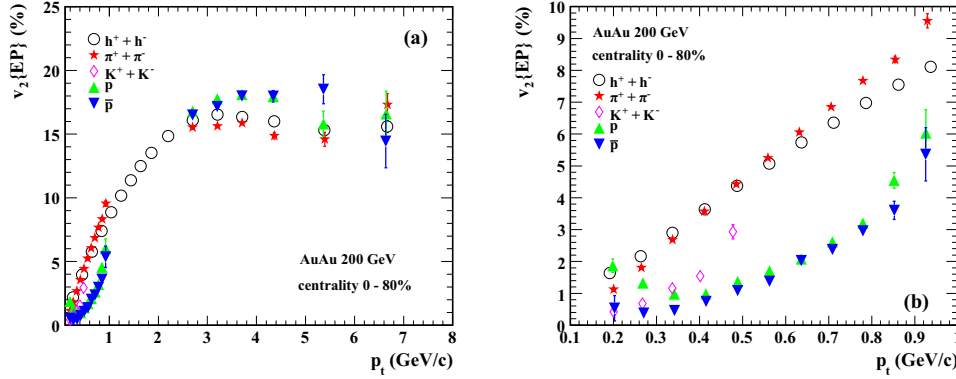


Figure 4.9: (a) $v_2\{EP\}$ versus p_t for charged pions, kaons and (anti)protons in the 0–80% centrality range in Au+Au collisions at 200 GeV. v_2 values for inclusive charged hadrons are displayed as well. (b) $v_2\{EP\}(p_t)$ at $p_t < 1.0$ GeV/ c .

Figure 4.9 (a) shows $v_2(p_t)$ obtained with the event plane method for pions, kaons, protons and antiprotons in minimum-bias data at 200 GeV Au+Au collisions. The v_2 for charged particles is shown for reference. For $p_t < 1.0$ GeV/ c , shown in detail in Fig. 4.9 (b), the familiar mass hierarchy is observed. At $p_t < 0.3$ GeV/ c the larger v_2 for protons compared to antiprotons is attributed to the contamination coming from protons produced in secondary interactions of particles with the detector material. At $p_t > 2.5$ GeV/ c , v_2 reaches a maximum, the mass ordering is broken, and v_2 for (anti)protons is larger than for pions. This trend for pions and protons follows the behavior observed for the strange particles K_s^0 and $\Lambda + \bar{\Lambda}$.

The centrality dependence of charged pions, kaons, (anti)protons as well as charged hadron $v_2(p_t)$ for 200 Au+Au collisions is shown in Fig. 4.10 (a). The characteristic low p_t mass ordering and characteristic intermediate p_t behavior are observed for each of the centrality intervals.

However, as shown for the charged hadrons, when v_2 is measured using the event plane method, non-flow effects can bias the experimental estimation of the reaction plane and change the apparent v_2 values. The non-flow effects have the largest relative contribution for the most central and for the most peripheral collisions. These non-flow effects can be significantly reduced by using four particle cumulant analysis.

Figure 4.11 (a) shows $v_2(p_t)$ for $p_t < 1.0$ GeV/ c for charged pions, kaons and (anti)protons in 20–60% centrality bin in Au+Au collisions at 200 GeV obtained with the event plane method, and the two- and four-particle cumulants. Figure 4.11 (b) shows the corresponding ratio of the standard event plane $v_2\{EP\}$ and two-particle cumulant $v_2\{2\}$ to the four-particle cumulant $v_2\{4\}$. In the p_t range below 1 GeV/ c , $v_2\{EP\}/v_2\{4\}$ is around unity within statistical errors for protons and kaons. For pions

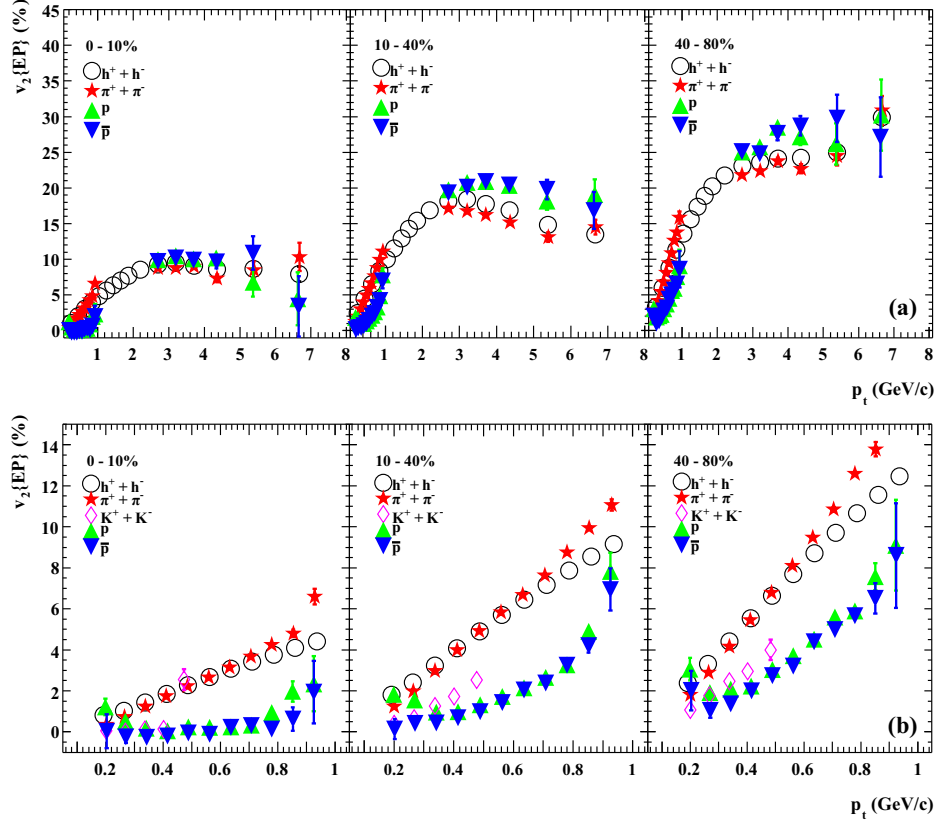


Figure 4.10: (a) $v_2\{EP\}$ versus p_t for inclusive charged hadrons, charged pions, kaons and (anti)protons in 0–10%, 10–40%, and 40–80% of the Au+Au interaction cross section at 200 GeV. v_2 is obtained with the standard event plane method. (b) $v_2\{EP\}(p_t)$ at $p_t < 1.0$ GeV/c.

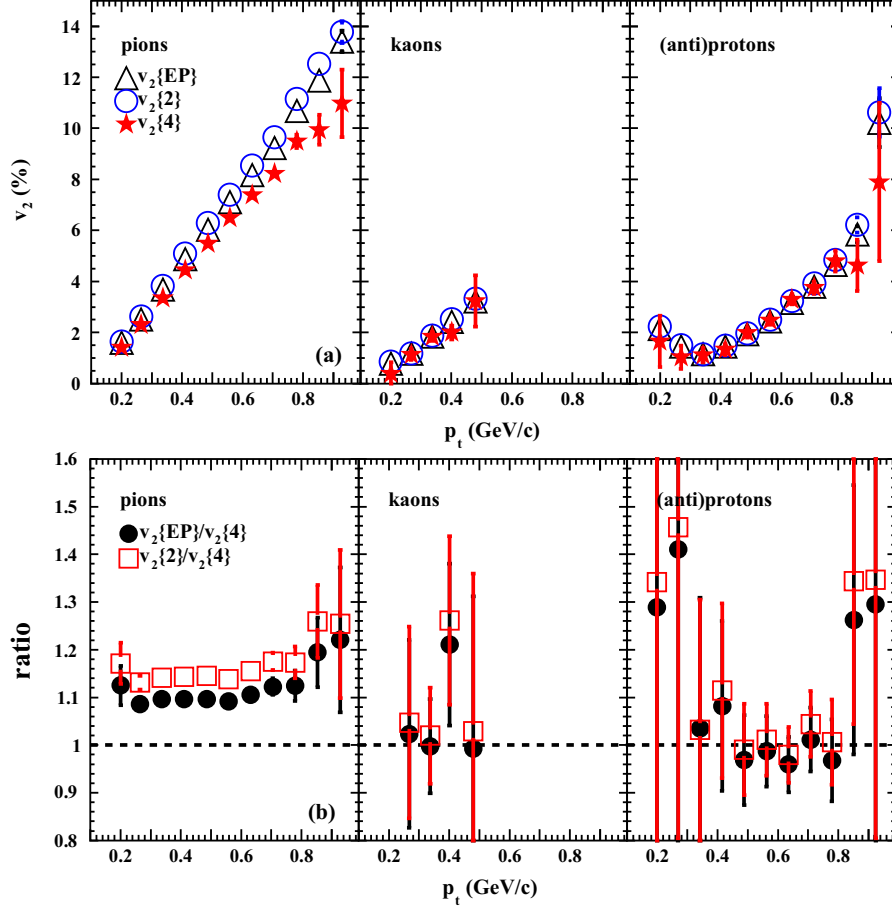


Figure 4.11: (a) $v_2\{p_t\}$ for $p_t < 1.0$ GeV/c for charged pions, kaons and (anti)protons in the 20–60% centrality bin in Au+Au collisions at 200 GeV. The v_2 is obtained with standard event plane method (triangles), two-particle cumulants (circles) and four-particle cumulants (stars). (b) The ratio of $v_2\{EP\}$ and $v_2\{2\}$ to $v_2\{4\}$.

in this range, however, the ratio is around 1.1 which indicates that non-flow correlations can be as large as 10%.

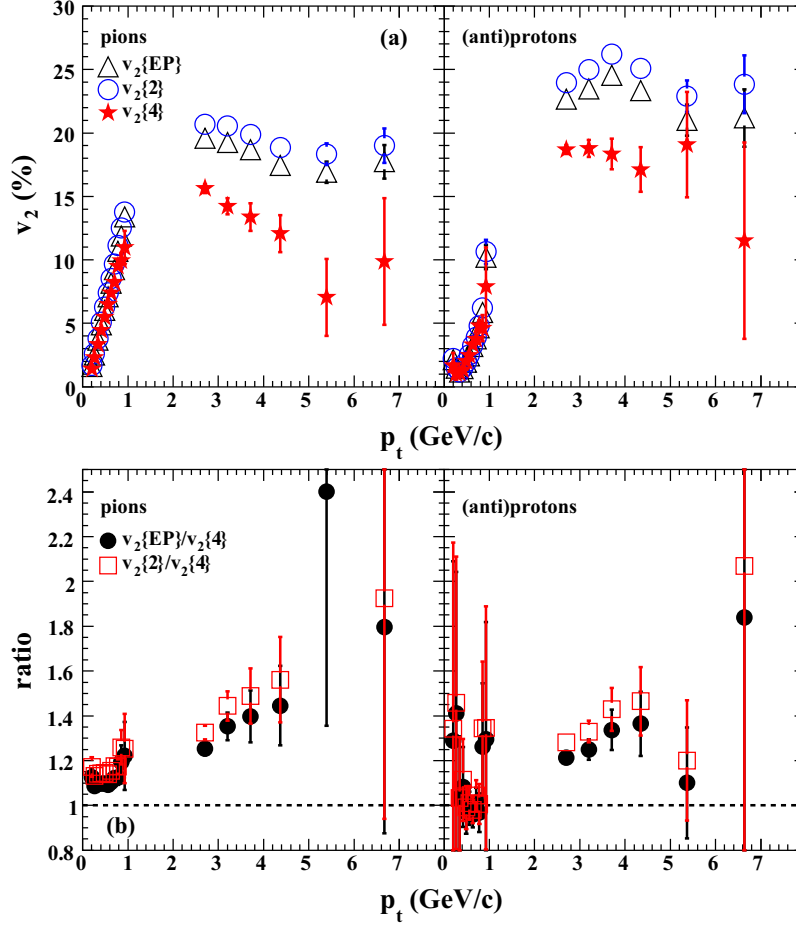


Figure 4.12: (a) $v_2\{p_t\}$ for charged pions and (anti)protons in the 20–60% centrality in Au+Au collisions at 200 GeV. The v_2 is obtained with standard event plane method (triangles), two-particle cumulants (circles) and four-particle cumulants (stars). (b) The ratio of $v_2\{EP\}$ and $v_2\{2\}$ to $v_2\{4\}$.

Figure 4.12 (a) shows charged pions and (anti)protons $v_2(p_t)$ extended to high p_t . A large difference between $v_2\{EP\}$ and $v_2\{4\}$ for both pions and (anti)protons is observed. At intermediate to high p_t , $v_2\{EP\}/v_2\{4\}$ is greater than unity and increases with p_t for (anti)protons as well as pions, see Fig. 4.12 (b). Nevertheless $v_2\{4\}$, shown in Fig. 4.13, confirms the characteristic intermediate p_t dependence as was already observed previously using the event plane method.

In order to compare to other identified particles already available in STAR, v_2 for

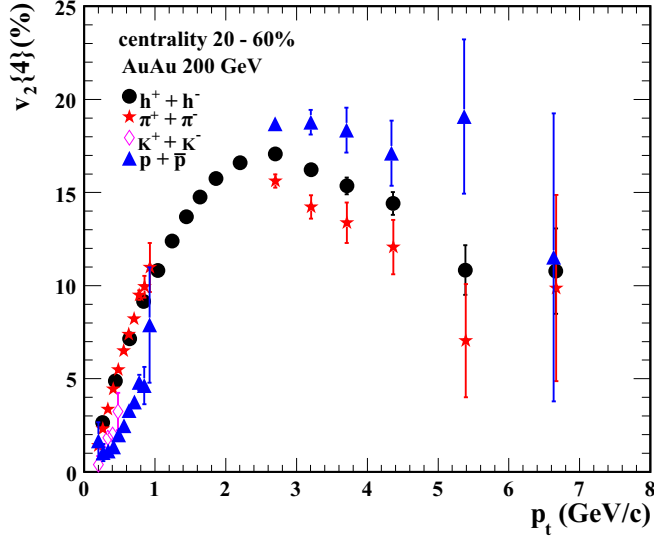


Figure 4.13: $v_2\{4\}$ versus p_t for inclusive charged hadrons, charged pions, kaons and (anti)protons in the 20–60% centrality interval in Au+Au collisions at 200 GeV.

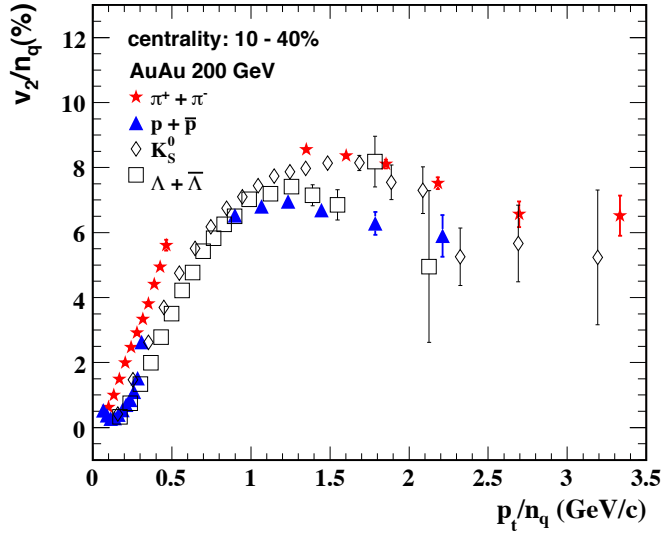


Figure 4.14: The scaled flow coefficients v_2/n_q versus p_t/n_q in the 10-40% centrality range in 200 GeV Au+Au collisions. $v_2\{EP\}$ is used for all particle species.

pions and protons is determined in the 10–40% centrality range using the reaction plane method. Figure 4.14 shows $v_2\{EP\}$ scaled by the number of constituent quarks n_q for pions, (anti)protons, K_s^0 and Λ as function of p_t scaled by n_q in 200 GeV Au+Au collisions. The scaled v_2 of these baryons and mesons, except for pions at low p_t , indeed approximately fall on a universal curve.

4.2.4 Energy dependence

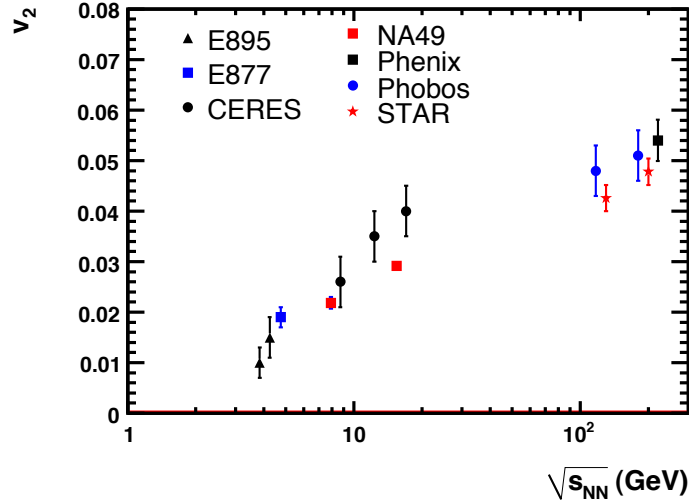


Figure 4.15: Elliptic flow as function of $\sqrt{s_{NN}}$ from AGS to the highest RHIC energies [46, 75–78].

The measured elliptic flow as function of beam energy for fixed centrality is shown in Fig. 4.15 [46, 75–78]. It is seen that the magnitude of v_2 increases smoothly with energy. Calculations from hadronic cascade models for the same centrality do not generate $v_2 \geq 0.02$ even at the highest beam energy. It follows that above AGS energies the measured elliptic flow is underpredicted by hadronic cascade models like RQMD [63]. On the other hand the calculations based on parton cascade allow for larger values of elliptic flow, even as large as observed at the highest RHIC energy [28, 79, 80]. However, these parton cascade models need, in order to describe the data, parton-parton cross sections which are much larger than the values calculated in pQCD.

Theoretical predictions from hydrodynamics for v_2 as function of the center-of-mass energy $\sqrt{s_{NN}}$ are shown in Fig. 4.16. Hydrodynamics, with an EoS which incorporates the different phases of QCD matter, predicts that the phase transition causes a non-monotonic excitation function for elliptic flow (circles and upper curve) [15, 81]. As the collision energy increases, initially v_2 increases since at low energies the fireball freezes

out before the elliptic flow has reached the hydrodynamical limit. When the energy density increases and the system enters the phase transition, v_2 decreases due to the reduced hydrodynamic pressure gradients, this is the so called softest point of the EoS. At even higher energy densities the v_2 increases again and finally saturates reflecting the QGP pressure gradient.

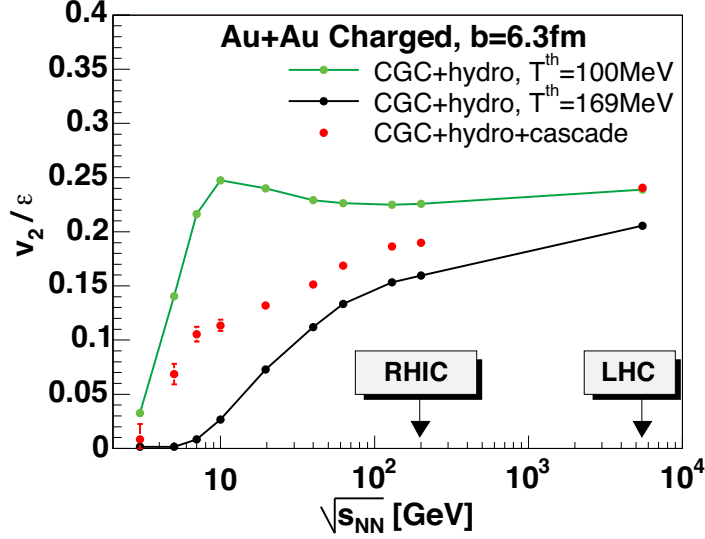


Figure 4.16: Theoretical predictions of v_2 versus collision energy using color glass condensate estimates for the initial conditions [81]. Instead of v_2 , v_2/ϵ is plotted. The calculations shown in this figure correspond to a fixed impact parameter which also implies a fixed eccentricity. Ideal hydrodynamic expansion up to kinetic freeze-out (circles and upper curve) or chemical freeze-out (circles and lower curve) is assumed. The circles without curve are results using a hadronic cascade model to describe the final phase after chemical freeze-out.

After the system freezes out v_2 can be affected by hadronic final state interactions. Therefore a more realistic description of the system evolution is given by combining hydrodynamics, applied at the early partonic and mixed-phase, with a hadronic transport model such as (U)RQMD for the later hadronic stage. It has been shown that the combination of hydrodynamics with hadronic cascade leads to a monotonic energy dependence of elliptic flow [81, 82], see the full circles without curve in Fig. 4.16. The contribution from the QGP phase (hydrodynamics up to 169 MeV) is shown by circles and lower curve. It is seen that at lower beam energies the contribution from the hadronic stage to v_2 is larger.

To compare simultaneously the energy and the centrality dependence as function of beam energy in one figure, v_2 scaled by the initial eccentricity (v_2/ϵ) versus $S^{-1}dN/dy$ is shown in Fig. 4.17. By dividing v_2 with ϵ , a correction for the initial geometry of the different centralities is applied. The multiplicity density, $S^{-1}dN/dy$, increases with centrality and increasing beam energy. The values of v_2/ϵ fall approximately on a single

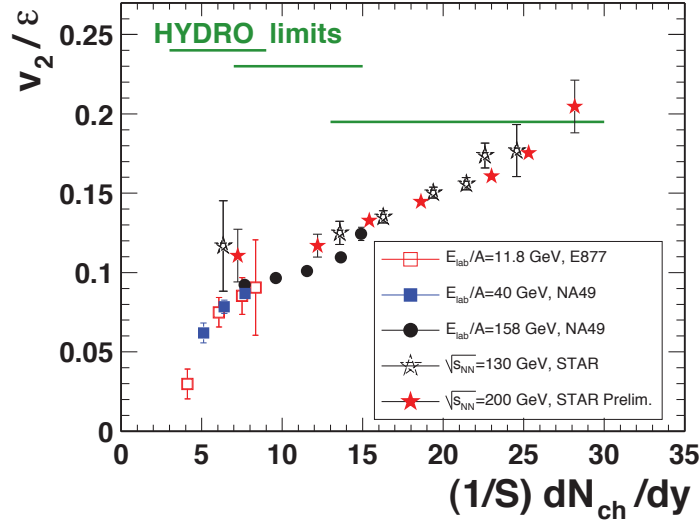


Figure 4.17: v_2 scaled by the initial eccentricity as function of multiplicity density [46].

curve, independent of beam energy or impact parameter. This shows that the elliptic flow increases approximately linearly from AGS to the top RHIC energy when corrected for the initial geometry. At the full RHIC energy for near central collisions, the value of v_2/ϵ approaches the ideal hydrodynamic calculations indicated in the figure by the horizontal lines (“hydro limits”). If the system would be locally thermalized, v_2/ϵ should be approximately centrality independent and weakly depending on beam energy through the equation of state. The disagreement between the data and the hydrodynamic calculations at lower energies and peripheral collisions is generally interpreted as a sign of incomplete thermalization.

To investigate in more detail the energy dependence of elliptic flow, elliptic flow measured by STAR at 200 GeV and 62.4 GeV is compared differentially as function of transverse momentum and particle type.

Figure 4.18 (a) shows $v_2(p_t)$ for charged particles in different centrality classes in Au+Au collisions at $\sqrt{s_{NN}} = 62.4$ GeV. The results are obtained using the event plane method, and the two- and four-particle cumulant. For the most central (0–5%) and the most peripheral collisions (70–80%), $v_2\{4\}$ can not be extracted due to the flow fluctuations. Comparing $v_2\{EP\}$ ($v_2\{2\}$) to $v_2\{4\}$ shows, similar to 200 GeV, that non-flow effects are more important at larger p_t and for central and peripheral collisions, see Fig. 4.18 (b). $v_2(p_t)$ at 62.4 GeV increases with transverse momentum and reaches its maximum around $p_t = 3$ GeV/c after which it decreases again.

Figure 4.19 (a) shows charged particle $v_2\{4\}(p_t)$ for both 62.4 GeV and 200 GeV as function of centrality. At these two energies, the transverse momentum dependence of $v_2\{4\}$ is very similar. However the ratio, shown in Fig. 4.19 (b), for the mid-central collisions shows that $v_2(p_t)$ increases approximately 5% from 62.4 GeV to 200 GeV.

In addition to $v_2(p_t)$ for charged particles, we can compare the particle type depen-

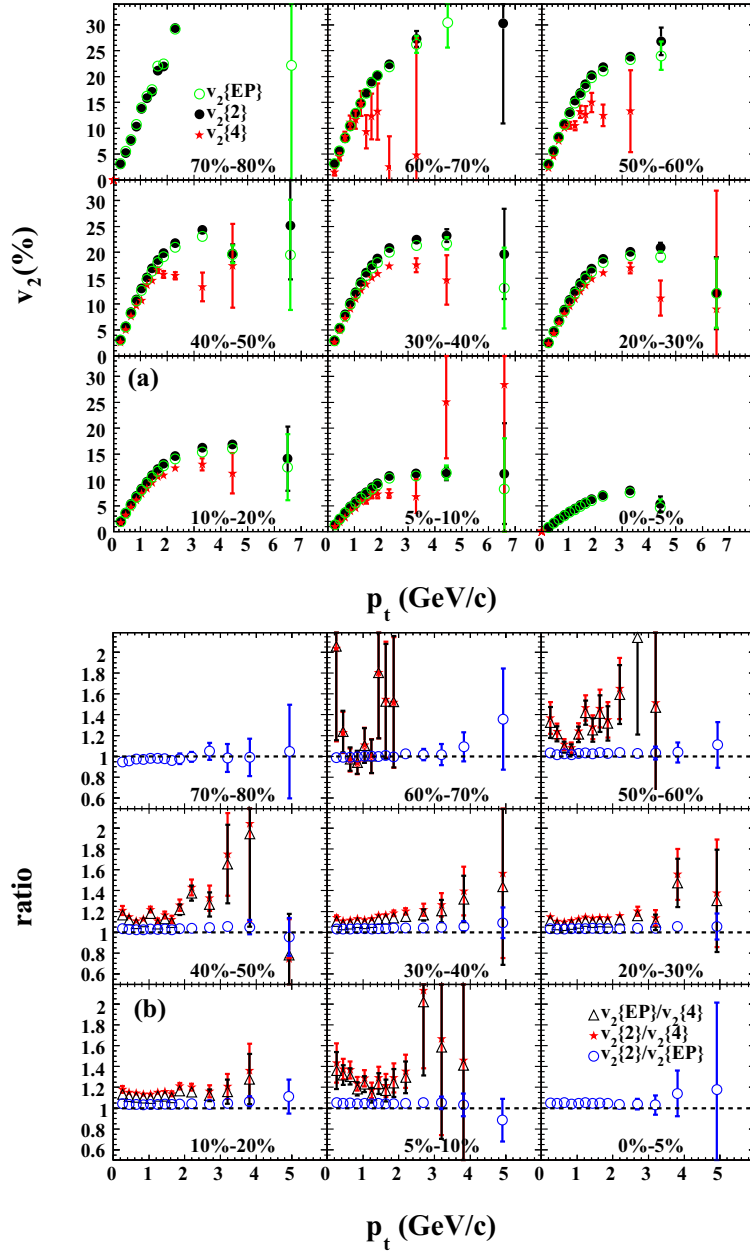


Figure 4.18: (a) Charged particle v_2 versus p_t obtained from the standard event plane method (open circles), from the two-particle cumulant method (full circles) and from the four-particle cumulant method (stars) for different centrality bins in Au+Au collisions at 62.4 GeV. (b) The ratios of $v_2\{EP\}/v_2\{4\}$ (triangles), $v_2\{2\}/v_2\{4\}$ (stars) and $v_2\{2\}/v_2\{EP\}$ (circles).

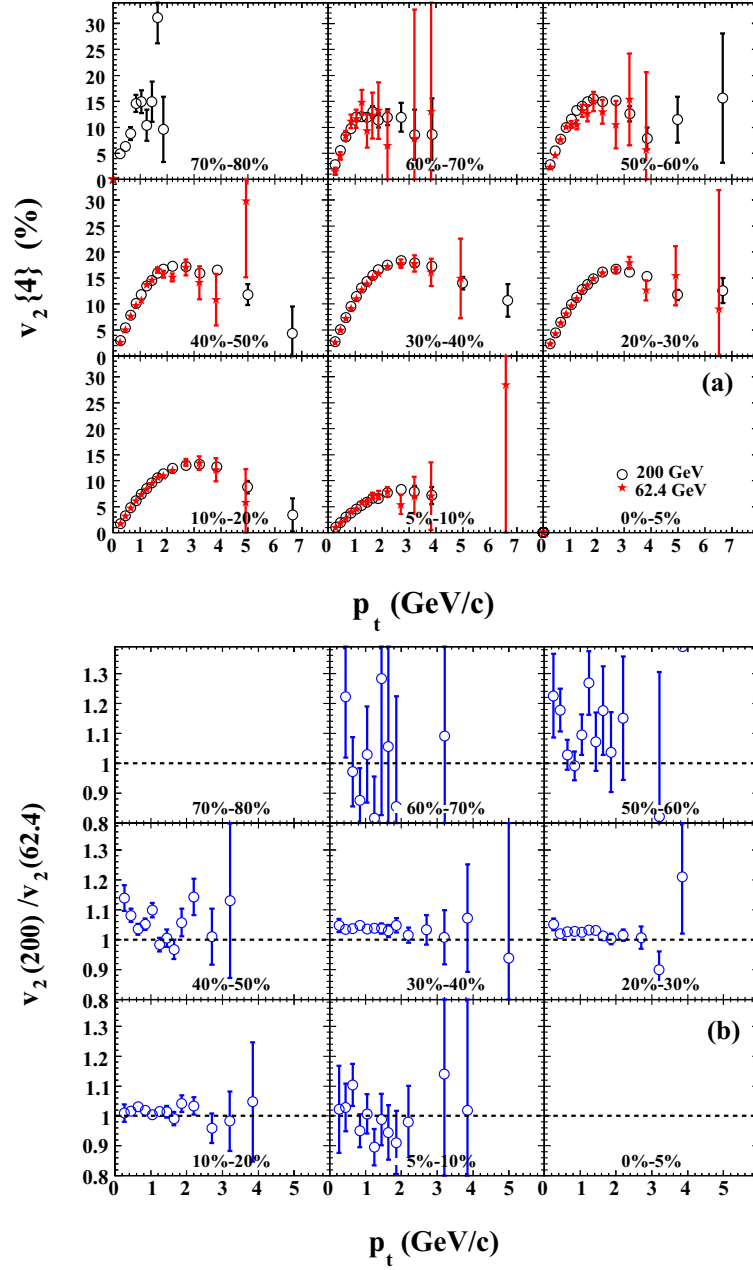


Figure 4.19: (a) Charged particle $v_2\{4\}$ versus p_t for different centrality intervals in Au+Au collisions at 200 (circles) and 62.4 GeV (stars). (b) The ratio of $v_2\{4\}(p_t)$ at 200 GeV to that at 62.4 GeV.

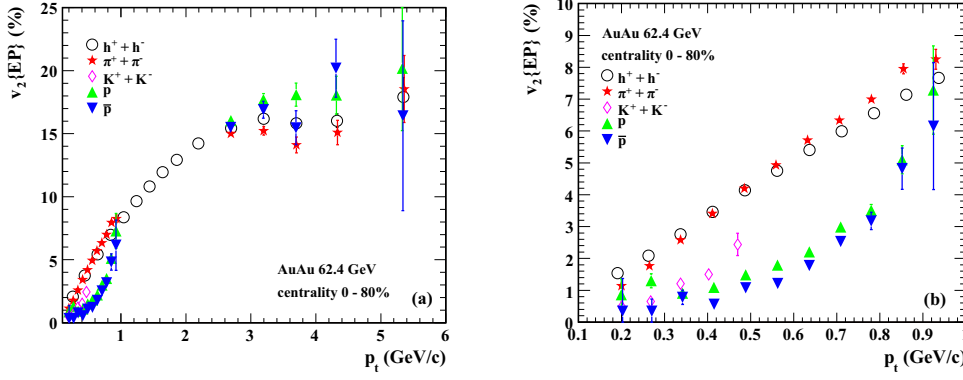


Figure 4.20: (a) v_2 versus p_t obtained with standard event plane method for charged pions, kaons, protons and antiprotons for minibias Au+Au collisions at 62.4 GeV. v_2 for inclusive charged hadrons is shown for reference. (b) $v_2(p_t)$ at $p_t < 1.0$ GeV/c.

dence at 62.4 GeV and 200 GeV. Figure 4.20 (a) shows $v_2(p_t)$ for charged pions, kaons, protons and antiprotons for minibias (0–80%) Au+Au collisions. For $p_t < 1.0$ GeV/c (shown in more detail in Fig. 4.20 (b)), the characteristic mass ordering is observed. For $p_t > 2.5$ GeV/c, (anti)proton v_2 is larger than pion v_2 as was seen at 200 GeV. The characteristic low and intermediate p_t behavior observed in minibias collisions at 62.4 GeV and at 200 GeV also holds for the different centralities, see Fig. 4.21 (a) and (b).

To estimate the non-flow effects at 62.4 GeV for pions and protons, elliptic flow obtained from the event plane method, the two- and four-particle cumulants is compared in the 20–60% centrality bin, see Fig. 4.22 (a). The corresponding ratio of $v_2\{EP\}$ and $v_2\{2\}$ to $v_2\{4\}$, Fig. 4.22 (b), shows for pions a 10% difference while protons are inconclusive. Figure 4.23 (a) shows charged pions and (anti)protons $v_2(p_t)$ obtained with the different analysis methods extended to higher p_t . The ratio of $v_2\{EP\}/v_2\{4\}$ and $v_2\{2\}/v_2\{4\}$ in Fig. 4.23 (b) clearly shows increasing non-flow contributions to both pions and (anti)protons as function of transverse momentum. Nevertheless, like at 200 GeV, the pion and (anti)proton $v_2\{4\}$ at intermediate p_t is still significant.

Figure 4.24 compares v_2 as function of p_t obtained with four-particle cumulant method for pions and (anti)protons both at 200 and 62.4 GeV. A similar p_t dependence for v_2 is observed at these two energies for both pions and (anti)protons at intermediate p_t . The results restricted to the low p_t region are shown in Fig. 4.25 (a). Figure 4.25 (b) shows that at low p_t v_2 for pions at 62.4 GeV tends to be about 5% smaller than at 200 GeV. The (anti)proton data at 62.4 and 200 GeV are consistent within errors.

Figure 4.26 (top panel) shows pion and proton v_2 from $\sqrt{s_{NN}} = 62.4$ Au+Au and 17.3 GeV Pb + Pb collisions from NA49 measured at the CERN SPS [46,57]. The bottom panels show pion, K_s^0 , proton and $\Lambda + \bar{\Lambda}$ data from both 17.3 and 200 GeV scaled by 62.4 GeV data. The 200 to 62.4 GeV ratios are obtained using v_2 data measured within the 0–80% centrality interval. The TOF v_2 measurements obtained at 62.4 GeV allow to show the 17.3 GeV to 62.4 GeV v_2 ratio to higher p_t . To approximately match the

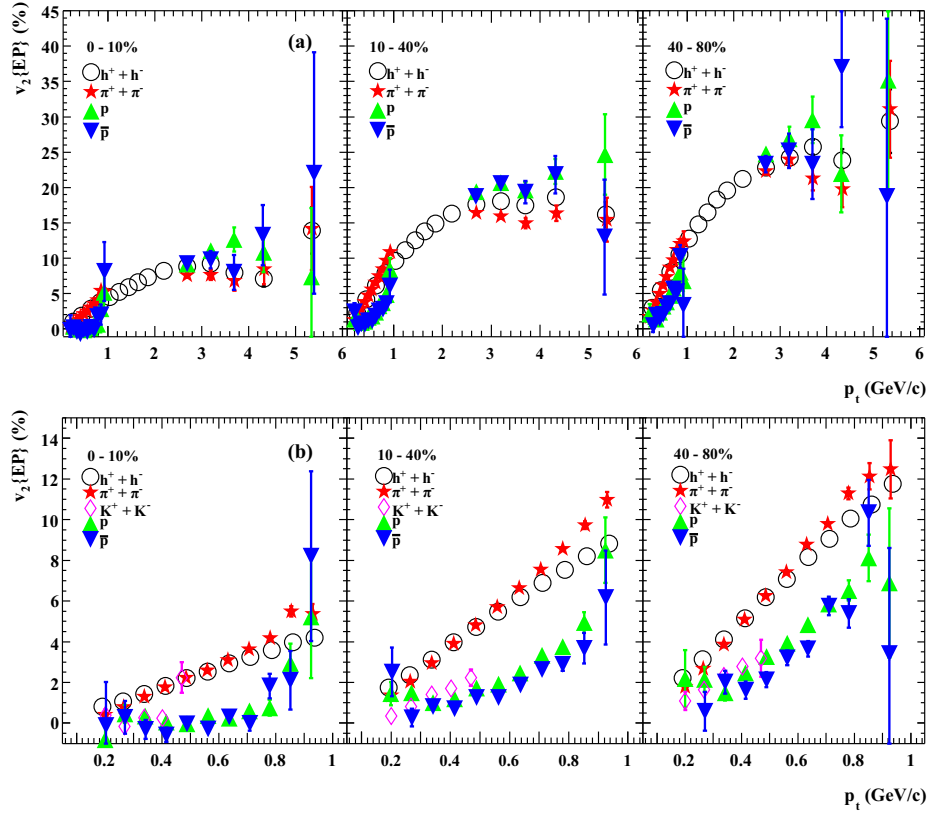


Figure 4.21: (a) v_2 versus p_t for inclusive charged hadrons, pions, kaons, protons and antiprotons in 0–10%, 10–40% and 40–80% of Au+Au cross section at 62.4 GeV. (b) $v_2(p_t)$ at $p_t < 1.0$ GeV/c.

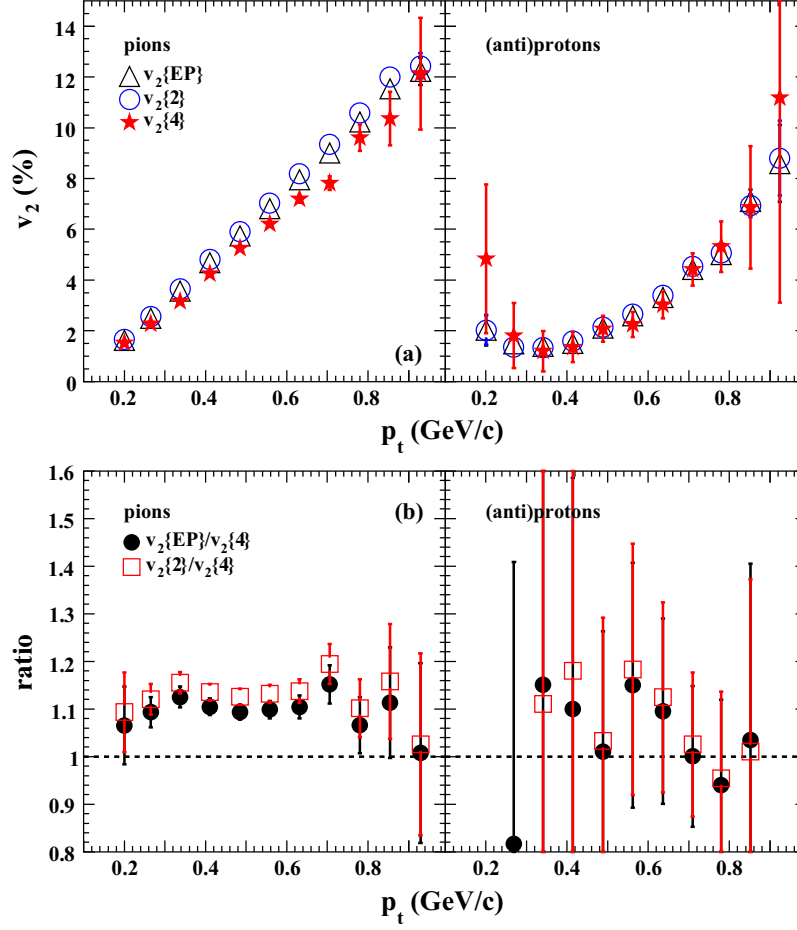


Figure 4.22: (a) v_2 versus p_t for pions and (anti)protons in the 20–60% centrality range in Au+Au collisions at 62.4 GeV. (b) The ratio of $v_2\{EP\}$ and $v_2\{2\}$ to $v_2\{4\}$ versus p_t for pions and (anti)protons.

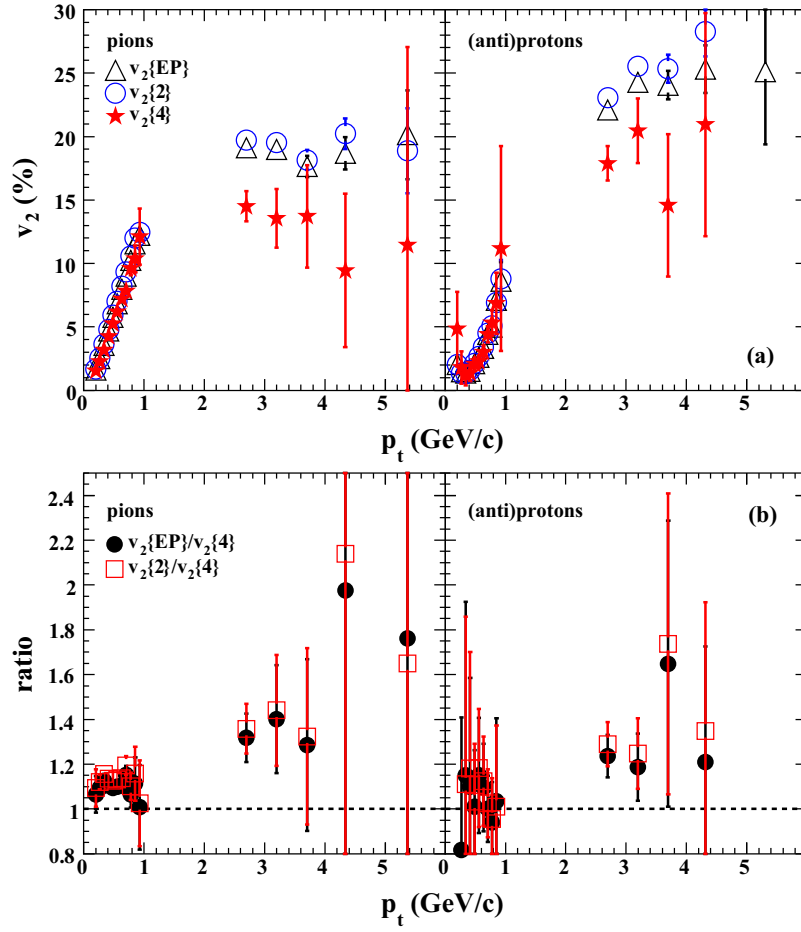


Figure 4.23: (a) v_2 versus p_t for pions and (anti)protons in the 20–60% centrality range in Au+Au collisions at 62.4 GeV. (b) The ratio of $v_2\{EP\}$ and $v_2\{2\}$ to $v_2\{4\}$ versus p_t for pions and (anti)protons.

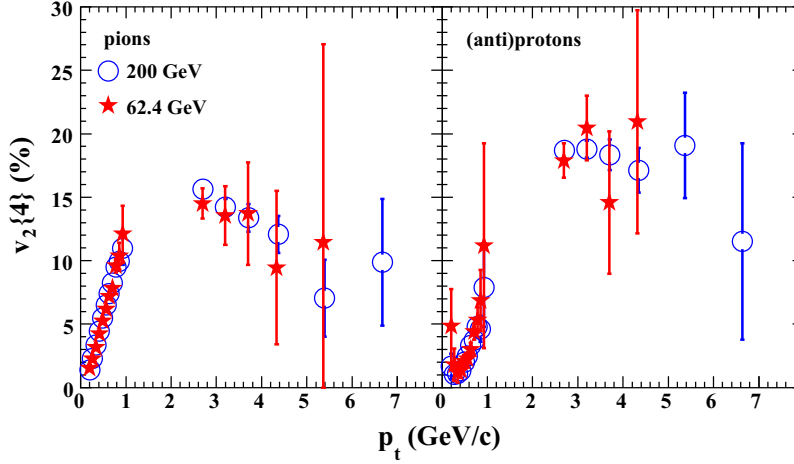


Figure 4.24: $v_2\{4\}$ versus p_t for pions and (anti)protons in 20–60% centrality range in Au+Au collisions at 200 (circles) and 62.4 GeV (stars).

centrality interval used for the 17.3 GeV data, the 17.3 to 62.4 GeV ratios are taken using 0–43.5% and 0–40% centrality intervals respectively. The STAR data at 62.4 GeV and 200 GeV are measured within the pseudo-rapidity interval $|\eta| < 1.0$ and the 17.3 GeV data are from the rapidity interval $0 < y < 0.7$. The standard event plane method is used to compare the measurements.

Possible non-flow errors, estimated from the difference of $v_2\{2\}$ and $v_2\{4\}$, are slightly larger at 200 GeV compared to 62.4 GeV. In the lower panels of Fig. 4.26, the shaded bands around unity show the uncertainty in the energy dependence of the v_2 ratio due to possible changes in the magnitude of non-flow effects at different energies. The portion of the band above unity applies to the ratio of 200 and 62.4 GeV data while the portion below unity only applies to the ratio of the 17.3 and 62.4 GeV data.

The v_2 data for pions and kaons at 62.4 GeV is about 5% smaller than the 200 GeV data (although at $p_t > 1$ GeV/ c the difference is within systematic uncertainties). The anti-proton data at 62.4 and 200 GeV are consistent within errors. For $p_t < 1.5$ GeV/ c the 200 GeV $\Lambda + \bar{\Lambda}$ v_2 is systematically smaller than the 62.4 GeV data, whereas for $p_t > 1.5$ GeV/ c the 200 GeV $\Lambda + \bar{\Lambda}$ v_2 data are consistent with or larger than the 62.4 GeV data. Such a dependence can arise if the system in 200 GeV collisions develops a larger expansion velocity.

Significant differences are seen between the 17.3 GeV and 62.4 GeV data at $p_t > 0.5$ GeV/ c . The v_2 values for pions measured at 62.4 GeV are approximately 10–25% larger than those measured at 17.3 GeV [46]. Although the magnitude of v_2 is different at the lower energy, the systematics of the particle-type dependencies are similar. In particular, pion v_2 and proton v_2 cross (or attain similar values) at $p_t \sim 1.7$ GeV/ c for $\sqrt{s_{NN}} = 17.3, 62.4$ and 200 GeV data. Due to the limited kinematic range covered by the 17.3 GeV data, a quark-number dependence of v_2 at intermediate p_t can neither be confirmed nor excluded.

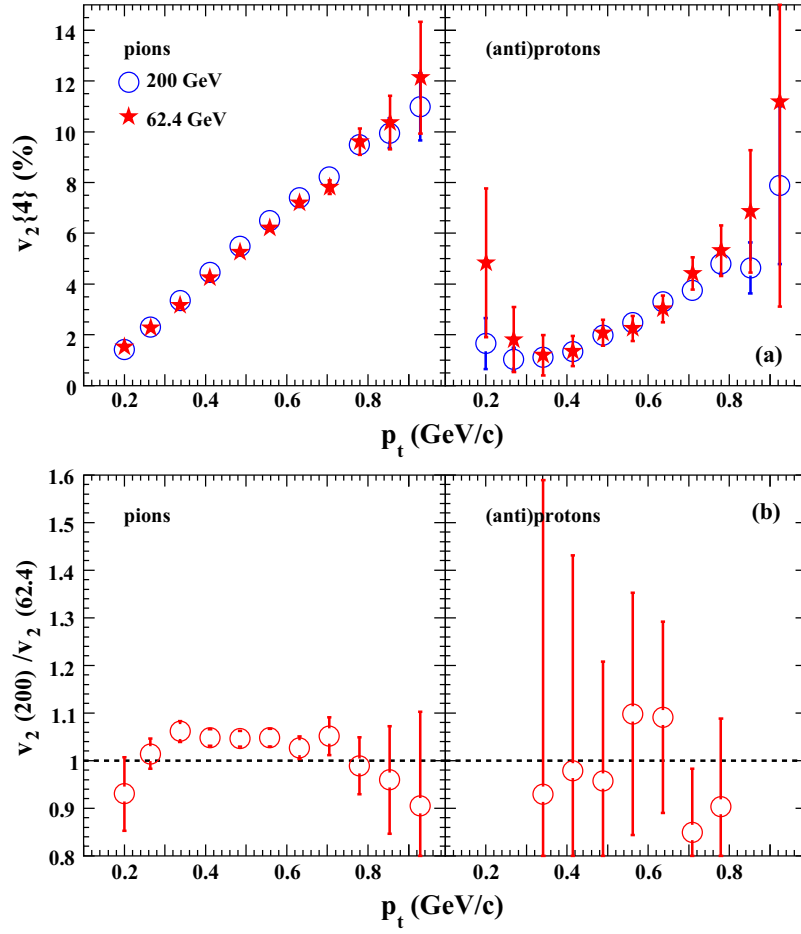


Figure 4.25: (a) $v_2\{4\}$ versus p_t at low p_t for pions and (anti)protons in 20–60% centrality bin in Au+Au collisions at 200 (circles) and 62.4 GeV (stars). (b) The ratio of $v_2\{4\}(p_t)$ at 200 GeV to that at 62.4 GeV for pions and (anti)protons.

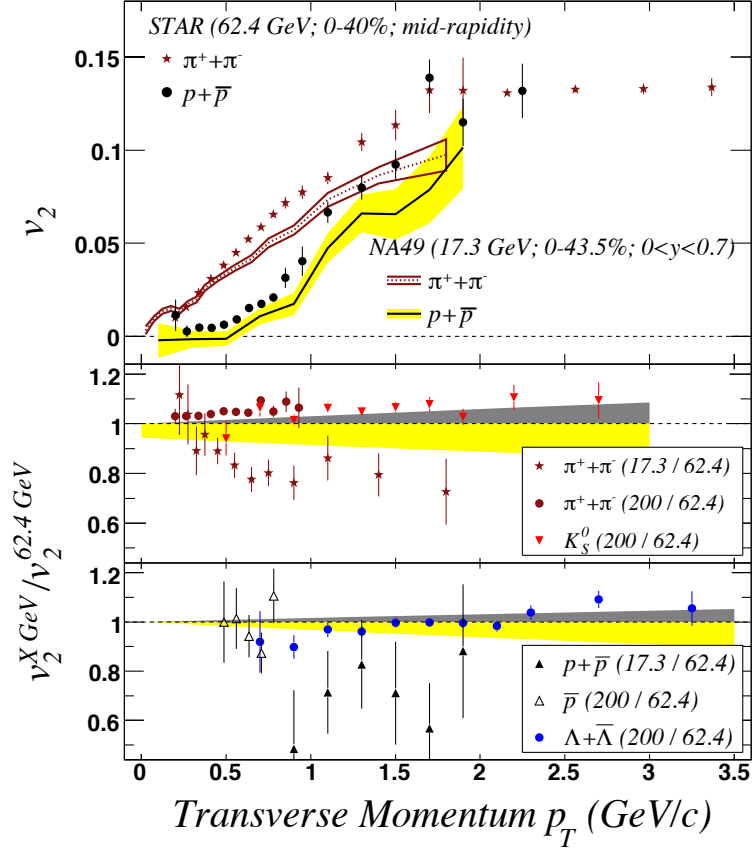


Figure 4.26: (Top panel) v_2 for pions and protons at $\sqrt{s_{NN}} = 62.4$ and 17.3 GeV. The 62.4 GeV data from TOF and dE/dx measurements combined. (Middle and bottom panels) Ratios of v_2 for $\pi^+ + \pi^-$, K_s^0 , $p + \bar{p}$ and $\Lambda + \bar{\Lambda}$ and at different center-of-mass energies scaled by the values at 62.4 GeV. The gray and yellow bands represent systematic uncertainties in the v_2 ratios arising from non-flow effects. The bands above unity are the uncertainties for the 200 GeV/62.4 GeV data and the bands below unity are for the 17.3 GeV/62.4 GeV data [57].

The larger increase in the slope of $v_2(p_t)$ from 17.3 to 62.4 GeV compared to the increase from 62.4 GeV to 200 GeV has been taken as a possible indication for reaching the limiting hydrodynamic behavior at 62.4 GeV [83].

4.2.5 Rapidity dependence

Measurements obtained in Au+Au collisions at $\sqrt{s_{NN}} = 130$ GeV by the Phobos collaboration have shown that integrated elliptic flow decreases rapidly as function of rapidity with a shape similar to the charged particle pseudorapidity distribution [84]. This has been confirmed by STAR based on Run II data [68].

It has been shown that particle production in the fragmentation region exhibits longitudinal scaling when plotted as a function of $\eta - y_{beam}$ [85]. This observation is known as limiting fragmentation. It is also known that the integrated elliptic flow for fixed centrality at mid-rapidity is proportional to the particle yield dN/dy as discussed in Section 4.2.2. If this scaling with dN/dy holds at all rapidities, then v_2 is also expected to show a longitudinal scaling behavior [86].

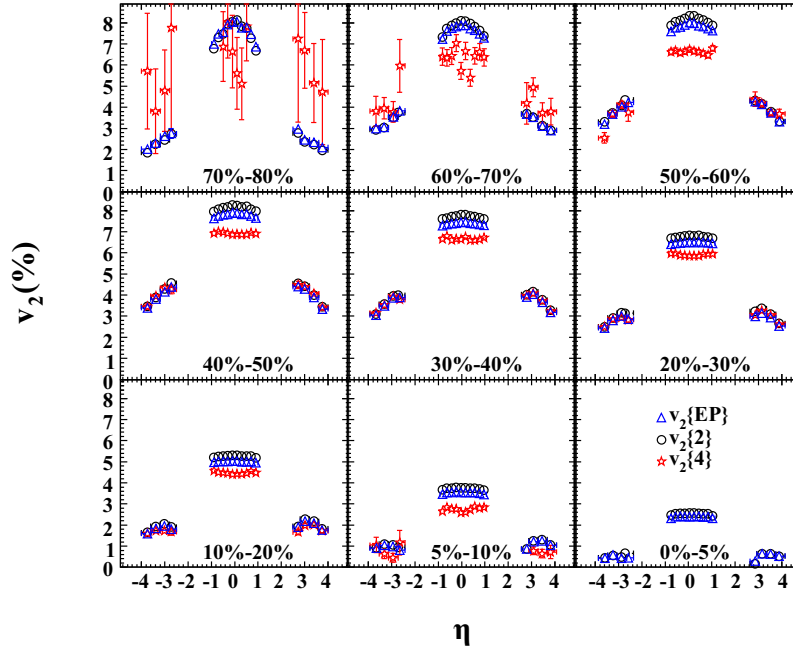


Figure 4.27: Charged particle v_2 versus η from the standard event plane method (triangles), from the two-particle cumulant method (circles) and from the four-particle cumulant method (stars) for different centrality intervals in Au+Au collisions at 200 GeV.

Figure 4.27 shows v_2 as function of η for charged particles in different centrality intervals for Au+Au collisions at 200 GeV. As before, to study the systematics, v_2 is obtained with the event plane method and the two- and the four-particle cumulants.

The second harmonic event plane is determined in the mid-rapidity region. Therefore the non-flow contributions to the v_2 values in forward-rapidity region will be significantly reduced as can be clearly seen in Fig. 4.27. Within the statistical errors in FTFC region, the values from the different methods are about the same for each centrality except the most peripheral (70–80%) where the four-particle cumulant method is limited by the multiplicity. It is seen that $v_2\{4\}$ around mid-rapidity is almost consistent with a flat distribution for all centrality bins within statistical errors. However, $v_2\{EP\}$ and $v_2\{2\}$ tend to peak at $\eta = 0$ when moving from central to peripheral collisions. The differences between $v_2\{EP\}$ or $v_2\{2\}$ and $v_2\{4\}$ at mid-rapidity are attributed either to the non-flow effects or to the fluctuations. The v_2 falls off rapidly with increasing rapidity for all centralities. The overall shape of $v_2(\eta)$ from the four-particle cumulant method is not strongly centrality dependent though the magnitude of $v_2(\eta)$ is. v_2 at forward-rapidity increases from the most central to mid-central collisions, reaches the maximum around centrality 40–50% and then decreases towards peripheral collisions.

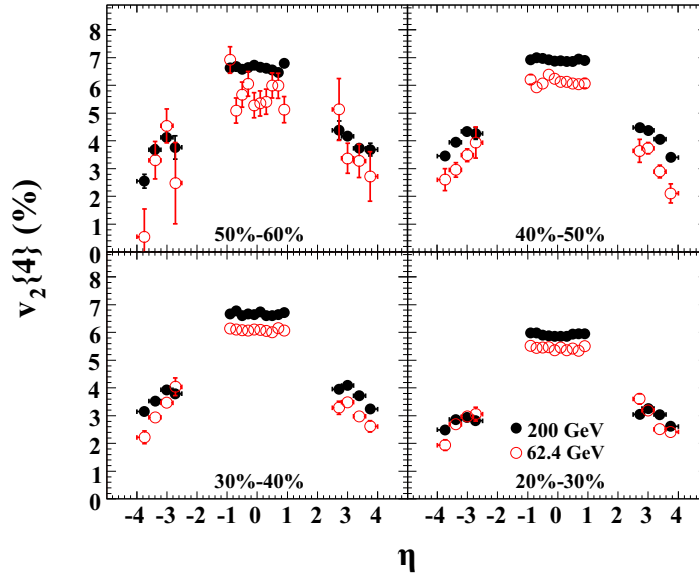


Figure 4.28: Charged particle $v_2\{4\}$ versus η for different centrality bins at 200 and 62.4 GeV in Au+Au collisions.

Figure 4.28 shows $v_2(\eta)$ obtained with the four-particle cumulant method for different centrality bins at 200 and 62.4 GeV. The ratio of $v_2(\eta)$ at these two energies is plotted in Fig. 4.29. The ratio is larger in the forward rapidity region than that at mid-rapidity.

To test the longitudinal scaling assumption, Fig. 4.30 shows v_2 as a function of $\eta - y_{beam}$ for different centralities at 200 and 62.4 GeV. The v_2 values measured at both energies fall on a universal curve, indicating that, similar to particle production, the longitudinal scaling indeed approximately holds.

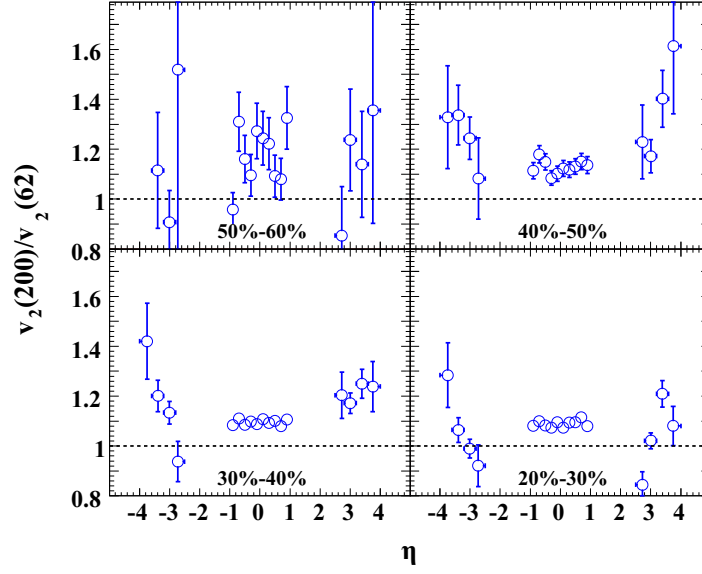


Figure 4.29: The ratio of $v_2(\eta)$ for charged particles at 200 GeV to that at 62.4 GeV for 4 different centrality classes in Au+Au collisions. v_2 is obtained with the four-particle cumulant method.

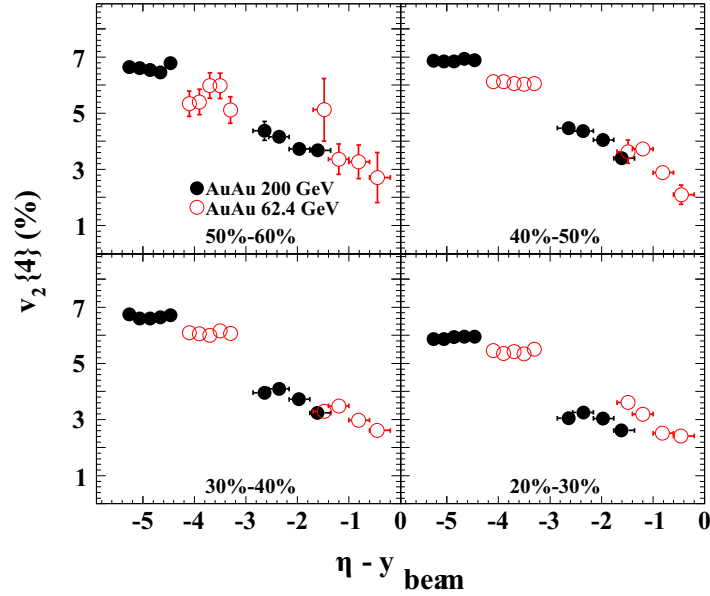


Figure 4.30: Charged particle $v_2\{4\}$ versus $\eta - y_{beam}$ for different centrality bins at 200 (full circles) and 62.4 GeV (open circles) in Au+Au collisions. The flow coefficients are shown for particles in the forward hemisphere only.

4.3 Higher harmonics

Higher harmonics of the momentum anisotropy are expected to be small [87, 88]. It was pointed out however that at higher transverse momenta these higher coefficients may become significant. Moreover the higher harmonics could be more sensitive to the initial conditions of the system than the elliptic flow coefficient v_2 [89]. In addition it was shown that they depend on the equation of state [90]. In recent work [91, 92], v_4/v_2^2 is proposed as a detailed probe of ideal hydrodynamic behavior. In ideal hydrodynamics, the ratio approaches to 0.5. Deviations from ideal-fluid behavior yield higher values due to the increased value of v_4 and this ratio is directly related to the degree of thermalization of the medium [91, 92].

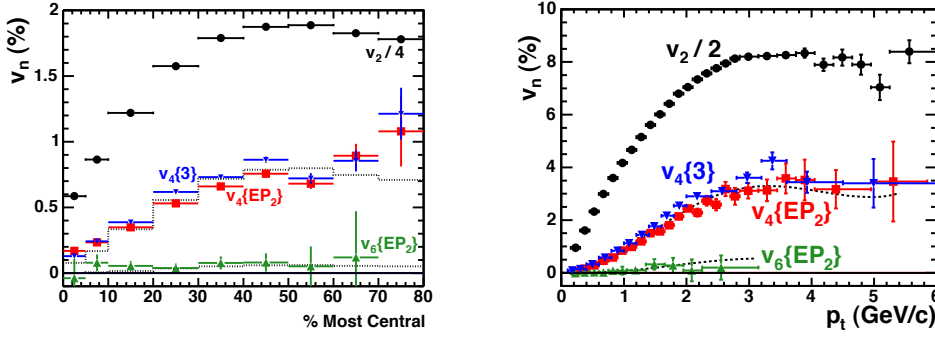


Figure 4.31: (a) The p_t - and η -integrated values of v_2 , v_4 , and v_6 with respect to the second harmonic event plane as a function of centrality [93]. The v_2 values are divided by a factor of four to fit on the scale. The three particle cumulant values for v_4 ($v_4\{3\}$) is also shown. The dotted histograms are $1.4 \cdot v_2^2$ and $1.4 \cdot v_2^3$. (b) The minimum bias values of v_2 , v_4 and v_6 with respect to the second harmonic event plane as a function of p_t [93]. The v_2 values are divided by a factor of two to fit on the scale. Also shown are the three particle cumulant values for v_4 ($v_4\{3\}$). The dashed curves are $1.2 \cdot v_2^2$ and $1.4 \cdot v_2^3$ respectively.

It has been found by STAR in Au+Au collisions at $\sqrt{s_{NN}} = 200$ GeV that the integrated v_4 is indeed an order of magnitude smaller than v_2 as expected (see Fig. 4.31 (a)). This figure also shows that the higher harmonic v_6 is consistent with zero. For the differential flow, shown in Fig. 4.31 (b), v_4 indeed becomes significant at higher p_t as expected. It was also found that these higher harmonics scale as $v_2^{n/2}$. The observed ratio of v_4/v_2^2 is larger than unity which is in disagreement with the value 0.5 expected from ideal fluid behavior.

4.3.1 Transverse momentum dependence

With the large data set in Au+Au collisions at $\sqrt{s_{NN}} = 200$ GeV, the fourth harmonic coefficient can be measured more differentially and up to higher transverse momenta.

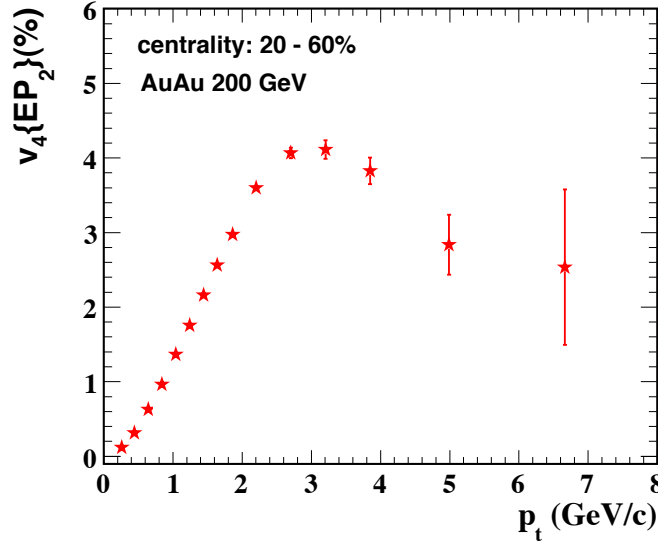


Figure 4.32: Charged particle v_4 versus p_t for 20–60% centrality interval in Au+Au collisions at 200 GeV.

The p_t dependence of the charged particle v_4 is shown for the 20–60% centrality interval in Fig. 4.32. The v_4 coefficient is obtained with respect to the second harmonic event plane and is denoted by $v_4\{EP_2\}$. It is seen that v_4 increases quadratically at low p_t and has, like v_2 , its maximum around 3 GeV/c. It is measured up to 7 GeV/c and is still sizable above 6 GeV/c.

Figure 4.33 shows the charged particle $v_4(p_t)$ for individual centralities in 200 GeV Au+Au collisions. v_4 at a given p_t increases from central to peripheral collisions. For central to mid-central collisions, the $v_4\{EP_2\}$ increases with p_t and peaks at intermediate p_t region. However, in peripheral collisions, such as 60–70% and 70–80%, v_4 continues to increase with p_t . The origin for this behavior of v_4 at high p_t in peripheral collisions could be non-flow contributions from jet like correlations. All these centralities combined, as was shown in Fig. 4.31, leads to a saturation of v_4 at intermediate p_t .

As discussed previously, the non-flow correlations affect the estimation of v_2 . The $v_2\{4\}$ is less sensitive to the non-flow effects. Figure 4.34 shows the ratio of v_4/v_2^2 as function of p_t for charged particles for the centrality range 20–60% in Au+Au collisions at 200 GeV, with v_2 obtained with the event plane method and the four-particle cumulant method respectively. It shows that both the magnitude and the trend of the ratios as function of p_t are quite different for $v_4\{EP_2\}/v_2^2\{EP\}$ and $v_4\{EP_2\}/v_2^2\{4\}$. The $v_4\{EP_2\}/v_2^2\{EP\}$ first decreases and then becomes almost constant as function of p_t . The $v_4\{EP_2\}/v_2^2\{4\}$, however, decreases with p_t , reaches its minimum at $p_t \sim 1$ GeV/c, and then starts to increase again. This might indicate that as a function of transverse momentum particle production is dominated by different mechanisms. Indeed, elliptic flow measurements have already shown that at intermediate p_t particle production can

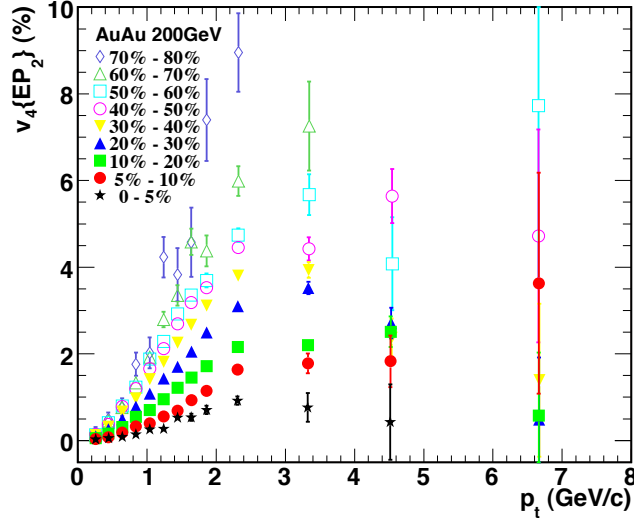


Figure 4.33: Charged particle v_4 versus p_t for 9 centrality classes in Au+Au collisions at 200 GeV.

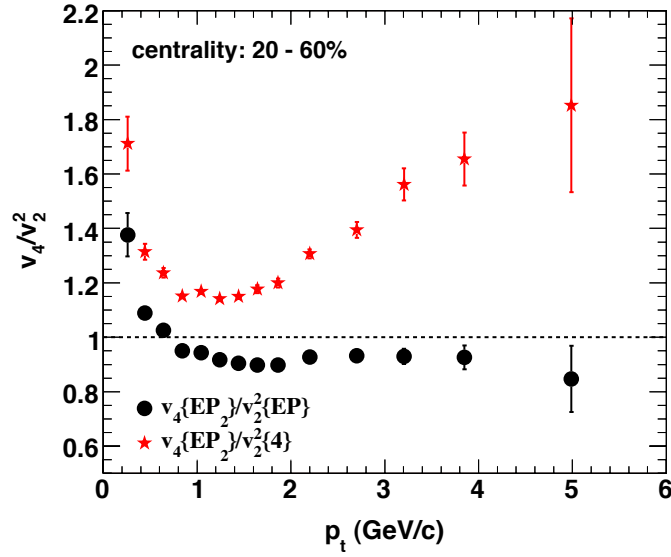


Figure 4.34: The ratio of v_4/v_2^2 versus p_t for charged particles for 20–60% centrality interval in Au+Au collisions at 200 GeV. v_2 is obtained with the standard event plane method (circles) or the four-particle cumulant method (stars).

be described by coalescence. Even though the minimum of $v_4\{EP_2\}/v_2^2\{4\}$ is much larger than the value (0.5) expected in a fully equilibrated system, its position might give information on up to which transverse momentum the hydrodynamics holds.

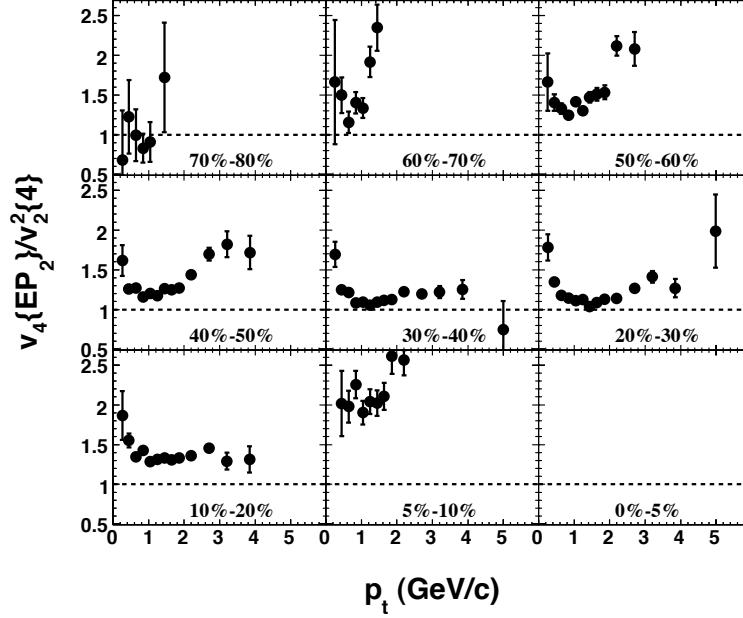


Figure 4.35: The ratio of $v_4\{EP_2\}/v_2^2\{4\}$ versus p_t for charged particles for different centrality classes in Au+Au collisions at 200 GeV.

In more central collisions a more thermalized system could be expected. The ratio v_4/v_2^2 is therefore expected to be smaller in more central collisions. Figure 4.35 shows the ratio of $v_4\{EP_2\}/v_2^2\{4\}$ as function of p_t for charged particles in different centrality classes. The centrality dependence observed does not show the expected trend, however the relatively larger non-flow effects in $v_4\{EP_2\}$ and the flow fluctuations in $v_2\{4\}$ in the most central and the peripheral collisions should be considered. Therefore, we will only focus on the mid-central collisions. It is seen that in this centrality range, the turn-over of the ratio occurs around 1 GeV/c in p_t . The ratio reaches a minimum in the 20–40% centrality interval.

As a reference, the ratio $v_4\{EP_2\}/v_2^2\{EP\}$ as function of p_t for charged particles in different centrality classes is shown in Fig. 4.36. In mid-central collisions, the ratios appear to be independent of p_t above 1 GeV/c.

Figure 4.37 shows the ratio v_4/v_2^2 measured at 200 GeV in the 20–30% centrality interval. Under the assumption that $v_2\{4\}$ is a genuine measure of elliptic flow, the systematic error in the ratio v_4/v_2^2 is dominated by non-flow contributions to v_4 . The

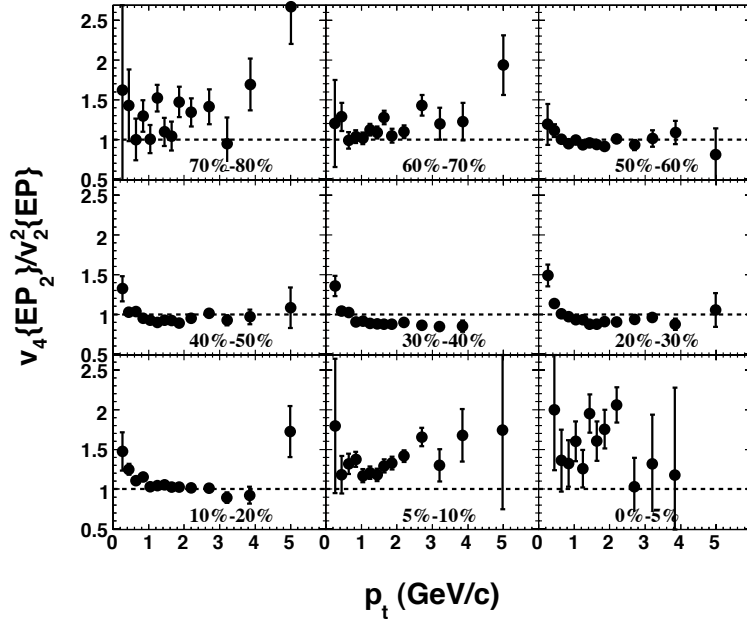


Figure 4.36: The ratio of $v_4\{EP_2\}/v_2^2\{EP\}$ versus p_t for charged particles for different centrality classes in Au+Au collisions at 200 GeV.

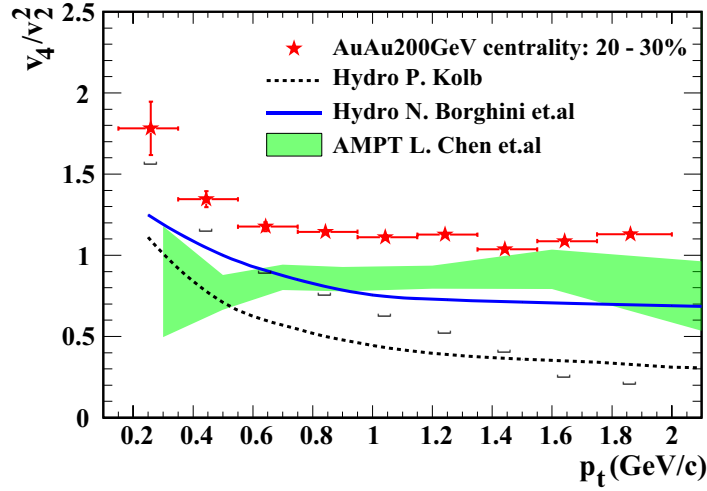


Figure 4.37: The ratio of v_4/v_2^2 versus p_t for charged particles at $|\eta| < 1.3$ in Au+Au collisions at 200 GeV. The brackets indicate the systematic uncertainty. The curves correspond to two hydrodynamic calculations [89,92]. The filled area shows the AMPT model calculations [94].

v_4 of particle i at a certain p_t can be obtained by three-particle (i, j, k) correlations:

$$\langle \cos(4\phi_i - 2\phi_j - 2\phi_k) \rangle = v_4(p_t)v_2^2, \quad (4.2)$$

where the average is taken over all the particles and events. The dominant non-flow contribution to the three particle correlation can be estimated as follows: if particle i is correlated with particle j by non-flow and correlated with particle k by flow, the three-particle non-flow correlations can be written like:

$$g_2 \times \langle \cos(2\phi_i - 2\phi_k) \rangle = g_2 \times v_2\{4\}(p_t)v_2 \quad (4.3)$$

where g_2 is the non-flow contribution from two-particle correlations. It is shown that $g_2 \propto v_2^2\{2\}(p_t) - v_2^2\{4\}(p_t)$ [49,95]. Therefore, the non-flow contributions to $v_4(p_t)$ is obtained by:

$$\frac{g_2 \times v_2\{4\}(p_t)v_2}{v_2^2} = \frac{(v_2^2\{2\}(p_t) - v_2^2\{4\}(p_t)) \times v_2\{4\}(p_t)}{v_2}. \quad (4.4)$$

The non-flow contributions to v_4/v_2^2 is then estimated by

$$\frac{v_2^2\{2\}(p_t) - v_2^2\{4\}(p_t)}{v_2v_2\{4\}(p_t)}. \quad (4.5)$$

The brackets in this figure show the lower limit of the ratio due to these systematic uncertainties. However, if the complete difference in $v_2^2\{2\} - v_2^2\{4\}$ originates from flow fluctuations, the systematic error will be reduced.

In the figure, the data are compared to two hydrodynamic model calculations [89,92] (curves) and to model predictions based on a microscopic description of the collision (AMPT model, filled area) [94]. It is seen that the data lie above the model predictions. However, the present systematic uncertainties do not allow us to completely exclude these models.

4.3.2 Particle type dependence

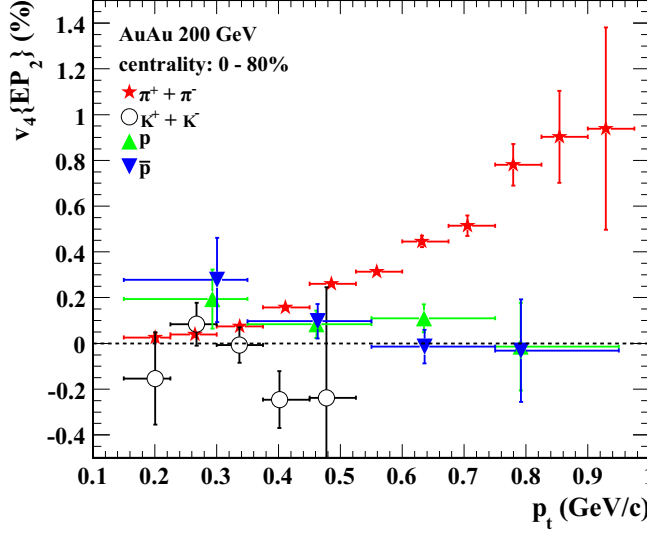


Figure 4.38: v_4 versus p_t for charged pions, kaons, protons and antiprotons in minbias Au+Au collisions at 200 GeV.

Figure 4.38 shows the v_4 in the low p_t region for charged pions, kaons, protons and antiprotons in minbias Au+Au collisions at 200 GeV. The v_4 for pions is larger than for kaons and (anti)proton and increases with p_t . The kaon and (anti)proton v_4 are essentially zero within this p_t range.

It is suggested in [96] that higher harmonics can also test quark-number scaling when measured for the identified particles. From a simple parton coalescence model, the ratio v_4/v_2^2 for meson (M) or baryon (B) is related to v_4/v_2^2 for quarks (q):

$$[v_4/v_2^2]_{p_t}^M \approx 1/4 + (1/2)[v_4/v_2^2]_{p_t/2}^q, \quad (4.6)$$

and

$$[v_4/v_2^2]_{p_t}^B \approx 1/3 + (1/3)[v_4/v_2^2]_{p_t/3}^q. \quad (4.7)$$

Figure 4.39 shows $v_4(p_t)$ at intermediate p_t for pions and (anti)protons in the 20–60% centrality interval in 200 GeV Au+Au collisions. Charged particle v_4 is displayed for comparison. At intermediate p_t , (anti)proton v_4 becomes larger than pion v_4 . This p_t dependence of v_4 is the same as the p_t dependence observed for v_2 .

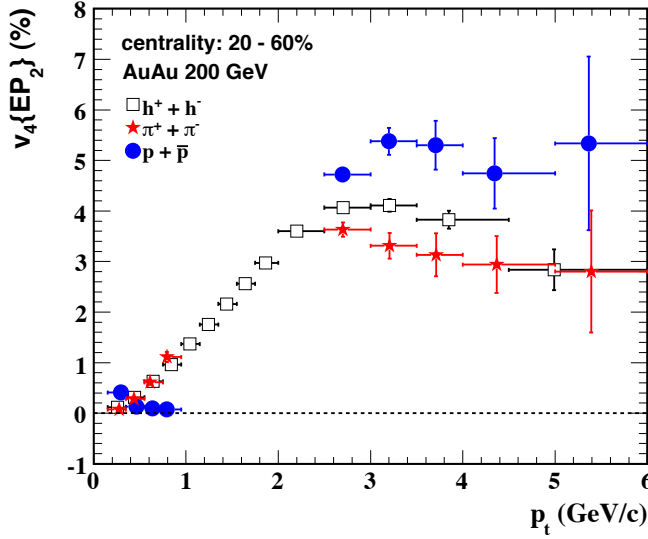


Figure 4.39: v_4 versus p_t for pions and (anti)protons for the 20–60% centrality interval in Au+Au collisions at 200 GeV. v_4 values for charged particle are displayed for comparison.

4.3.3 Energy dependence

Figure 4.40 shows the $v_4(p_t)$ for different centralities in Au+Au collisions at 62.4 GeV. As observed for 200 GeV data, v_4 at the lower RHIC energy increases with p_t and saturates at intermediate p_t for central to mid-central collisions.

Figure 4.41 shows the $v_4\{EP_2\}$ for charged particles as function of p_t for the 20–60% centrality interval in Au+Au collisions at 200 and 62.4 GeV. Compared to 200 GeV, $v_4(p_t)$ is very similar at 62.4 GeV, this behavior was also already observed for the differential elliptic flow $v_2(p_t)$.

Figure 4.42 shows the ratio of v_4/v_2^2 as function of p_t for charged particles for 20–60% centrality interval in Au+Au collisions at 200 and 62.4 GeV. The ratios of v_4/v_2^2 at 62.4 GeV are in agreement with those at 200 GeV.

4.3.4 Rapidity dependence

Due to the large data sample obtained in Au+Au Run IV, the pseudorapidity dependence of charged particle v_4 can be studied as function of centrality. In addition the pseudorapidity dependence of v_4 at 200 GeV will be compared to that at 62.4 GeV.

Figure 4.43 shows charged particle v_4 versus η for minbias Au+Au collisions at 200 and 62.4 GeV. The $v_4\{EP_2\}$ is calculated with respect to the second harmonic event plane which is determined by the particles at the mid-rapidity region. The large rapidity gap reduces the non-flow effects on the v_4 measurements at the forward rapidity region, as was already discussed for v_2 . $v_4(\eta)$ is integrated over the particles with transverse

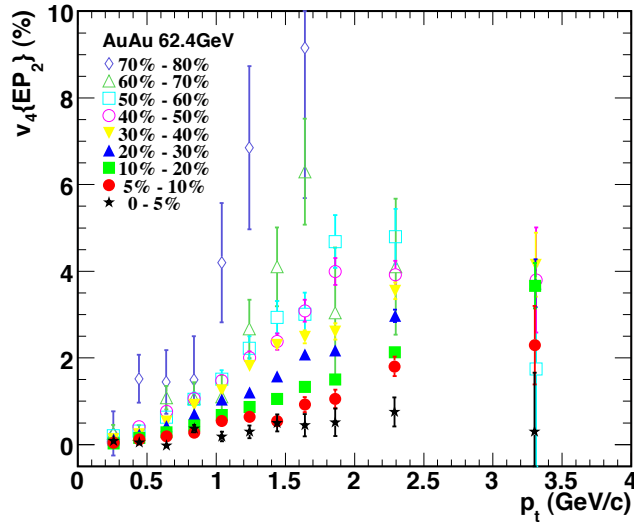


Figure 4.40: Charged particle v_4 versus p_t for 9 centrality classes in Au+Au collisions at 62.4 GeV.

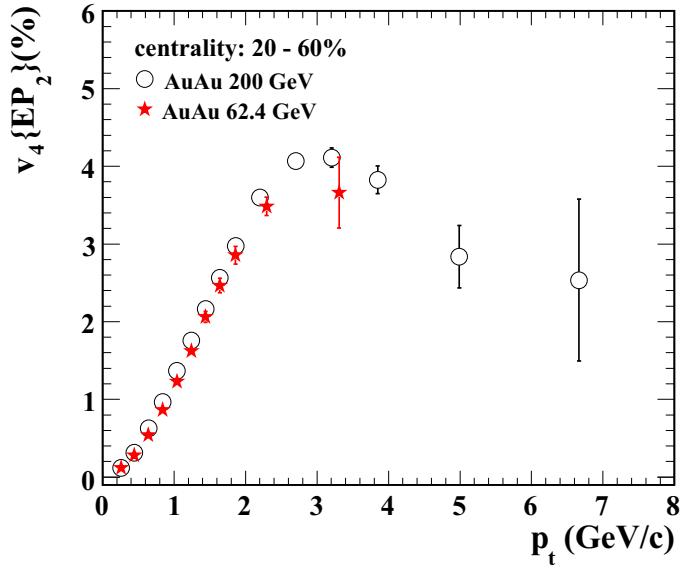


Figure 4.41: Charged particle v_4 versus p_t for 20–60% centrality in Au+Au collisions at 200 (circles) and 62.4 GeV (stars).

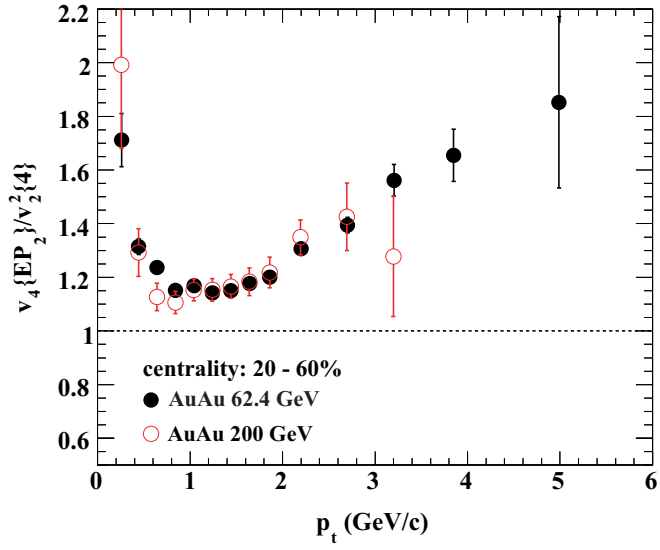


Figure 4.42: The ratio of v_4/v_2^2 versus p_t for charged particles for 20-60% centrality interval in Au+Au collisions at 200 and 62.4 GeV. v_2 is obtained with the four-particle cumulant method.

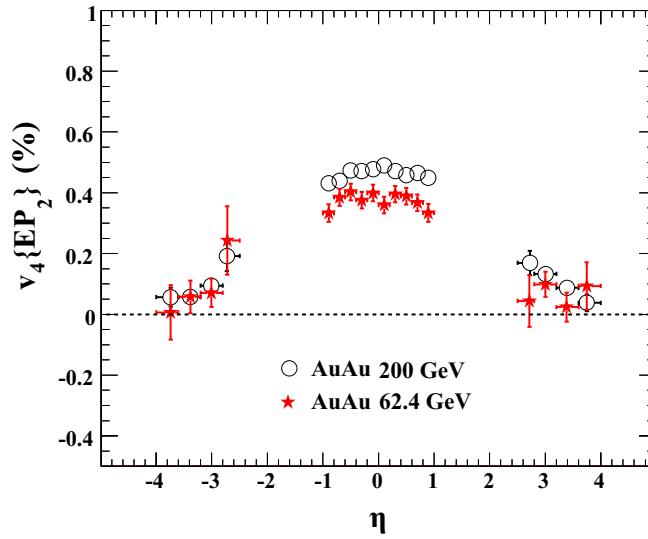


Figure 4.43: Charged particle v_4 versus η for minbias Au+Au collisions at 200 (circles) and 62.4 GeV (stars).

momentum larger than 0.15 GeV/c. At both energies, v_4 decreases quickly from mid-rapidity to forward rapidity. At mid-rapidity, v_4 at 200 GeV is larger than at 62.4 GeV. At forward rapidities, v_4 values become very small.

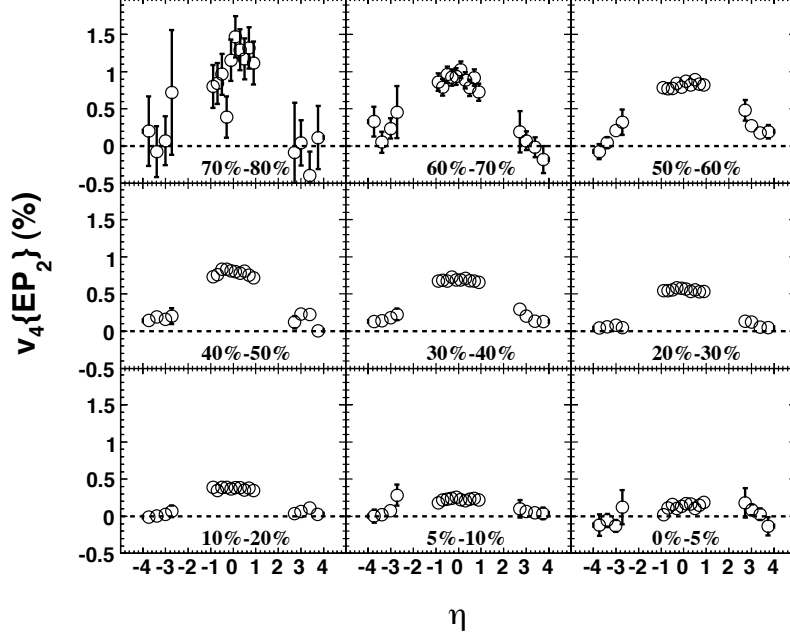


Figure 4.44: Charged particle v_4 versus η for different centralities in Au+Au collisions at 200 GeV.

The pseudorapidity dependence of v_4 is measured for different centralities, shown in Fig. 4.44 for 200 GeV data. The v_4 at mid-rapidity increases from central to peripheral collisions.

Figure 4.45 compares in detail the $v_4(\eta)$ for 4 different centrality classes in mid-central collisions at 200 GeV to 62.4 GeV. At mid-rapidity v_4 values are smaller at 62.4 GeV compared to 200 GeV, though the difference is almost indistinguishable at forward-rapidity. When plotted as function of $\eta - y_{beam}$, shown in Fig. 4.46, the v_4 values at both energies fall on a universal curve. This shows that, like for v_2 , the longitudinal scaling is also observed for v_4 .

Since hydrodynamics describes the RHIC data at mid-rapidity and breaks down at forward rapidity, v_4/v_2^2 is expected to have a minimum at mid-rapidity. Figure 4.47 shows the pseudorapidity dependence of $v_4\{EP_2\}/v_2^2\{4\}$ as well as $v_4\{EP_2\}/v_2^2\{EP\}$ for charged particles in the 20–60% centrality interval for 200 GeV Au+Au collisions. Contrary to expectation, $v_4\{EP_2\}/v_2^2\{4\}$ has a maximum at mid-rapidity and decreases

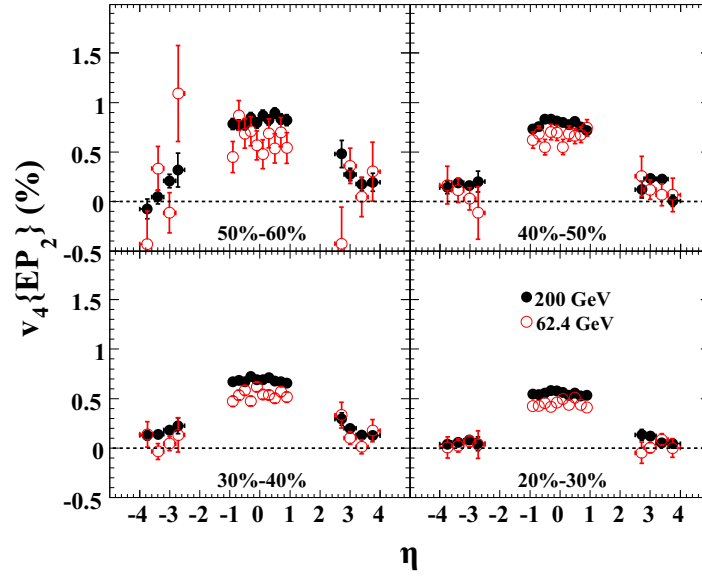


Figure 4.45: Charged particle v_4 versus η for 4 different centrality intervals in Au+Au collisions at 200 (full circles) and 62.4 GeV (open circles).

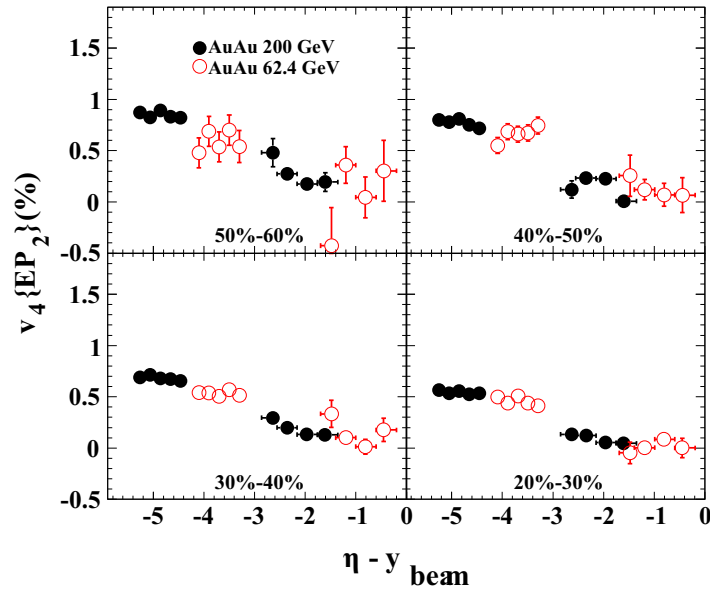


Figure 4.46: Charged particle v_4 versus $\eta - y_{beam}$ for different centrality bins at 200 (full circles) and 62.4 GeV (open circles). The flow coefficients are shown for particles in the forward hemisphere only.

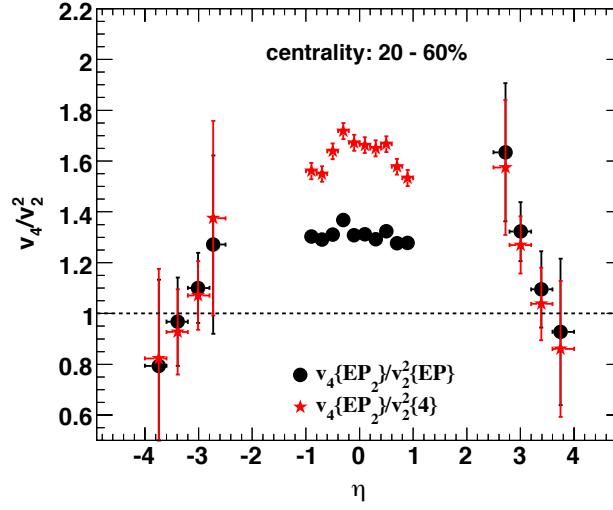


Figure 4.47: The ratio of v_4/v_2^2 versus η for charged particles for 20–60% centrality interval in Au+Au collisions at 200 GeV. v_2 is obtained with the standard event plane method (circles) and four-particle cumulant method (stars).

at larger rapidity. This is also observed for the individual centralities, presented in Fig. 4.48.

Figure 4.49 shows the energy dependence of the ratio $v_4\{EP_2\}/v_2^2\{4\}$ as function of η for charged particles for 20–60% centrality. The ratios measured are, within the statistical uncertainties, at both 200 and 62.4 GeV comparable.

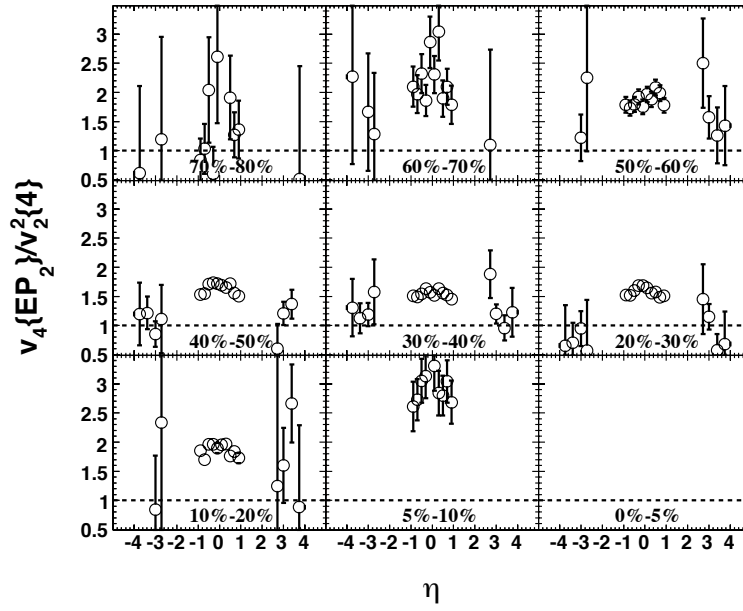


Figure 4.48: The ratio of $v_4\{EP_2\}/v_2^2\{4\}$ versus η for charged particles for different centrality classes in Au+Au collisions at 200 GeV.

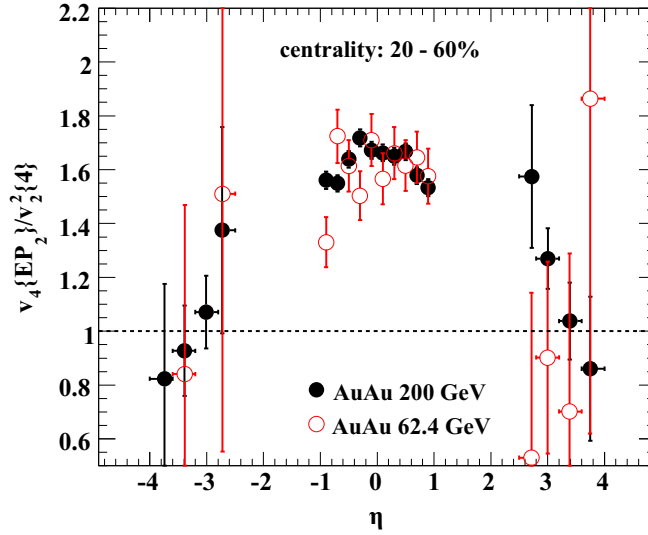


Figure 4.49: The ratio of $v_4\{EP_2\}/v_2^2\{4\}$ versus η for charged particles for 20–60% centrality interval in Au+Au collisions at 200 and 62.4 GeV.

Chapter 5

Conclusions and Summary

In this thesis an anisotropic flow analysis is described which is done to understand the properties of hot and dense matter created in heavy-ion collisions at the Relativistic Heavy Ion Collider (RHIC). The data used for the analysis are Au+Au collisions at both $\sqrt{s_{NN}} = 200$ GeV and $\sqrt{s_{NN}} = 62.4$ GeV measured with the Solenoidal Tracker experiment at RHIC (STAR). The two largest anisotropic flow coefficients, elliptic flow v_2 and the fourth harmonic v_4 , are measured for inclusive charged particles as well as charged pions, kaons and (anti)protons. The flow coefficients are studied as function of transverse momentum, centrality and pseudorapidity. The main systematic errors come from so-called non-flow contributions and from the unknown fluctuations in the observable. Therefore different methods, the event plane and the two- and the four-particle cumulants, are applied to estimate the anisotropic flow coefficients and based on the difference between the methods estimate the systematic uncertainty.

Elliptic flow

In this thesis we show, with the large data sample obtained in Au+Au collisions at $\sqrt{s_{NN}} = 200$ GeV, elliptic flow for charged particles up to 8 GeV/ c for different collision centralities obtained using the four-particle cumulant method. The sizable elliptic flow observed with this method at high p_t is consistent with the scenario of parton energy loss and is evidence for the formation of very dense matter.

With the particle identification extended to higher transverse momentum ($p_t > 2.5$ GeV/ c) using the relativistic rise of the specific ionization energy loss in the Time Projection Chamber (TPC), we measure the elliptic flow of pions and protons at intermediate to high p_t . The characteristic low p_t mass ordering and its break down at intermediate p_t , first observed for K_s^0 and Λ , is with this analysis also seen for the pions and protons. These observations combined confirm the baryon meson scaling and are in agreement with the quark number scaling. This observation is often quoted as evidence for the observation of parton degrees of freedom at RHIC.

The very similar transverse momentum dependence of $v_2\{4\}$ for inclusive charged particles as well as identified particles at 62.4 and 200 GeV has been interpreted as an indication of the softening of the Equation of State at RHIC energies. However, from

the 200 and 62.4 GeV data, it follows that at mid-rapidity the integrated v_2 increases approximately linearly from AGS to the top RHIC energy. At the full RHIC energy for near central collision, the value of v_2 do approach, for the first time in heavy-ion collisions, the ideal hydrodynamic calculations. The disagreement between the data and the hydrodynamic calculations at lower energies is interpreted as a sign of incomplete thermalization.

In addition the analysis in this thesis shows that the charged particle $v_2(\eta)$ at these two energies follows the longitudinal scaling when plotted as a function of $\eta - y_{beam}$, consistent with the picture of $v_2 \propto dN/dy$.

Higher harmonics

The importance of measuring the higher harmonics to probe the properties of the created system has been pointed out by various authors [15, 50, 87–89]. Actual measurements have been challenging because of the very small magnitude of the signal. However, because of the relative large elliptic flow at RHIC we can study for the first time the fourth harmonic, v_4 , in detail. At 200 GeV, we have measured the charged particle v_4 up to 7 GeV/ c and shown that it is still sizable above 6 GeV/ c . At low p_t , it is seen that the pion v_4 is larger than that of (anti)proton. At intermediate p_t , v_4 for (anti)protons is larger than for pions, this behavior is similar to the behavior observed for identified particle v_2 . In addition, the longitudinal scaling observed for elliptic flow is also seen in $v_4(\eta)$.

In recent work [91, 92], the ratio v_4/v_2^2 is proposed as a more sensitive probe of ideal hydrodynamic behavior. Furthermore, it is argued that the ratio is directly related to the degree of thermalization. The measured ratio v_4/v_2^2 as function of p_t is found to be above the values expected for ideal fluid behavior, indicative of still incomplete thermalization at the full RHIC energies. Surprisingly, the ratio is found to be larger at mid-rapidity than at forward-rapidity. The ratio as function of centrality has a minimum for mid-central collisions.

Summary

Anisotropic flow measurements at RHIC have shown that the created system to first order can be described as a thermalized fluid which expands hydrodynamically. This has been the main experimental pillar for the perfect liquid discovery [97, 98]. The detailed measurements of anisotropic flow described in this thesis do show however that there are still signs of incomplete thermalization. Uncertainties in modelling the initial conditions and in the Equation of State make a more unambiguous statement at RHIC energies difficult. It is expected that anisotropic flow measurements at the CERN Large Hadron Collider (LHC) will reduce these uncertainties significantly.

Bibliography

- [1] F. Karsch and E. Laermann, “Quark-Gluon Plasma 3”, Editors: R. C. Hwa and X. N. Wang, World Scientific, Singapore (2003).
- [2] “Quark-Gluon Plasma: theoretical foundations”, J. Kapusta, B. Muller and J. Rafelski, Elsevier (2003).
- [3] M. Gyulassy and M. Plumer, Phys. Lett. B**243**, 432 (1990).
- [4] J. W. Cronin *et al.*, Phys. Rev. D**11**, 3105 (1975).
- [5] M. Arneodo, Phys. Rept. **240**, 301 (1994).
- [6] L. McLerran and R. Venugopalan, Phys. Rev. D**49**, 2233 (1994).
- [7] L. McLerran and R. Venugopalan, Phys. Rev. D**49**, 3352 (1994).
- [8] L. McLerran and R. Venugopalan, Phys. Rev. D**50**, 2225 (1994).
- [9] J. Adams *et al.* Phys. Rev. Lett. **91**, 072304 (2003).
- [10] I. G. Bearden *et al.*, Phys. Rev. Lett. **78**, 2080 (1997).
- [11] E. Schnedermann, J. Sollfrank, and U. Heinz, Phys. Rev. C**48**, 2462 (1993).
- [12] J. Adams *et al.*, Phys. Rev. Lett. **92**, 112301 (2004).
- [13] H. Sorge, Phys. Rev. Lett. **82**, 2048 (1999).
- [14] S. A. Voloshin and A. M. Poskanzer, Phys. Lett. B**474**, 27 (2000).
- [15] P. Kolb, J. Sollfrank, and U. Heinz, Phys. Rev. C**62**, 054909 (2000).
- [16] S. Voloshin and Y. Zhang, Z. Phys. C**70**, 665 (1996).
- [17] B. Alver *et al.*, Phys. Rev. Lett. **98**, 242302 (2007).
- [18] P. Kolb and U. Heinz, “Quark-Gluon Plasma 3”, Editors: R. C. Hwa and X. N. Wang, World Scientific, Singapore (2003).
- [19] H. Sorge, Phys. Rev. Lett. **78**, 2309 (1997).

- [20] H. Sorge, Phys. Lett. B**402**, 251 (1997).
- [21] H. Bebie, P. Gerber, J. L. Goity, and H. Leutwyler, Nucl. Phys. B**378**, 95 (1992).
- [22] S. A. Bass *et al.*, Prog. Part. Nucl. Phys. **41**, 255 (1998).
- [23] M. Bleicher *et al.*, J. Phys. G**25**, 1859 (1999).
- [24] X. N. Wang and M. Gyulassy, Phys. Rev. D**44**, 3501 (1991).
- [25] B. Zhang, Comput. Phys. Commun. **109** 193 (1998).
- [26] T. Sjostrand, Comput. Phys. Commun. **82** 74 (1994).
- [27] B. A. Li and C. M. Ko, Phys. Rev. C**52**, 2037 (1995).
- [28] Zi-wei Lin and C. M. Ko, Phys. Rev. C**65**, 034904 (2002).
- [29] H. Hahn *et al.*, Nucl. Instrum. Meth. A**499**, 245 (2003).
- [30] M. Adamczyk *et al.*, Nucl. Instrum. Meth. A**499**, 437 (2003).
- [31] B. B. Back *et al.*, Nucl. Instrum. Meth. A**499**, 603 (2003).
- [32] K. Adcox *et al.*, Nucl. Instrum. Meth. A**499**, 469 (2003).
- [33] K. H. Ackermann *et al.*, Nucl. Instrum. Meth. A**499**, 624 (2003).
- [34] M. Anderson *et al.*, Nucl. Instrum. Meth. A**499**, 659 (2003).
- [35] K. H. Ackermann *et al.*, Nucl. Instrum. Meth. A**499**, 713 (2003).
- [36] F. S. Bieser *et al.*, Nucl. Instrum. Meth. A**499**, 766 (2003).
- [37] M. Miller, K. Reygers, S. Sanders, and P. Steinberg, *arXiv: nucl-ex/0701025* (2007).
- [38] C. Adler *et al.*, Phys. Rev. Lett. **87**, 112303 (2001).
- [39] B. B. Back *et al.*, Phys. Rev. C**65**, 031901 (2002).
- [40] K. Adcox *et al.* Phys. Rev. Lett. **86**, 3500 (2001).
- [41] I. G. Bearden *et al.*, Phys. Lett. B**523**, 227 (2001).
- [42] A. Tang, Ph.D thesis, Kent State University (2002).
- [43] Z. B. Xu, Int. J. Mod. Phys. A**20**, 3783 (2005).
- [44] B. I. Abelev *et al.*, Phys. Rev. Lett. **97**, 152301 (2006).
- [45] A. Poskanzer and S. Voloshin, Phys. Rev. C **58**, 1671 (1998).
- [46] C. Alt *et al.*, Phys. Rev. C**68**, 034903 (2003).

- [47] J. Y. Ollitrault, Phys. Rev. D**46**, 229 (1992).
- [48] J. Y. Ollitrault, Phys. Rev. D**48**, 1132 (1993).
- [49] C. Adler *et al.*, Phys. Rev. C**66**, 034904 (2002).
- [50] N. Borghini, P. M. Dinh (2), J. Y. Ollitrault Phys. Rev. C**64**, 054901 (2001).
- [51] N. Borghini, P. M. Dinh, and J. Y. Ollitrault, *arXiv: nucl-ex/0110016* (2001).
- [52] R. S. Bhalerao, N. Borghini, and J. Y. Ollitrault, Phys. Lett. B**580**, 157 (2004).
- [53] R. S. Bhalerao, N. Borghini, and J. Y. Ollitrault, Nucl. Phys. A**727**, 373 (2003).
- [54] N. Borghini, R. S. Bhalerao, and J. Y. Ollitrault, J. Phys. G**30**, S1213 (2004).
- [55] C. N. Yang and T. D. Lee, Phys. Rev. **87**, 404 (1952).
- [56] C. Adler *et al.*, Phys. Rev. Lett. **87**, 182301 (2001).
- [57] B. I. Abelev *et al.*, Phys. Rev. C**75**, 054906 (2007).
- [58] C. Adler *et al.*, Phys. Rev. Lett. **90**, 032301 (2003).
- [59] P. Huovinen, P. F. Kolb, Ulrich W. Heinz, P. V. Ruuskanen, and S. A. Voloshin, Phys. Lett. B**503**, 58 (2001).
- [60] M. Gyulassy, I. Vitev, and X. N. Wang, Phys. Rev. Lett. **86**, 2537 (2001).
- [61] D. Teaney, Phys. Rev. C**68**, 034913 (2003).
- [62] X. N. Wang and M. Gyulassy, Phys. Rev. Lett. **68**, 1480 (1992).
- [63] R. J. M. Snellings, A. M. Poskanzer, and S. A. Voloshin. *arXiv: nucl-ex/9904003* (1999).
- [64] X. N. Wang, Phys. Rev. C**63**, 054902 (2001).
- [65] M. Gyulassy, I. Vitev, X. N. Wang, and P. Huovinen, Phys. Lett. B**526**, 301 (2002).
- [66] M. Miller and R. Snellings, *arXiv: nucl-ex/0312008* (2003).
- [67] H. Heiselberg and A. M. Levy, Phys. Rev. C**59**, 2716 (1999).
- [68] J. Adams *et al.*, Phys. Rev. C**72**, 014904 (2005).
- [69] J. Adams *et al.*, Phys. Rev. Lett. **95**, 122301 (2005).
- [70] S. A. Voloshin, Nucl. Phys. A**715**, 379 (2003).
- [71] D. Molnar and S. A. Voloshin, Phys. Rev. Lett. **91** 092301 (2003).
- [72] R. C. Hwa and C. B. Yang, Phys. Rev. C**67**, 064902 (2003).

- [73] V. Greco, C. M. Ko, and P. Levai, Phys. Rev. Lett. **90**, 202302 (2003).
- [74] R. J. Fries, B. Muller, C. Nonaka, and S. A. Bass, Phys. Rev. Lett. **90**, 202303 (2003).
- [75] S. Manly *et al.*, Nucl. Phys. A**715**, 611 (2003).
- [76] P. Chung *et al.*, Phys. Rev. C**66**, 021901 (2002).
- [77] R. L. Ray, Nucl. Phys. A**715**, 45 (2003).
- [78] S. Esumi, Nucl. Phys. A**715**, 599 (2003).
- [79] B. Zhang, M. Gyulassy, and C. M. Ko, Phys. Lett. B**455**, 45 (1999).
- [80] D. Molnar and M. Gyulassy, Nucl. Phys. A**697**, 495 (2002).
- [81] T. Hirano, U. Heinz, D. Kharzeev, R. Lacey, and Y. Nara, J. Phys. G**34**, S879 (2007).
- [82] D. Teaney, J. Lauret, and E. V. Shuryak, Phys. Rev. Lett. **86**, 4783 (2001).
- [83] S. S. Adler *et al.*, Phys. Rev. Lett. **94**, 232302 (2005).
- [84] B. B. Back *et al.*, Phys. Rev. Lett. **89**, 222301 (2002).
- [85] B. B. Back *et al.*, Phys. Rev. C**74**, 021901 (2006).
- [86] N. Borghini, Eur. Phys. J. A**29**, 27 (2006).
- [87] P. F. Kolb, J. Sollfrank, and U. W. Heinz, Phys. Lett. B**459**, 667 (1999).
- [88] D. Teaney and E. V. Shuryak, Phys. Rev. Lett. **83**, 4951 (1999).
- [89] P. F. Kolb, Phys. Rev. C**68**, 031902 (2003).
- [90] P. Huovinen, Nucl. Phys. A**761**, 296 (2005).
- [91] R. S. Bhalerao, J. P. Blaizot, N. Borghini and J. Y. Ollitrault, Phys. Lett. B**627**, 49 (2005).
- [92] N. Borghini and J. Y. Ollitrault, Phys. Lett. B**642**, 227 (2006).
- [93] J. Adams *et al.*, Phys. Rev. Lett. **92**, 062301 (2004).
- [94] L. W. Chen, C. M. Ko, and Z. W. Lin, Phys. Rev. C**69**, 031901 (2004).
- [95] N. Borghini, P. M. Dinh, and J. Y. Ollitrault, Phys. Rev. C**66**, 014905 (2002).
- [96] P. F. Kolb, L. W. Chen, V. Greco, and C. M. Ko, Phys. Rev. C**69**, 051901 (2004).
- [97] J. Adams *et al.*, Nucl. Phys. A**757**, 102 (2005).
- [98] “New discoveries at RHIC”, Proceedings of RIKEN BNL Research Center Workshop, Volume **62**, (2004).

Samenvatting

In dit proefschrift worden de eigenschappen van Quantum Chromo Dynamica (QCD) bestudeerd bij de zeer hoge energiedichtheden die bereikt worden in botsingen van zware-ionen in de ‘Relativistic Heavy-Ion Collider’ (RHIC). De metingen van dit onderzoek zijn gedaan aan goud-goud botsingen met een energie van $\sqrt{s_{NN}} = 200$ GeV en 62.4 GeV en zijn verricht met de STAR detector (de ‘Solenoidal Tracker at RHIC’).

In een niet-centrale zware-ionenbotsing is het initiële transversale overlapgebied van de kernen niet symmetrisch. De ontstane drukgradiënt in het begin van de botsing is hierdoor verschillend in de x- en y-richting, hetgeen leidt tot een verschil in de transversale impulsverdelingen van de deeltjes in deze richtingen. Dit verschil van de deeltjesdistributies wordt anisotrope stroming genoemd en gekarakteriseerd door de coëfficiënten v_n . Deze coëfficiënten v_n worden gedefinieerd door een Fourier-reeks ontwikkeling van de transversale impulsverdelingen als functie van azimuth. De twee belangrijkste coëfficiënten, v_2 en v_4 , worden in dit proefschrift bestudeerd als functie van de botsingsenergie, de centraliteit van de botsing, de deeltjes identiteit en de transversale impuls. Deze metingen maken het mogelijk om de toestandsvergelijking van het gecreëerde systeem te toetsen aan voorspellingen uit QCD. Voor deeltjes met hoge transversale impuls kan met deze metingen de interactie van deze deeltjes met het gecreëerde systeem getoetst worden.

Voor het bepalen van de coëfficiënten v_n wordt de grootste bijdrage in de systematische onzekerheid veroorzaakt door (a) correlaties tussen de deeltjes die niet gegenereerd worden door de anisotrope stroming zelf en (b) door de verschillen in de anisotrope stroming in de individuele botsingen (die verder wel dezelfde karakteristieken hebben). In dit proefschrift is met behulp van verschillende analyse methoden deze systematische onzekerheid bepaald.

Uit de analyse blijkt dat deeltjes met een transversale impuls van 8 GeV/c een significante anisotrope stroming vertonen. Hieruit volgt dat deze deeltjes inderdaad interacties met het gecreëerde systeem ondergaan, hetgeen wordt verspeld door de theorie. Hieruit kan worden afgeleid dat het gecreëerde systeem een zeer hoge dichtheid moet hebben.

De meting van de anisotrope stroming van geladen pionen, protonen en antiprotonen met transversale impuls groter dan 2.5 GeV/c zoals beschreven in dit proefschrift, samen met de al gemeten anisotrope stroming van neutrale kaonen en Λ s, laat duidelijk zien dat de anisotrope stroming bij deze transversale impuls afhangt van het aantal ‘constituent’ quarks van het deeltje. Dit wordt door velen gezien als een sterke aanwijzing voor quarks als relevante vrijheidsgraden in het geproduceerde systeem.

De hoge gemeten waarden van de anisotrope stroming, die word gedomineerd door de deeltjes met transversale impuls onder de $1 \text{ GeV}/c$, als ook de gevonden karakteristieke deeltjes massa afhankelijkheid was voorspeld door hydrodynamische model berekeningen. Gedetailleerde studies hebben laten zien dat een dergelijke overeenkomst tussen theorie en meting alleen mogelijk is wanneer het systeem heel snel in thermisch evenwicht komt ($< 1 \text{ fm}/c$) en een zeer lage viscositeit heeft. Uit de hier gepresenteerde metingen van de anisotrope stroming, getoetst aan de voorspellingen van hydrodynamische modellen, laten zowel de botsingsenergie afhankelijkheid, de centraliteits afhankelijkheid, maar vooral ook de ratio v_4/v_2^2 zien dat het systeem niet waarschijnlijk volledig in thermisch evenwicht is. Onzekerheden in de parameters van de modellen maken het moeilijk om bij RHIC, gebaseerd op deze metingen, een meer kwantitatieve uitspraak te doen. Door het meten van de anisotrope stroming bij de toekomstige ‘Large Hadron Collider’ (LHC) te CERN wordt naar verwachting de onzekerheid in de parameters significant kleiner.

Acknowledgements

The past four and a half years of Ph.D. research at Nikhef have been a great experience. I would like to mention a few people who have contributed in particular.

I am grateful to my supervisor Raimond Snellings for guiding me in the field of heavy-ion physics step by step, for being very supportive, for his insightful suggestions on physics, for quick answers on questions about computing and english and for his infinite patience. The thesis would not be in this shape without lots of help from him.

I would like to thank Aihong Tang at BNL who has been actively involved in my analysis and has given me lots of suggestions and has answered many questions on the techniques used for flow analysis and on the physics of heavy-ion collisions..

I also appreciate the discussions and the suggestions from other Flowers in STAR: Yan Lu, Art Poskanzer, Ilya Selyuzhenkov, Paul Sorensen, Sergei Voloshin and Gang Wang.

I would like to thank Nu Xu for giving me the opportunity to visit LBNL and for the continuous encouragement.

I would like to thank Thomas Peitzmann acting as my promoter. My gratitude also goes to the other members in the ALICE group at Nikhef and at the Utrecht university for the very friendly atmosphere. Special thanks also goes to Teus van Egdom and Ed van Willigen in the personnel department at Nikhef for their help with everything.

Thanks to the reading committee: Stan Bentvelsen, Rene Kamermans, Justus Koch and Eric Laenen for quickly reading the thesis in the final days.

Finally, thanks to my family for their endless love and support.

Curriculum Vitae

General:

Name Yuting Bai
Birth December 31, 1975
Nationality Chinese

Education:

04/2003 - 10/2007 Ph.D. in the National Institute of Subatomic Physics
(Nikhef),
Amsterdam, The Netherlands
09/1998 - 03/2003 M.S. in Physics in the Institute of Particle Physics,
Central China Normal University,
WuHan, China
09/1994 - 06/1998 B.A. in Physics in the Physics Department,
Central China Normal University,
WuHan, China

Papers in preparation:

- The fourth harmonic coefficient of anisotropic flow for charged particles at $\sqrt{s_{NN}} = 200$ GeV and 62.4 GeV
- Centrality dependence of charged and strange hadron elliptic flow from 200 GeV Au+Au collisions

Publications as one of the principal authors:

- B. I. Abelev *et al.*, “Mass, quark-number, and $\sqrt{s_{NN}}$ dependence of the second and fourth flow harmonics in ultra-relativistic nucleus nucleus collisions,” Phys. Rev. C **75** (2007) 054906
- J. Adams *et al.*, “Azimuthal anisotropy in Au + Au collisions at $\sqrt{s_{NN}} = 200$ -GeV,” Phys. Rev. C **72** (2005) 014904
- Ataian, M. R. *et al.*, “ Transverse-momentum fluctuations in π^+p and K^+p collisions at 250 GeV/c,” Phys. Rev. Lett., **89** (2002) 121802

- Y. Wu, L. Liu, Y. Wang, Y. Bai and H. Liao, “Two correlation patterns as indicators for underlying dynamics of complex systems,” *Phys. Rev. E* **71** (2005) 017103

Proceedings:

- Yuting Bai (for the STAR Collaboration), “The anisotropic flow coefficients v_2 and v_4 in Au+Au collisions at RHIC,” *J. Phys. G: Nucl. Part Phys.* **34** (2007) S903

Talks:

- “ v_2 and v_4 centrality, p_t and particle-type dependence in Au+Au collisions at RHIC” presented at the CERN Heavy Ion Forum, December 13, 2006.
- “ v_2 and v_4 centrality, p_t and particle-type dependence in Au+Au collisions at RHIC” presented at Quark Matter 2006, Shanghai, China, November 18, 2006.
- “Energy dependence of anisotropic flow” presented at “Quark Confinement and the Hadron Spectrum VII”, Ponta Delgada, Portugal, September 2-7, 2006.
- “Anisotropic flow as probe of thermalization” presented at RHIC & AGS Users Meeting at BNL, June 5-7, 2006.
- “Similarities and differences in elliptic flow of identified particles at 62 and 200 GeV” presented at a workshop on “QCD Theory and RHIC Physics”, Wuhan, China, June 19-24, 2005.
- “Identified v_2 and v_4 in Au+Au collisions” presented at DNP, Chicago, USA, October, 29, 2004.
- “Transverse-momentum fluctuations in π^+p and K^+p collisions at 250 GeV/ c ” presented at “Correlation and Fluctuation in Multiparticle Production”, Crete island, Greece, June 8-15, 2002.
- “Event-by-Event fluctuations of transverse momentum in elementary collisions at 250 GeV/ c ” presented at ISMD, Datong, China, September 1-7, 2001.